Title

The Application of the Symmetry Properties of Optical Second Harmonic Generation to Studies of Interfaces and Gases

Author

Feller, M.B.

Publication Date

1991-11-01

Lawrence Berkeley Laboratory
UNIVERSITY OF CALIFORNIA

Materials & Chemical
Sciences Division

The Application of the Symmetry Properties of Optical Second Harmonic Generation to Studies of Interfaces and Gases

M.B. Feller
(Ph.D. Thesis)

November 1991

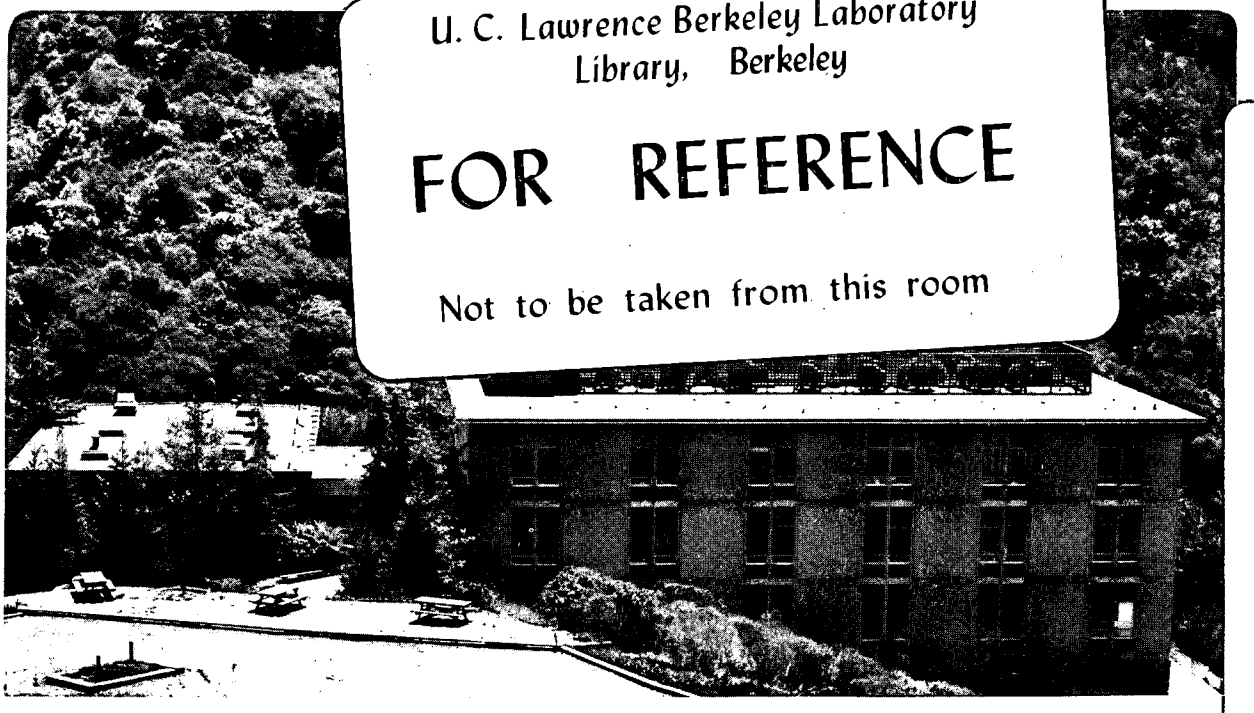

Prepared for the U.S. Department of Energy under Contract Number DE-AC03-76SF00098

DISCLAIMER

LBL-31577

THE APPLICATION OF THE SYMMETRY PROPERTIES OF OPTICAL SECOND HARMONIC GENERATION TO STUDIES OF INTERFACES AND GASES

MARLA BETH FELLER
Ph.D. Thesis

DEPARTMENT OF PHYSICS
University of California

and

MATERIALS SCIENCES DIVISION
Lawrence Berkeley Laboratory
University of California
Berkeley, CA 94720

NOVEMBER 1991

This work was supported by the Director, Office of Energy Research, Office of Basic Energy Sciences, Materials Sciences Division, of the U.S. Department of Energy under Contract No. DE-AC03-76SF00098.

The Application of the Symmetry Properties of Optical Surface Second Harmonic Generation to the Study of Interfaces and Gases

by

Marla Beth Feller

Abstract

Optical second harmonic generation has proven to be a powerful tool for studying interfaces. The symmetry properties of the process allow for surface sensitivity not available with other optical methods. In this thesis, we take advantage of these symmetry properties SHG to study a variety of interesting systems not previously studied with this technique.

We show that optical second harmonic generation is an effective surface probe with a submonolayer sensitivity for media without inversion symmetry. We demonstrate the technique at a gallium arsenide surface, exploiting the different symmetry properties of the bulk and surface of the crystal to isolate the surface contribution. The adsorption of tin onto gallium arsenide is used to demonstrate submonolayer sensitivity. A detailed summary of all accessible elements of the surface nonlinear susceptibility tensor $\chi^{(2)}$ for the various faces of GaAs is provided.

We also demonstrate that optical second harmonic generation can be used to determine the anisotropic orientational distribution of a surface monolayer of molecules. We apply the technique to study homogeneously aligned liquid crystal cells. The surface dipole sensitivity of the technique made it possible to study the monolayer in the absence and presence of a bulk of liquid crystal. By comparing the monolayer orientational distribution functions of three surface treatments (rubbed polymer-coated substrates,

rubbed surfactant-coated substrates, and substrates made from oblique evaporation of SiO_x film), we find that two different surface-originated mechanisms are effective in aligning liquid crystal films. For rubbed polymer samples, it is shown that a short-range molecular interaction is responsible for alignment of the first monolayer which then aligns the bulk via an epitaxy-like interaction. Results on polymers with various structures and compositions and rubbed with a variety of rubbing strengths are presented. For the other surface treatments, the first monolayer is isotropically distributed, indicating a bulk elastic interaction is responsible for the bulk alignment.

To further explore the LC-polymer interface, we used SHG to study the surface memory effect. The surface memory effect is the rendering of an isotropic interface anisotropic by putting it in contact with an anisotropic bulk. We found that by placing an unrubbed polymer substrate in contact with an aligned LC cell, the unrubbed polymer was changed such that it aligns a nematic phase of LC. By combining SHG results with other techniques, we can begin to understand a microscopic picture responsible for this effect.

Last, we describe some preliminary measurements of a time-resolved spectroscopic study of the phenomenon of second harmonic generation in a gas. The construction of a 500 microjoule.pulsed, tunable laser source is described.

Acknowledgement

First, I thank Professor Y. R. Shen for being generous with his knowledge and his time. As an advisor, he is devoted to developing in his students the skills necessary to be a good scientist: the ability to set-up and work through difficult experiments, to interpret results with good physical insight, and to communicate results clearly to the scientific community. He has tremendous faith in his students which helps us to build the confidence we need to do independent research. I would also like to thank him for being able to attract scientists from all over the world, making graduate school a multi-cultural experience.

To the members of the Shen group, past and present. You are most responsible for transforming me from someone who was good at homework problems to an experimental physicist. Through you, I have learned everything from the theoretical intricacies of SHG to fixing power supplies. Most importantly, you helped me to have confidence in myself as a scientist. You are a tremendous group of scientists that have produced significant experimental results with extremely limited resources. There are several individuals who had particular impact on my graduate career: Hui Hsiung, who helped me set up my first SHG experiment, and told me what it took to get through this group; Philippe Guyot-Sionnest showed it was possible to work 15 hour days and still being a decent human being; Wei Chen, an outstanding scientist and friend, with whom I shared many long days and nights of looking for allen wrenches, impersonating stepping motors , and discussing where we belong in the world; Xu Dong Xiao, a wonderfully brilliant and caring individual who constantly amazed me on breaking the limits on what is possible in lab and in life; Tom Moses for being an excellent model of a competent, efficient and careful scientist (who never failed to laugh at my jokes); Chris Mullin, with whom I battled unbelievable odds and worked in one of the most unpleasant environmental conditions and made this laser work. He is an impressive experimental scientist, even if he is a spaz. To

the new scientists, especially my good friend John O'Brien, who need to carry on the tradition (though I recommend starting some new ones) - mazol tov.

I owe a special acknowledgement to Rich Superfine. We have helped each other go from being first years confused about what it takes to be a physicist to two individuals with Ph. D.s still confused about what it takes to be a physicist. I can honestly say, I would not have made it if it hadn't been for his inspiration and support. He is a thorough, hardworking, clear-thinking scientist whose enthusiasm for research kept the groups spirit from being completely bogged down with intermittently working Apple II computers and temperamental lasers. The day he left, the department became a bit quieter and the group meetings lost their spirit (though they became significantly shorter).

I thank Rita Jones for being such a talented and competent assistant to Ron and for being my friend. She understands better than anyone what it takes to get through this group and is generous with her advice and support.

I would like to thank two outstanding chemists/laser jocks/therapists Steve Doig and Phil Reed for building this amplifier before we did on an even tighter budget. I also want to thank Professor Roger Falcone and his group for their technical support (both knowledge and equipment) and for listening to my constant complaints about my YLF laser. I would also like to thank the Subo Ko and Jenkin Richard, who, as undergraduates, helped at various stages of the construction.

I acknowledge the physics department staff; from the custodial staff to the machine shop, you are all extremely competent and supportive and are fundamental to progress in our research, as well as extremely friendly. I offer a special acknowledgement to Frances for bearing with me in the early mornings before I had my coffee.

There are many friends within the department I would like to thank for our years of codependency: Larry Wald for the endless support both experimentally and emotionally, Mary Silber and Kanwal Singh for being my friends, Eve Ostriker for being cool, John Close and Seamus Davis for helping me keep perspective on how truly miserable I was. I

also want to thank the women of the department for being women in the department. Your very existence was a constant source of support for me.

I owe a special thanks to the bubbas: Eric Gingold, **Dr. Carl Mears**, Steve Weiss, Melissa Schoen, and Simon Verghese for getting me out of the lab, whether it be to play ultimate, go camping, listen to music, drink coffee or write email. Both individually, and as a group, you taught me to respect myself as a person and made it impossible for me to feel lonely.

Last, I acknowledge the women and men of the U. C. Berkeley Ultimate team. I would be a much less complete person if you didn't exist. I especially thank two soon-to-be-real-doctors Panna Lossy and Judy Ungerleider for sharing their tremendous energy for life, and thereby changing mine.

For financing four years of my research, I acknowledge an AT&T Doctoral Fellowship.

Table of Contents

I. Introduction

In the last 15 years, much progress has been made in the study of surfaces and interfaces. Much of this can be attributed to the development of a wide variety of experimental techniques.[1,2] However, many surface techniques are limited in their versatility. The application of optical techniques to the study of surfaces has many advantages.[3] Optical techniques can probe any interface that is accessible by light, while many other surface science techniques are restricted to surfaces in ultrahigh vacuum chambers. Because their frequency can be tuned, lasers can be used to do spectroscopy. Also, lasers are capable of producing short pulses of radiation, which allows for time-resolved studies of surfaces. Though there has been significant progress in the field of linear optics,[4,5] these techniques inherently lack surface specificity; that is, they lack the ability to discriminate between a signal from a surface and that from the bulk of the material. Linear optical techniques also often lack the sensitivity to monitor monolayer or submonolayer processes.

These difficulties are avoided with the application of second harmonic generation (SHG) to surfaces and interfaces.[6] In addition to sharing the advantages of optical techniques, SHG has been demonstrated to be surface specific and to have submonolayer sensitivity for a wide variety of systems. The technique has been applied to the study of electrical and structural properties of a metal, semiconductor and insulator surfaces in a wide variety of environments,[7] and it has been used to induce and monitor a variety of surface processes, including surface melting[8,9], desorption[10] and diffusion.[11] It has also been used to study the orientation[12] and chemistry[13] of molecular monolayers on solid and liquid surfaces. In this thesis, we continue to explore the wide variety of interfacial problems that can be probed with surface SHG.

The surface specificity of SHG relies on the symmetry properties of the process. Second harmonic generation is a second order nonlinear process, which implies that in the

dipole approximation, it is not allowed in media with inversion symmetry. At the surface of a centrosymmetric material, the inversion symmetry is broken and SHG is allowed. This has been the basis of surface second harmonic experiments to date. We asked the question, is it possible to observe second harmonic light generated at the surface of a noncentrosymmetric material? In principle, if the surface has *different* symmetry than the bulk, then through a careful selection of input and output field polarizations, we should be able to isolate a surface SHG signal by discriminating against the bulk signal. In Chapter III, we describe how we extended the technique of optical second harmonic generation to surfaces of media of non-centrosymmetric materials by demonstrating the technique on gallium arsenide,[14] an important material for applied and fundamental research.[15] A surface probe of GaAs would make it possible to study important interfacial processes like the formation of Shottky barriers,[16] passivation or molecular beam epitaxy.

We have also extended the application of surface SHG to measure the orientational distribution function of a molecular monolayer. Second harmonic generation is ideally suited to study molecular orientation. It has the sensitivity to detect submonolayer coverages and has the interface specificity that allows us to probe these monolayers in a variety of environments. SHG also has the ability to measure many aspects of the orientation of a monolayer: it can be used to determined the existence and direction of polar ordering;[17, 18] it can measure the orientation of molecules with respect to the surface normal;[12, 19] and by probing SHG as a function of surface orientation, it can yield information about the azimuthal ordering of a molecular monolayer.[20, 21, 22] SHG has been used to study a variety of properties of molecules at a water surface,[23] including orientational phase transitions[24, 25] and dynamical properties of adsorption. Examples of systems where our understanding of monolayer structures is critical to the development of new technologies are films prepared by Langmuir-Blodgett techniques[26] and liquid crystal systems.

We have used these properties of SHG to study liquid crystal monolayers in both the absence and presence of a bulk of liquid crystal molecules.[20, 21] Liquid crystals are a class of materials that possess a symmetry between an ordinary isotropic fluid and a crystalline solid. We studied three phases of the particular liquid crystal we used: an isotropic phase, which behaves as an ordinary fluid; a nematic phase which is characterized by orientational ordering of the molecules; and a smectic A phase which is characterized by orientational ordering and a periodic layer structure along one direction. It has been demonstrated that it is possible to create a large mono-domain of aligned liquid crystal molecules by placing the material in contact with an appropriately-treated substrate.[27] These interfaces are interesting because they are not only fundamental to LC-display or LC electro-optic technologies, but also because they are an example of the fascinating phenomenon of surface-induced alignment. By studying the orientation of the molecules in the interfacial monolayer we can begin to understand what is happening near the interface that allows these surfaces to induce an alignment in the bulk.

We have used SHG to study two interesting problems in interfacial liquid crystal physics. In Chapter IV, we describe the thorough investigation we have done of the mechanisms responsible for parallel aligned LC cells. Two different surface-originated mechanisms are found to be effective in aligning a homogeneous liquid crystal film: one is based on molecular interaction at the interface and the other on the elastic interaction of the bulk liquid crystal. In Chapter V, we discuss some experiments we did to study the surface memory effect, an effect seen at LC-polymer interfaces which is an interesting manifestation of the LC-polymer interactions.[28] The surface memory effect is a breaking of the isotropic symmetry of a surface by placing it in contact with an anisotropic material. In both cases, we were able to study these processes on a microscopic level, allowing us to begin to understand these interfacial phenomena on a fundamental level.

We can take advantage of the frequency selectivity of lasers and their ability to generate short pulses to do a time-resolved SHG spectroscopy experiment. To do this, we

need an energetic, tunable, picosecond laser source. The construction of a 500 microjoule/pulse, 2 picosecond, tunable laser source is described in Chapter VI. The first problem to which we have chosen to apply this laser is the still poorly understood phenomenon of SHG in atomic vapors. In Chapter VII, we describe preliminary correlation measurements we have done to determine the time scale of the process responsible for breaking the symmetry of the vapor, allowing the coherent generation of second harmonic photons.

References

[1]M. Prutton, *Surface Physics* (Oxford University press, Oxford, 1983).

[2]G. Somorjai, *Chemistry in Two Dimensions: Surfaces* (University Press, Ithaca, New York, 1981).

[3]F. R. Assenegg, A. Leitner, M. E. Lippitsch, *Surface Studies with Lasers* (Springer-Verlag, Berlin, 1983).

[4]D. E. Aspnes, A. A. Studna, Phy. Rev. Lett. **54**, 1956 (1985).

[5]A. A. Aspnes, *et al.*, Phys. Rev. Lett. **64**, 192 (1990).

[6]Y. R. Shen, Nature **337**, 137 (1989).

[7]G. Richmond, Surf. Sci. (1991).

[8]H. W. K. Tom, G. D. Aumiller, C. H. Brito-Cruz, Phys. Rev. Lett **60**, 1438 (1988).

[9]C. V. Shank, R. Yen, C. Hirlimann, Phys. Rev. Lett. **51**, 900 (1983).

[10]X. D. Zhu, (University of California, Berkeley, 1990),

[11]X. D. Xiao, X. D. Zhu, W. Daum, Y. R. Shen, submitted to Phys. Rev.B (1991).

[12]T. F. Heinz, H. W. K. Tom, Y. R. Shen, Phys. Rev. A **28**, 1883 (1983).

[13]X. D. Xiao, V. Vogel, Y. R. Shen, G. Marowsky, J. Chem. Phys. **94**, 2315 (1991).

[14]T. Stehlin, M. Feller, P. Guyot-Sionnest, Y. R. Shen, Opt. Lett. **13**, 389 (1988).

[15]M. H. Brodsky, Sci. Amer. **February, 1990**, 68 (1990).

[16]G. Jezequel, A. Taleb-Ibrahimi, R. Ludeke, F. Schaffler, J. Vac. Sci. Technol. A **6**, 1561 (1988).

[17]K. Kemnitz, *et al.*, Chem. Phys. Lett. **131**, 285 (1986).

[18]H. Hsuing, *et al.*, J. Chem. Phys. **87**, 3127 (1987).

[19]E. S. Peterson, C. B. Harris, J. Chem. Phys. **91**, 2683 (19891).

[20]M. B. Feller, W. Chen, Y. R. Shen, Phys. Rev. A **43**, 6778 (1991).

[21]W. Chen, M. B. Feller, Y. R. .Shen, Phys. Rev. Lett. **63**, 2665 (1989).

[22]G. Marowsky, G. Lupke, R. Steinhoff, L. Chi, D. Mobius, Phys. Rev. B **41**, 4480 (1990).

[23]V. Vogel, Y. R. Shen, Ann. Rev. Mat. Sci. **21**, 515 (1991).

[24]T. Rasing, M. W. Kim, Y. R. Shen, S. Grubb, Phys. Rev. Lett. (1985).

[25]T. Rasing, Y. R. Shen, M. W. Kim, P. Valent, J. Bock, Phys. Rev. A **31**, 537 (1985).

[26]V. Mizrahi, G. I. Stegeman, W. Knoll, Chem. Phys. Lett. **156**, 392 (1989).

[27]J. Cognard, Mol. Cryst. Liq. Cryst. **51**, 1 (1982).

[28]N. A. Clark, Phys. Rev. Lett. **55**, 292 (1985).

II. General Considerations of Interface Optical Second-Harmonic Generation

A. Formalism

In this section, we will outline how one can study an interface using the technique of second harmonic generation. We will first present the general formalism used to describe the experimental results throughout the thesis; the specific aspects of SHG needed to analyze a particular system is saved for the individual chapters describing those experiments. Derivations for the equations presented here are described in detail in several sources.[1-3]

It has been demonstrated that if you shine an intense optical light at a surface, it is possible to generate a nonlinear polarization that radiates at twice the frequency of the incident field in both the transmitted and reflection directions. This nonlinear polarization can be related to the incident fields through a tensor product between the incident field within the medium and the nonlinear susceptibility $\chi^{(2)}$:[4]

$$P(2\omega) = \chi^{(2)}(2\omega = \omega + \omega) : E(\omega)E(\omega) \qquad (1)$$

$\chi^{(2)}$ is a material parameter that contains the information about the system we want to measure.

Assume we have a dipole sheet with polarization P^S radiating into a dielectric medium of dielectric constant ε_m. From classical electrodynamics, the expression for the field radiated by this sheet of polarization is given by[2, 5]

$$E'(\Omega) = \frac{2\pi i \Omega \sec\theta_m}{c\sqrt{\varepsilon_m}} P^S \cdot \hat{e}(\Omega)\, e^{i(k_m \cdot r - \Omega t)} \qquad (2)$$

where θ_m is defined in Fig. 1, and $\hat{e}(\Omega)$ is the unit polarization vector for the outgoing field. If we sandwich this polarization sheet between two different dielectric media (described by ε_1 and ε_2), we create an interface (see Fig. 1). The laser beam is incident and the reflected SH output is detected in Medium 1. Only the interface and Medium 2 are assumed to have a nonlinear optical response. To take into account the reflection and refraction of the radiation generated by the polarization sheet that occurs at the interface, we multiply Eq. 2 by a geometric correction factor, $L(\Omega)$, called a macroscopic local field factor, to obtain

$$E'(\Omega) = \frac{2\pi i \Omega \sec\theta_m}{c\sqrt{\varepsilon_m}} P^S \{L(\Omega) \cdot \hat{e}(\Omega)\} e^{i(k_m \cdot r - \Omega t)} \qquad (3)$$

The explicit forms of $\hat{e}(\Omega)$ and $L(\Omega)$ are presented later in the text, in Eq. 6 and Eq. 7, respectively.

The measured SHG signal is proportional to the power of the second harmonic field. To be consistent with the formalism used in *The Principles of Nonlinear Optics,*[4] we use the convention

$$E = E_o e^{i\omega t} + E_o^* e^{-i\omega t}$$
$$= 2\mathrm{Re}\left\{ E_o e^{-i\omega t} \right\}$$

where E_o is the amplitude of the field. This leads to an expression for the intensity which is given by

$$I = \frac{c}{2\pi}\sqrt{\frac{\varepsilon}{\mu}}|E_o|^2 \qquad (4)$$

Substituting into Eq. 1 and 3 into Eq. 4, we get an expression for the second harmonic power measured . In units of photons/pulse, the SH signal is given by

$$S = \frac{32\pi^3\omega^2\sec^2\theta_1(2\omega)}{c^3\sqrt{\varepsilon_1(2\omega)\,\varepsilon_1(\omega)}}\,|\chi^{(2)}_{eff}|^2\, I^2_\omega\, TA \qquad (5)$$

where I_ω is the intensity of the incident laser beam, T is the laser pulsewidth, A is the area of the laser spot on the surface, $\varepsilon_1(\Omega)$ is the dielectric constant of medium 1 at frequency Ω ($\Omega = 2\omega$ or ω), $\theta_1(2\omega)$ is the SH reflection angle, and $\chi^{(2)}_{eff}$ is the effective nonlinear susceptibility. $\chi^{(2)}_{eff}$ has the form

$$\chi^{(2)}_{eff} = \{\hat{e}(2\omega)\cdot L^{(r)}(2\omega)\}\,\chi^{(2)}:\{L(\omega)\cdot\hat{e}(\omega)\}\{L(\omega)\cdot\hat{e}(\omega)\}$$

where $\hat{e}(\Omega)$ are unit polarization vectors for $\Omega = \omega$ or 2ω and $L(\Omega)$ are the appropriate local field factors. The polarization vectors for the incident beam and SH beam propagating in the reflected direction, as defined in the lab coordinates of Fig. 2, are given by

$$\hat{e}_i(\omega) = \{-\cos\theta_1(\omega),\, 0,\, \sin\theta_1(\omega)\} \qquad (6)$$
$$\hat{e}_r(2\omega) = \{\cos\theta_1(2\omega),\, 0,\, \sin\theta_1(2\omega)\}$$

for p-polarization, and

$$\hat{e}_i(\omega) = \hat{e}_r(2\omega) = \{0,\, 1,\, 0\}$$

for s-polarization. For the transmitted beam, the polarization vectors for p-polarized light are given by

$$\hat{e}_i(\omega) = \{-\cos\theta_1(\omega), 0, -\sin\theta_1(\omega)\} \qquad (6)$$

$$\hat{e}_r(2\omega) = \{\cos\theta_1(2\omega), 0, -\sin\theta_1(2\omega)\}$$

and the s-polarization is the same as for the reflected beam. The local field factors (or Fresnel coefficients), $L(\Omega)$ (where $\Omega=\omega$ for the incident field and $\Omega=2\omega$ for the SH field), take into account the reflection, refraction and enhancement of the fields due to the presence of the interface. Note, in an experiment, the quantity measured is $\chi^{(2)}_{eff}$. In order to determine accurately the values of the components of $\chi^{(2)}$, we must calculate the macroscopic local field corrections to the incident laser fields and to the SH field generated at the interface.

The form of the macroscopic local field factors will depend on the details of the particular interface under study. A detailed derivation of the local field factors for the general case of a polarization sheet sandwiched between two infinite bulk media is presented in Reference 3. It shows that the local field factors at the fundamental frequency relating the input field $E_{laser}(\omega)$ in medium 1 to the corresponding field components in the polarization sheet, $E_{source}(\omega)$ are given by:[1]

$$L_{xx}(\omega) = \frac{E_{source}}{E_{laser}}\Big|_x = \frac{2n_1(\omega)\cos\theta_2}{n_2(\omega)\cos\theta_1 + n_1(\omega)\cos\theta_2},$$

$$L_{yy}(\omega) = \frac{E_{source}}{E_{laser}}\Big|_y = \frac{2n_1(\omega)\cos\theta_1}{n_1(\omega)\cos\theta_1 + n_2(\omega)\cos\theta_2},$$

$$L_{zz}(\omega) = \frac{E_{source}}{E_{laser}}\Big|_z = \frac{2n_1^2(\omega)n_2(\omega)\cos\theta_1}{n_m^2(\omega)\{n_2(\omega)\cos\theta_1 + n_1(\omega)\cos\theta_2\}}, \qquad (7)$$

where n_1, n_2, n_m are indices of refraction of the media 1 and 2 and the polarization sheet, respectively, with $n_i(\Omega)= \sqrt{\varepsilon_i(\Omega)}$.

The output local field factors are defined in Eq. 3, where all the geometric factors resulting from the reflection and refraction of the SH field at the interface are contained in $L(2\omega)$. The wavevector of the radiation at 2ω has components along both the positive and negative z-axes. Their directions are determined by the constraint imposed by conservation of the tangential component of the wavevectors. In the reflection direction (along the negative z-axis), the output local field factors $\{L_{ii}(2\omega) = L_{ii}^{R}(2\omega)\}$ have the exact same form as that of the input local field factors of Eq. (7), using the values of the indices of refraction at 2ω. In the transmitted direction (along the positive z-axis), the output local field factors $\{L_{ii}(2\omega) = L_{ii}^{T}(2\omega)\}$ also have the same form as Eq. (7) if we exchange subscripts *1* and *2* and use the values of the indices of refraction at 2ω.

B. Bulk contribution

Let us generalize Eq. 1 to include a contribution from the bulk of Medium 2 pictured in Fig. 1. We can account form the bulk contribution by writing an effective surface susceptibility as,[1, 3]

$$\chi_{ijk}^{eff} = \chi_{ijk}^{s} + \frac{\chi_{ijk}^{B}}{(k_z(2\omega) + 2k_z(\omega))} f_i(2\omega) f_j(\omega) f_k(\omega) \qquad (8)$$

where χ^S is the susceptibility from the interface, χ^B is the susceptibility of the bulk, $k_z(2\omega)$ and $k_z(\omega)$ are the z-components of the k-vectors in Medium 2 that describe the SH wave and the incident field, respectively, and $f(\Omega) = (1,1,\frac{\varepsilon_2(\Omega)}{\varepsilon_m(\Omega)})$. By including f in this way, we can use the same local field factors as expressed in Eq. 7. The ratio $\frac{1}{(k_z(2\omega) + 2k_{2z}(\omega))}$ is the "phasematching length" for SHG in the reflection direction. It defines the distance over which the bulk is phase-matched when monitoring with SHG,

assuming that the phasematching distance is shorter than the penetration depth of the incident fields. Writing the surface susceptibility in this way implies that we can also write an effective nonlinear polarization that includes both the surface and bulk contributions as

$$P^{eff}_{ijk} = P^{s}_{ijk} + \frac{i\,P^{B}_{ijk}}{(k_z(2\omega) + 2k_z(\omega))} f_i(2\omega)$$

The "i" factor comes about because the bulk contribution is 180 degrees out of phase with the surface contribution. The derivation of this expression is based on continuity of the fields across the interface, and has been worked out in detail elsewhere.[3]

The expression given in Eq. 1 only includes the dipole contribution to the nonlinear polarization. There are higher-order multipole contributions to both the surface and bulk nonlinear polarizations. For the surface polarization, the higher-order contributions are due to discontinuities in the field and discontinuities in the susceptibilities at the interface; for the bulk, they are due to gradients in the fields and susceptibilities within the bulk of the material. In general, these higher order terms are included in the nonlinear polarization in the following way:[6]

$$P^{(2)}_{total}(2\omega) = P^{(2)}(2\omega) - \nabla \cdot Q^{(2)}(2\omega) + \frac{c}{i2\omega} \nabla \times M^{(2)}(2\omega) + \ldots.$$

with

$$P(2\omega) = \chi^{D} : E(\omega)E(\omega) + \chi^{P} : E(\omega)\nabla E(\omega)$$

$$Q(2\omega) = \chi^{Q} : E(\omega)E(\omega)$$

$$M(2\omega) = \chi^{M} : E(\omega)E(\omega)$$

to first order in the gradient of the incident fields. Physically, we can think of these difference susceptibilities in the following way: χ^D corresponds to the dipole response of the material to the field; χ^P corresponds the dipole response to the gradient of the field; and χ^Q and χ^M correspond to the quadrupole and magnetic dipole response to the gradient of the field, respectively. The polarization can be written as[7,8]

$$P^{(2)}_{total}(2\omega) = \chi^D : E(\omega)E(\omega) + \chi^P : \nabla\{E(\omega)E(\omega)\} - \nabla\{\chi^Q : E(\omega)E(\omega)\} \qquad (9)$$

These contributions were derived from first principles in Reference 6. An interesting term came from this derivation that had not been elucidated in the earlier surface SHG literature; namely a term arises from the difference in the bulk susceptibility across the interface that is described by

$$\{\nabla\chi^Q\}\, E(\omega)E(\omega) = \left\{\frac{\chi^Q_1}{\varepsilon_1} - \frac{\chi^Q_2}{\varepsilon_2}\right\} E(\omega)E(\omega) \qquad (10)$$

This term is interesting in that it depends only on bulk parameters but is a "surface term" in the sense that it exists because of the discontinuity across an interface. This term will become important in Chapters IV and V of this thesis, when we discuss the bulk contribution in liquid crystal systems.

C. General Symmetry Properties of Second Harmonic Generation

The experiments described in this thesis exploit the symmetry properties of SHG. In the past, several experiments have been conducted that have used symmetry properties to obtain information about their systems. The nonlinear susceptibility , $\chi^{(2)}_{ijk}(2\omega)$, is a second rank tensor whose symmetry is determined by the symmetry properties of the

material. It has 27 independent components. We can reduce the number of these components by applying the symmetry properties of the system. If the system has inversion symmetry, like a centrosymmetric crystal, then all of the components of $\chi^{D}(2\omega)$ are identically zero. Note, $\chi^{P}(2\omega)$ and $\chi^{Q}(2\omega)$ are fourth rank tensors and, hence, are not forbidden by any crystal symmetry. If a surface is isotropic (which, for a second rank tensor, implies that it has 2 mirror plane or higher symmetries), there are only three independent non-zero contributions, namely

$$\chi_{zzz}$$

$$\chi_{zxx} = \chi_{zyy}$$

$$\chi_{xxz} = \chi_{xzx} = \chi_{yzy} = \chi_{yyz}$$

An extensive exploration of the symmetry characteristics of the $\chi_{B}^{(2)}(2\omega)$ is given in Chapter 2 of *The Principles of Nonlinear Optics* [4] and a list of the components for the surface susceptibility tensor for a variety of surface symmetries is given in Reference 9.[9]

In general, the detected SHG will have contributions from a linear combination of components of the nonlinear susceptibility χ. Sometimes it is possible to access individual components through proper selection of the polarization of the incident optical field and the outgoing second harmonic field and the orientation of the material. In Chapter III, we use the symmetry properties to isolate the surface contribution from the bulk as shown in Eq. 10 above. In Chapters IV and V we use the symmetry properties to maximize the information we can obtain about the orientation of molecules at an interface.

References

[1]Y. R. Shen, Annu. Rev. Phys. Chem. **40**, 327 (1989).

[2]T. F. Heinz, (University of California, Berkeley, 1982),

[3]H. W. K. Tom, (University of California, Berkeley, 1984),

[4]Y. R. Shen, *Principles Of Nonlinear Optics* (Wiley, New York, 1984).

[5]Y. R. Shen, Ann. Rev. Mater. Sci. **16**, 69 (1986).

[6]N. Bloembergen, R. K. Chang, S. S. Jha, C. H. Lee, Phys. Rev. **174**, 813 (1968).

[7]P. Guyot-Sionnest, Y. R. Shen, Phys. Rev. B **38**, 7985 (1988).

[8]P. Guyot-Sionnest, Y. R. Shen, Phys. Rev. B **35**, 4420 (1987).

[9]P. Guyot-Sionnest, W. Chen, Y. R. Shen, Phys. Rev. B **33**, 8254 (1986).

Figure Captions

Figure 1: Coordinate system used for formalism presented in this chapter.

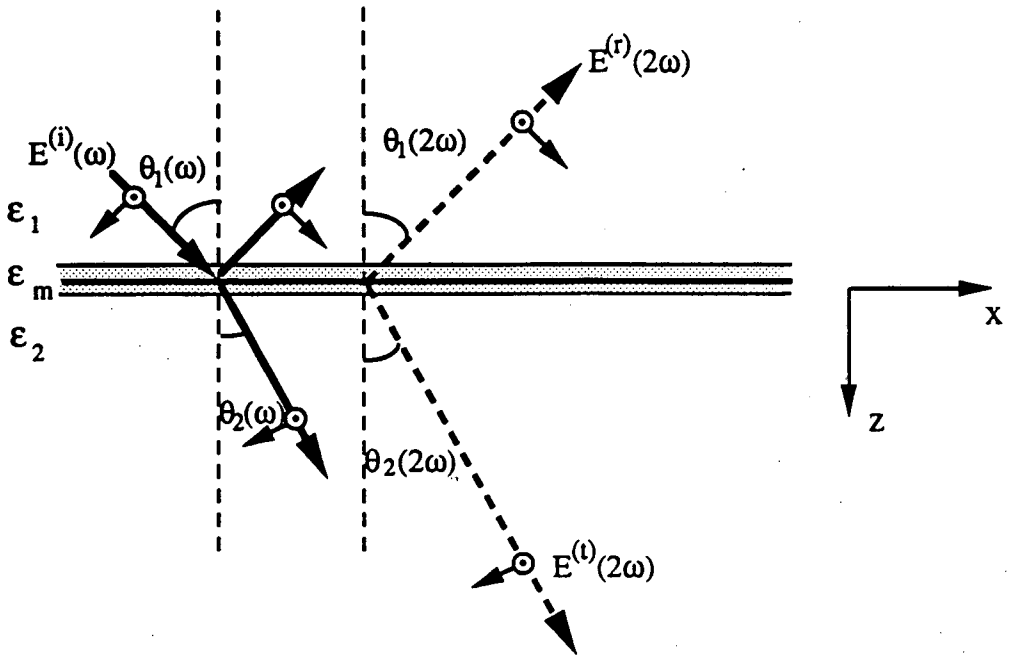
E(r)(2ω)
E(i)(ω)
θ1(ω)
θ1(2ω)
ε1
εm
ε2
θ2(ω)
θ2(2ω)
E(t)(2ω)
x
z

III. Surface Second Harmonic Generation from a Noncentrosymmetric Medium

A. Introduction

In recent years, optical second harmonic generation (SHG) has proven to be a very effective and sensitive tool for obtaining information about structural and electronic properties of metal and semiconductor surfaces.[1, 2] However, experiments so far have been restricted to substrates with inversion symmetry, since then SHG is forbidden in the bulk but allowed at the surface, giving this technique its unique surface specificity. In this experiment, we showed that with proper polarization combinations, this restriction to media with inversion symmetry can be relaxed.[3] Thus, SHG can be used as an effective surface probe for all interfaces accessible by light. For demonstration, we have studied with SHG the adsorption of Sn on GaAs.

Semiconductor - metal interfaces are of great interest in fundamental as well as applied semiconductor research. The formation of Schottky barriers by metal overlayers on GaAs has been a subject of much concern.[4] The lack of successful theoretical descriptions of such interfaces and their electronic structure requires new and independent experimental studies.[5, 6] Surface SHG, unlike other optical techniques such as photoemission spectroscopy,[7, 8] ellipsometry, [9] and reflectivity measurements,[10] is capable of probing material properties of higher order, thus having the possibility of deducing new information about an interface. In addition, with short-pulse lasers, it allows time and frequency resolved probing of surface and interface processes.[2]

B. Theory: Polarization Discrimination of Bulk Contribution

We consider here SHG in reflection from a vacuum/solid interface. As we showed in Chapter II, Eq. 3, the SH-field generated at an interface can be written as :

$$\mathbf{E}(2\omega) = \frac{4\pi i\omega \sec\theta_m(2\omega)}{c\sqrt{\varepsilon_m}} \mathbf{P}^S \left[\mathbf{L}(2\omega) \cdot \hat{\mathbf{e}}(2\omega)\right] e^{i(\mathbf{k}_m \cdot \mathbf{r} - \Omega t)} \qquad (1)$$

where the effective nonlinear surface polarization $\mathbf{P}^S(2\omega)$ is given by:

$$\mathbf{P}^S(2\omega) = \chi^{(2)}_{surf} : \mathbf{E}(\omega)\mathbf{E}(\omega)[\mathbf{L}(\omega) \cdot \hat{\mathbf{e}}(\omega)][\mathbf{L}(\omega) \cdot \hat{\mathbf{e}}(\omega)]$$
$$+ \chi^{(2)}_{bulk} : \mathbf{E}(\omega)\mathbf{E}(\omega)[\mathbf{L}(\omega) \cdot \hat{\mathbf{e}}(\omega)][\mathbf{L}(\omega) \cdot \hat{\mathbf{e}}(\omega)]\, L_{eff}$$

$\chi^{(2)}_{surf}$ and $\chi^{(2)}_{bulk}$ are the surface and bulk nonlinear susceptibility tensors, respectively, $\mathbf{L}(\omega)$ and $\mathbf{L}(2\omega)$ are the Fresnel factors for the incident input and output fields, and $L_{eff} = \frac{1}{(k_\omega + k_{2\omega})}$ is the effective phase-matching distance in the bulk substrate for the reflected SHG.

In media with inversion symmetry, $\chi^{(2)}_{bulk}$ vanishes in the electric-dipole approximation, and the $\chi^{(2)}_{surf}$ term may dominate, making SHG surface specific. This is not the case for media without inversion symmetry, like gallium arsenide. However, the symmetry of the bulk is generally *different* from the symmetry of the surface. It is then possible to choose an experimental geometry with selected polarization combinations to effectively suppress the dipole-allowed $\chi^{(2)}_{bulk}$. GaAs is a cubic crystal with 43m bulk symmetry. This implies there is only one independent, nonzero element of $\chi^{(2)}_{bulk}$ is $\chi^{(2)}_{xyz}$

$=\chi^{(2)}_{yzx}=\chi^{(2)}_{zxy}$, with x,y,z referring to the crystalline coordinate system. We want to compare the symmetry of these bulk tensor components with the components of the surface nonlinear susceptibility for three different faces of GaAs, namely the (100), (110), and the (111) faces. The nonzero components of the $\chi^{(2)}_{surface}$ for these three faces are listed in the second column of Table 4.

To find experimental geometries which allow one to distinguish between bulk and surface contributions, we needed to find an orientation of the crystal and a combination of input and output polarizations which would discriminate against a bulk contribution but allow for detection of a surface contribution. The coordinate systems we used to do the analysis is shown in Fig. 1. There are three coordinate systems of interest: the lab coordinates (x,y,z) which are defined by the plane of incidence being in the x-z plane and z being normal to the sample surface; the sample coordinates (x', y', z') which are defined by x' being parallel to the projection of the (100) crystal axis onto the surface and z' is the surface normal; and the crystal coordinates (x", y", z"). The sample orientation is defined in the plane of the crystal surface with $\Omega=0^{\circ}$ corresponding to x' parallel to x. The coordinate transformation from the lab coordinates to the sample coordinates are given in Table 1a. The transformations between the crystal coordinate system and the sample coordinate system are given for three faces of GaAs in Table 1b.

Since the signal generated by the bulk is a few orders of magnitude larger than the signal from the surface, there is no hope of distinguishing the two in regions when the bulk is nonzero. By studying the dependence of the bulk and surface contributions on a rotation of the sample, we were able to extract the combinations of polarization and sample orientation which allow access to diverse $\chi^{(2)}_{surface}$-elements with the bulk contribution

suppressed. To calculate how rotating the sample affects the bulk contributions, I used the following recipe:

1. Transform nonlinear polarization P_i from lab coordinate system to sample coordinate system using the transformations given in Table 1a.

2. Transform $P_{i'}$ from sample coordinates to crystal coordinates using the transformations given in Table 1b.

3. Substitute in appropriate $\chi^{(2)}_{i"j"k"}$ $E_{j"}$ $E_{k"}$'s for the nonlinear polarizations now written in the crystal coordinates.

4. Transform fields from crystal coordinates to sample coordinates.

5. Transform fields from sample coordinates to original lab coordinates

To calculate how the surface contributions depend on orientation of the sample, the same approach is used, except that step 2 can be eliminated.

To simplify the calculation, we were able to condense all the geometric factors which did not depend on the orientation of the crystal into one term, G

$$G \equiv [L(\omega)\cdot\hat{e}(\omega)][L(\omega)\cdot\hat{e}(\omega)][L(2\omega)\cdot\hat{e}(2\omega)]\ \frac{\sec\theta(2\omega)}{c}$$

for the surface terms, and

$$G \equiv [L(\omega)\cdot\hat{e}(\omega)][L(\omega)\cdot\hat{e}(\omega)][L(2\omega)\cdot\hat{e}(2\omega)]\ \frac{\sec\theta(2\omega)}{\sqrt{\varepsilon_{GaAs}}\,c}L_{eff}$$

for the bulk terms. G depends on the angle of incidence, and the indices of refraction for the system. $L(\Omega)$ and $e(\Omega)$ are defined in Chapter 2 equations 6 and 7 respectively, with

$n_1(\Omega) = n_{air}(\Omega)$, and $n_2(\Omega) = n_{GaAs}(\Omega)$ for $\Omega = \omega$ for the incident fields and $\Omega = 2\omega$ for the SH-field. For example, if the experimental geometry is chosen to look at the s-in/s-out polarization, the geometrical term for the surface contribution would be

$$G_{yyy} = [L_y(\omega)\,\hat{e}_y(\omega)]^2[L_y(2\omega)\,\hat{e}_y(2\omega)]\,\frac{\sec\theta(2\omega)}{c}$$

The bulk contributions to the effective surface nonlinear polarization as a function of the crystal orientation are listed for different crystal faces in Table 2. The contributions from the surface susceptibilities are listed in Table 3. For each crystal face, we chose a geometry that led to a zero bulk contribution and checked to see the which components of the surface susceptibility were nonzero. Table 4 summarizes the results. It shows all the nonzero elements of the surface susceptibility tensor $\chi^{(2)}_{surface}$ for the (100), (110) and (111) faces of GaAs and the possible geometries for their determination by SHG.

C. Experimental Results on GaAs

We used SHG from GaAs (100) to demonstrate the feasibility of surface studies on non-centrosymmetric media. The crystals were grown by the "horizontal electro dynamic gradient freeze" technique and cut in the (100) orientation. The polished samples were etched with a mixture of H_20, H_2O_2, and NH_3OH (10:1:1) and placed in an ultrahigh-vacuum chamber with a base pressure below 10^{-9} Torr. The crystal was then heated to 280°C to further clean the surface. For the experiment, we used a Q-switched and mode-locked Nd:YAG laser (Quantronix Model 417) with a fundamental frequency at 1.06 μm and an angle of incidence of 70°. The SHG signal was detected using a standard photon

counting technique which involved the using home-built gated electronics interfaced with an IBM computer.

To demonstrate the surface sensitivity of the technique, we used SHG to monitor the adsorption of Sn on GaAs. The metal was evaporated in an electrically heated oven at approximately 20 cm away from the sample. The evaporation rate was monitored by a quartz balance. In a p_{in} - p_{out} polarization geometry (i.e. p-polarized input beam and p-polarized second harmonic beam) with the (100) axis in the plane of incidence, the detected SH field is easily derived from Eq. 1, using the effective nonlinear surface polarization $P^s(2\omega)$ from Table 3a:

$$E_p(2\omega) = \chi^{(2)}_{zzz} G_{zzz} E^2_z(\omega) E^2_z(\omega) + \chi^{(2)}_{zxx} G_{zxx} E^2_x(\omega) E^2_x(\omega) + \chi^{(2)}_{xxz} G_{xxz} E^2_x(\omega) E^2_z(\omega)$$

in which the $\chi^{(2)}_{zzz}$ term is dominant and the bulk dipole contribution is absent. The latter could be obtained from the p_{in} - s_{out} geometry, with (Table 2a):

$$E_s(2\omega) = \chi^{(2)}_{bulk} G_{yxz} E_x(\omega) E_z(\omega)$$

Fig. 2 shows the change of the surface SH-signal as a function of the evaporation time. The increase of the SH-signal from the clean GaAs surface to the Sn covered surface using the p_{in} - p_{out} geometry was about a factor of five, while the bulk signal from the p_{in} - s_{out} geometry did not change. This is a clear demonstration of the surface specificity of the technique. The immediate response of the SH-signal to the adsorption of Sn on GaAs at the beginning of the metal deposition shows the sensitivity of the technique in the submonolayer region.

D. Discussion

The SH-signal from Sn-covered GaAs is generated from the surface nonlinear susceptibility $\chi^{(2)}_{surface} = \chi^{(2)}_{GaAs} + \chi^{(2)}_{Sn} + \chi^{(2)}_{interaction}$. With increasing coverage, $\chi^{(2)}_{Sn}$ becomes dominant, due to the large nonlinear polarizability of the nearly free electrons of the metal [11]. In Fig.1, saturation of the SH- signal sets in after an evaporation time of approximately 30 minutes, which corresponds to an average thickness of about 10 Å of the deposited metal. It shows that already in this range of deposition a full monolayer of Sn must have been present on GaAs. This is consistent with results obtained from a detailed study of the GaAs-Sn interface [12]. By comparing the magnitude of our signal to that of a quartz reference, we calculated the surface susceptibility from the clean GaAs surface to be $\chi^{(2)}_{zzz} = 3.5 \times 10^{-15}$ esu, with the saturated value corresponding to twice that. The effective surface contribution from the bulk of GaAs is approximately $\chi^{(2)}_{effective} = \chi^{(2)}_{bulk} L_{eff} = 1 \times 10^{-12}$ esu, which is consistent with the known value of the bulk dipole susceptibility of GaAs (1×10^{-6} esu) and an effective phasematching length of $L_{eff} = 100$ Å.

To obtain more complete information about surfaces and interfaces of noncentrosymmetric media like GaAs, as many different $\chi^{(2)}_{surface}$ - components as possible should be determined. For this purpose, the relatively simple experimental technique described above can be extended. Along with the simple cases of direct determination of some $\chi^{(2)}_{surface}$ - components with certain combinations of polarizations and sample orientations, other $\chi^{(2)}_{surface}$ - components, marked with "c" or "d" in Table 4, are accessible by an interference method, in which the bulk contribution can be cancelled out by a destructive interference with the field generated from an identical sample in an inverted

orientation. Different elements of $\chi^{(2)}_{surface}$ can be deduced from measurements in different experimental geometries. In addition, anisotropic surface components are separable from isotropic surface and bulk terms by using a modulation technique [13], in which the second harmonic signal is obtained from a rotating sample with a phase sensitive detection correlated to the sample rotation frequency. Using these methods, most $\chi^{(2)}_{surface}$ elements are separately accessible. This then allows studies of structural symmetries of the surfaces and interfaces of noncentrosymmetric crystals. Surface modifications such as metal deposition and molecular adsorption can also be easily detected. With the help of tunable lasers, spectroscopic information about surface electronic structures can be obtained. The possibility of time resolved measurements, in particular, opens the door for additional studies of dynamical processes like surface states relaxations, surface reconstruction, and crystal growth, in an UHV or liquid environment.

In conclusion, we have demonstrated, using the adsorption of Sn on GaAs as an example, that SHG can be a practical tool for probing surfaces of noncentrosymmetric media. The sensitivity of this technique is in the submonolayer region. The nonvanishing elements of $\chi^{(2)}_{surface}$ could be measured by various polarization combinations and sample orientations, with perhaps the help of some interference methods. Thus, the restriction of surface SHG to centrosymmetric materials is removed.

References

[1]H. W. K. Tom, G. D. Aumiller, Phys. Rev. B **33**, 8818 (1986).

[2]T. F. Heinz, M. M. T. Loy, W. A. Thompson, Phys. Rev. Lett. **63**, (1985).

[3]T. Stehlin, M. Feller, P. Guyot-Sionnest, Y. R. Shen, Opt. Lett. **13**, 389 (1988).

[4]Surf. Sci. **168**,

[5]S. B. Zhang, M. L. Cohen, S. G. Louie, Phys. Rev. B **32**, 3955 (1985).

[6]S. B. Zhang, M. L. Cohen, S. G. Louie, Phys. Rev. B **34**, 768 (1986).

[7]R. I. G. Uhrberg, G. V. Hanson, J. M. Nickolls, S. A. Flodstrom, Phys. Rev. Lett. **48**, 1032 (1982).

[8]F. J. Himpsel, P. Heimann, D. E. Eastman, Phys. Rev. B. **24**, 2003 (1981).

[9]R. M. A. Azzam, N. M. Bashara, *Ellipsometry and Polarizaed Light* (North-Holland, Amsterdam, 1977).

[10]P. Chiradia, A. Cricenti, S. Selci, G. Chiarotti, Phys. Rev. Lett. **52**, 1145 (1984).

[11]N. Bloembergen, R. K. Chang, S. S. Jha, C. H. Lee, Phys. Rev. **174**, 813 (1968).

[12]N. Budgens, M. Luth, M. Mattern-Klossau, A. Spitzer, A. Tulke, Surf. Sci. **160**, 46 (1985).

[13]D. E. Aspnes, A. A. Studna, Phys. Rev. Lett. **54**, 1956 (1985).

Table 1a: Transformations between lab coordinates and sample coordinates

$$x' = x\cos(\Omega) - y\sin(\Omega) \qquad x = x'\cos(\Omega) + y'\sin(\Omega)$$
$$y' = y\cos(\Omega) + x\sin(\Omega) \qquad y = y'\cos(\Omega) - x'\sin(\Omega)$$
$$z' = z$$

Table 1b: Transformations between sample coordinates and crystal coordiantes

100 Face

$$x'' = -z'$$
$$y'' = y'$$
$$z'' = -x'$$

110 Face

$$x'' = \frac{1}{\sqrt{2}}(x' - y') \qquad x' = \frac{1}{\sqrt{2}}(x'' + z'')$$
$$y'' = -z' \qquad y' = \frac{1}{\sqrt{2}}(z'' - x'')$$
$$z'' = \frac{1}{\sqrt{2}}(x' + y') \qquad z' = -y''$$

111 face

$$x'' = \sqrt{\frac{2}{3}}x' - \frac{1}{\sqrt{6}}(y' + z') \qquad x' = \sqrt{\frac{2}{3}}x'' + \frac{1}{\sqrt{3}}z''$$
$$y'' = \frac{1}{\sqrt{2}}(y' - z') \qquad y' = -\frac{1}{\sqrt{6}}x'' + \frac{1}{\sqrt{2}}y'' + \frac{1}{\sqrt{3}}z''$$
$$z'' = \frac{1}{\sqrt{3}}(x' + y' + z') \qquad z' = -\frac{1}{\sqrt{6}}x'' - \frac{1}{\sqrt{2}}y'' + \frac{1}{\sqrt{3}}z''$$

Table 2: Orientational dependence of the bulk contributions of GaAs to the detected SH field, with z parallel to the surface normal and y perpendicular to the plane of incidence.

100 - face

$$E_x(2\omega) = \chi^{(2)}_{bulk}\left[G_{xzx}E_z(\omega)E_x(\omega)\cos(2\Omega) + G_{xzx}E_z(\omega)E_y(\omega)\sin(2\Omega)\right]$$

$$E_y(2\omega) = \chi^{(2)}_{bulk}\left[G_{yzy}E_z(\omega)E_y(\omega)\cos(2\Omega) - G_{yzx}E_z(\omega)E_x(\omega)\sin(2\Omega)\right]$$

$$E_z(2\omega) = \chi^{(2)}_{bulk}\left[E_x(\omega)E_y(\omega)\cos(2\Omega) + \frac{1}{2}\left(E_y^2(\omega) - E_x^2(\omega)\right)\sin(2\Omega)\right]$$

110 - face

$$E_x(2\omega)=\chi^{(2)}_{bulk}[G_{xxx}E_x^2(\omega)\left(\frac{3}{2}\sin(\Omega)\cos^2(\Omega)\right) - G_{xyy}E_y^2(\omega)\left(\frac{1}{2}\sin^3(\Omega) - \sin(\Omega)\cos^2(\Omega)\right)$$
$$+G_{xzz}E_z^2(\omega)\left(\frac{1}{2}\sin(\Omega)\right) - G_{xxy}E_xE_y\left(2\sin^2(\Omega)\cos(\Omega)-\cos^3(\Omega)\right)]$$

$$E_y(2\omega)=\chi^{(2)}_{bulk}[G_{yxx}E_x^2(\omega)\left(\frac{1}{2}\cos^3(\Omega)\right) - \cos(\Omega)\sin^2(\Omega)) + G_{yyy}E_y^2(\omega)\left(\frac{3}{2}\sin^2(\Omega)\cos(\Omega)\right)$$
$$- G_{yzz}E_z^2(\omega)\left(\frac{1}{2}\cos(\Omega)\right) + G_{yxy}E_xE_y\left(2\cos^2(\Omega)\sin(\Omega)-\sin^3(\Omega)\right)]$$

$$E_z(2\omega) = \chi^{(2)}_{bulk}\left[G_{zzy}E_z(\omega)E_y(\omega)\cos(\Omega) - G_{zzx}E_z(\omega)E_x(\omega)\sin(\Omega)\right]$$

111 - face

$$E_x(2\omega)= \chi^{(2)}_{bulk}\left[\left(G_{xxx}E_x^2(\omega) - G_{xyy}E_y^2(\omega)\right)\cos(3\Omega) + 2G_{xxy}E_x(\omega)E_y(\omega)\sin(3\Omega) - 2G_{xxz}E_x(\omega)E_z(\omega)\right)\right]$$

Table 2, cont.

$$E_y(2\omega) = \chi^{(2)}_{bulk}\left[\left(G_{yyy}E_y^2(\omega) - G_{yxx}E_x^2(\omega)\right)\sin(3\Omega) - 2G_{yxy}E_x(\omega)E_y(\omega)\cos(3\Omega) + 2G_{yyz}E_y(\omega)E_z(\omega)\right]$$

$$E_z(2\omega) = \chi^{(2)}_{bulk}\left[2G_{zzz}E_y^2(\omega) - \left(G_{zxx}E_x^2(\omega) + G_{zyy}E_y^2(\omega)\right)\right]$$

Table 3: Orientational dependence of surface contributions of GaAs to the detected SH field.

<u>100 Face</u>

$$E_x(2\omega) = \chi^{(2)}_{xxz} G_{xxz} E_x(\omega) E_z(\omega)$$

$$E_y(2\omega) = \chi^{(2)}_{yyz} G_{yyz} E_y(\omega) E_z(\omega)$$

$$E_z(2\omega) = \chi^{(2)}_{zzz} G_{zzz} E^2_z(\omega) + \chi^{(2)}_{zxx} G_{zxx} E^2_x(\omega) + \chi^{(2)}_{zyy} G_{zyy} E^2_y(\omega)$$

<u>110 Face</u>

$$\begin{aligned} E_x(2\omega) = \chi^{(2)}_{xxy}(&-G_{xxx}E^2_x(\omega)2\cos^2(\Omega)\sin(\Omega)+G_{xyy}E^2_y(\omega)2\cos^2(\Omega)\sin(\Omega) \\ &+G_{xxy}E_x(\omega)E_y(\omega)(2\cos^3(\Omega) - 2\sin^2(\Omega)\cos(\Omega)) \\ &+\chi^{(2)}_{xxz}(-G_{xxz}E_x(\omega)E_z(\omega)\, 2\cos^2(\Omega) + 2G_{xyz}E_y(\omega)E_z(\omega)\, \sin(\Omega)\cos(\Omega)) \\ &+\chi^{(2)}_{yyy}\,(G_{xxx}E^2_x(\omega)\, \sin^3(\Omega)-G_{xyy}E^2_y(\omega)\, \cos^2(\Omega)\sin(\Omega) \\ &-2G_{xxy}E_x(\omega)E_y(\omega)\sin^2(\Omega)\cos(\Omega)) \\ &+\chi^{(2)}_{yzz}G_{xzz}E^2_z(\omega)\sin(\Omega) \\ &+\chi^{(2)}_{yxx}\,(-G_{xxx}E^2_x(\omega)\, \cos^2(\Omega)\sin(\Omega)+G_{xyy}E^2_y(\omega)\sin^3(\Omega) \\ &-2G_{xxy}E_x(\omega)E_y(\omega)(2\sin^2(\Omega)\cos(\Omega)) \\ &+\chi^{(2)}_{yyz}(-G_{xxz}E_x(\omega)E_z(\omega)\, 2\, \sin^2(\Omega) - 2G_{xyz}E_y(\omega)E_z(\omega)\, \sin(\Omega)\cos(\Omega)) \end{aligned}$$

Table 3, cont.

$$E_y(2\omega) = \chi^{(2)}_{yzz} G_{yzz} E_z^2(\omega)\cos(\Omega)$$

$$+\chi^{(2)}_{yxx}(G_{yxx}E_x^2(\omega)\cos^3(\Omega)+G_{yyy}E_y^2(\omega)\sin^2(\Omega)\cos(\Omega)$$

$$+2G_{yxy}E_x(\omega)E_y(\omega)\cos^2(\Omega)\sin(\Omega)$$

$$+\chi^{(2)}_{yyy}\,(G_{yxx}E_x^2(\omega)\,\sin^2(\Omega)\cos(\Omega)+G_{yyy}E_y^2(\omega)\,\cos^3(\Omega)$$

$$+2G_{yxy}E_x(\omega)E_y(\omega)\cos^2(\Omega)\sin(\Omega))$$

$$+\chi^{(2)}_{yyz}(G_{yyz}E_y(\omega)E_z(\omega)\,2\cos^2(\Omega) - 2G_{yxz}E_x(\omega)E_z(\omega)\,\sin(\Omega)\cos(\Omega))$$

$$+\chi^{(2)}_{xxy}\,(-G_{yxx}E_x^2(\omega)\,2\sin^2(\Omega)\cos(\Omega)+G_{yyy}E_y^2(\omega)\,2\sin^2(\Omega)\cos(\Omega)$$

$$+2G_{yxy}E_x(\omega)E_y(\omega)(2\cos^2(\Omega)\sin(\Omega) - 2\sin^3(\Omega))$$

$$+\chi^{(2)}_{xxz}(G_{yxz}E_x(\omega)E_z(\omega)\,2\,\sin(\Omega)\cos(\Omega) + 2G_{yyz}E_y(\omega)E_z(\omega)\,\sin^2(\Omega))$$

$$E_z(2\omega) = \chi^{(2)}_{zzz} G_{zzz} E_z^2(\omega)$$

$$+\chi^{(2)}_{zyy}(G_{zxx}E_x^2(\omega)\sin^2(\Omega)+G_{zyy}E_y^2(\omega)\,\cos^2(\Omega) - 2E_x(\omega)E_y(\omega)\cos(\Omega)\sin(\Omega))$$

$$+\chi^{(2)}_{zxx}(-G_{zxx}E_x^2(\omega)\,\cos^2(\Omega) + G_{zyy}E_y^2(\omega)\,\sin^2(\Omega) + 2E_x(\omega)E_y(\omega)\cos(\Omega)\sin(\Omega))$$

$$+\chi^{(2)}_{zyz}(-G_{zxz}E_x(\omega)E_z(\omega)\,2\sin(\Omega) + G_{zyz}E_y(\omega)E_z(\omega)\,2\cos(\Omega))$$

<u>111 Face</u>

$$E_x(2\omega) = \chi^{(2)}_{xxx}\left[\left(G_{xxx}E_x^2(\omega) - G_{xyy}E_y^2(\omega)\right)\cos(3\Omega) + 2G_{xxy}E_x(\omega)E_y(\omega)\sin(3\Omega) + 2G_{xxz}E_x(\omega)E_z(\omega)\right]$$

$$E_y(2\omega) = \chi^{(2)}_{yyx}\left[\left(G_{yyy}E_y^2(\omega) - G_{yxx}E_x^2(\omega)\right)\sin(3\Omega) - 2G_{yxy}E_x(\omega)E_y(\omega)\cos(3\Omega)\right]$$

$$E_z(2\omega) = \left[\chi^{(2)}_{zzz} G_{zzz}E_z^2(\omega) + \chi^{(2)}_{zxx}\left(G_{zxx}E_x^2(\omega) + G_{zyy}E_y^2(\omega)\right)\right]$$

Table 4 : Summary of all nonzero $\chi^{(2)}_{surface}$ - components for the (100), (110) and (111) crystal face of GaAs and the corresponding experimental geometries that could allow their determination by SHG.

Face	χ^{s}_{ijk}	Input Polar.*	Output Polar.*	Sample Orient.*	
100	zzz	p	p	0o	b)
(isotrop)	zyy=zxx	s	p	0o	a)
	yyz=xxz	p	s	45	a)
110	zzz	p	p	0°	b)
(C_{1v})	zyy	s	p	0°	a)
	xxz=xzx	p	s	0°	c)
	yyz=yzy	p	s	36°	c)
	zxx	s	p	55o	c)
	yyy	s	s	0o	a)
	xxy=xyx	p	s	36o	c)
	yzz	p	s	36o	b)
	zzy=zyz	m	p	-	d)
	yxx	p	p	36o	c)
111	yyx=-xxx				
(C_{3v})	=xyy=yxy	m	s	-	d)
	yyz=xxz				
	=xzx=yzy	m	s	-	d)
	zzz	m	p	-	d)
	zxx=zyy	m	p	-	d)

* (p): p-polarized; (s): s-polarized; (m): mixed; (-): sample orientation Ω is determined by the input amd output polarizations.

---

a) : χ^{s}_{ijk} can be directly determined by the geometry given.

b) : χ^{s}_{ijk} is accessible in combination with other χ_{surf}- components, but it is much larger than the other components due to the Fresnel factors.

c) : χ^{s}_{ijk} is accessible only in combination with other χ_{surf}-components.

d) : χ^{s}_{ijk} is mixed with bulk contributions.

Figure Captions

Fig. 1: Coordinate system used in analysis. Description of the coordinate system is given in the text.

Fig. 2: SH-signal as a function of the time of evaporation of Sn on GaAs (100). The p_{in} - p_{out} geometry with the (100) axis in the plane of incidence was used.

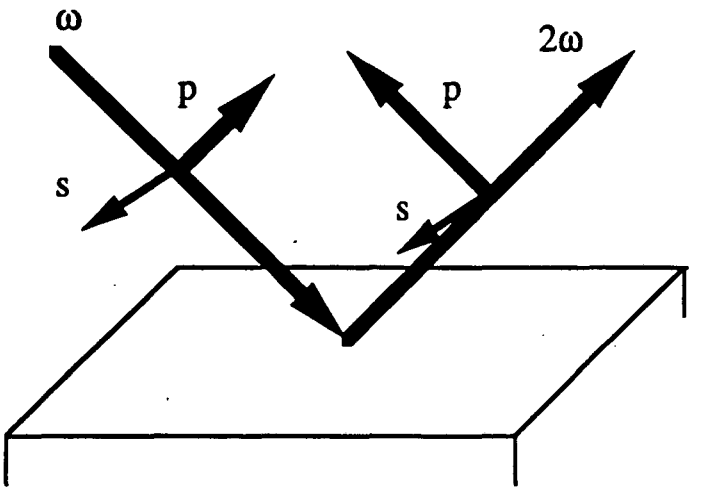

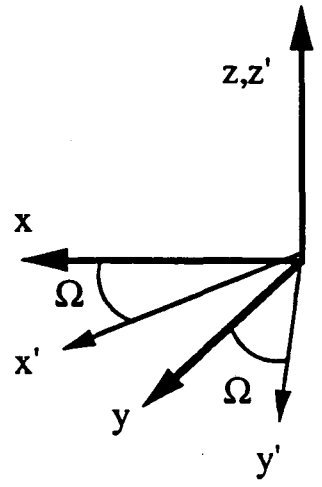

Figure 1

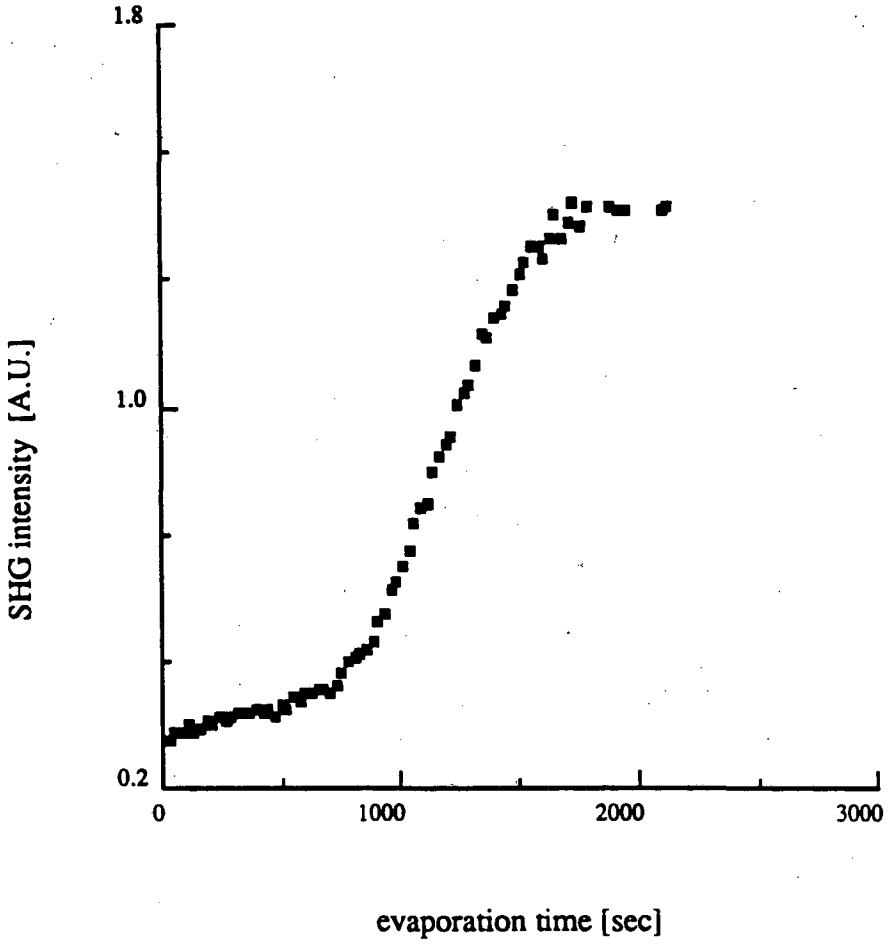
1.8
1.0
0.2
SHG intensity [A.U.]
0
1000
2000
3000
evaporation time [sec]

Fig 2

IV. Second Harmonic Generation from Anisotropic Monolayer Distribution and the Effect of Rubbing on Homogeneous Alignment of a Nematic Liquid Crystal

A. Introduction

Alignment of bulk liquid crystal (LC) mesophases by properly treated surfaces of substrates is a technique commonly used in the construction of LC devices. Several surface treatments have been successfully employed, but the physical mechanisms affecting the surface-induced bulk alignment are still not well understood. For homogeneous bulk alignment [1](average molecular orientation along a direction parallel to the surface), the specially treated surfaces often used are rubbed polymer-coated substrates, rubbed surfactant-coated substrates, and substrates covered with an obliquely evaporated SiO_x film. Obviously, as a surface-induced effect, how the first monolayer of LC molecules at the interface is oriented by the surface-molecule interaction is fundamental to our understanding of homogeneous alignment by different substrates.

Berreman[2, 3] first studied the problem by rubbing a glass substrate with diamond paste and creating microgrooves. He calculated the elastic distortion due to the grooves and found that the lowest energy configuration was for all the molecules to lie along the grooves, creating a uniformly aligned cell along the rubbing direction. Recently, Geary[4] *et. al.*, considering alignment of LC films on polymer-coated substrates rubbed with cloth, proposed a different mechanism. Rubbing of the films orients the polymer chains along a preferred direction and the molecular interaction between the LC molecules and the stretched polymer induces the alignment. Both proposed mechanisms lack direct experimental verification of the microscopic pictures they purport.

To study the LC alignment in different cases with different surface treatments, a variety of techniques have been employed. Pre-transitional optical birefringence[5, 6, 7] and contact angle measurements[8] have been used to deduce the order parameter of LC at various surfaces. Anchoring energy measurements[9] have been carried out to measure

the strength of the interaction between the treated surfaces and the LC bulk. All these techniques provide useful information more on the macroscopic properties of an interfacial system. They are not as helpful in probing the LC-substrate interaction at the microscopic level. Researchers have recently used scanning tunneling microscopes (STM) to observe the alignment of LC monolayers on conducting substrates, such as graphite[10], but the results still need interpretation and most of the systems with practical interest cannot be studied with this technique.

We have demonstrated in recent years that optical second harmonic generation (SHG) is a powerful method for probing molecules adsorbed at an interface. In particular, it can be used to determine the orientational distribution of a surface monolayer of molecules.[11, 12, 13] We have applied the technique to the study of LC monolayers at various interfaces. By monitoring the in-plane symmetry of an LC monolayer evaporated onto a substrate, we can determine whether the monolayer is anisotropically aligned by the treated surface.[6] This then allows us to conclude that the surface-induced alignment of the LC bulk is of a short-range or long-range nature. For some polymer-coated substrates, we have observed good alignment of the monolayer parallel to the rubbing direction, implying that a molecular epitaxy-like interaction is responsible for the bulk alignment. The monolayer alignment is only slightly altered in the presence of an LC bulk. For rubbed surfactant-treated substrates, no detectable anisotropy in the monolayer alignment can be observed, suggesting that the long-range elastic interaction may be responsible for the bulk alignment.

In this paper, we report the details of our SHG studies on the problem of surface-induced homogeneous alignment. A variety of rubbed polymer-coated substrates, rubbed surfactant-coated substrates, and obliquely evaporated SiO_x substrates have been investigated. Polarizing microscope and birefringence measurements were used to provide supplementary information about the substrates and the samples. In Sec. II, we describe the basic theory of how to derive the orientational distribution

function from the SHG measurements for a molecular monolayer. The necessary inclusion of some geometrical factors and possible contribution of the LC bulk to the SHG signal is discussed. The SHG results on LC monolayers evaporated onto rubbed and unrubbed substrates coated with several different polymers and surfactants, as well as obliquely evaporated SiO_x are then presented and analyzed in Sec. IV. Finally, in Sec. V, the alignment mechanisms for different surface treatments are discussed. It is shown that the microscopic picture of the alignment derived from our work is consistent with the results of surface anchoring energy measurements.

B. General SHG Considerations

1. Using SHG to derive orientational distribution function for a molecular monolayer.

Optical second harmonic generation as a general surface analytical tool has been described in detail in the previous Chapters. As a second-order nonlinear optical process, it is highly surface specific and allows probing of polar ordering at an interface. With its submonolayer sensitivity, the technique is ideal for studying molecular monolayers at various interfaces. The monolayer characteristics are reflected in the surface nonlinear susceptibility of the monolayer. By measuring the individual components of the nonlinear susceptibility, it is possible to deduce information about the orientation and arrangement of molecules in a monolayer. We are particularly interested in the orientation and alignment of an LC monolayer adsorbed on a solid substrate.

Consider a monolayer of molecules with a second-order polarizability $\alpha^{(2)}$. Assuming that the intermolecular interaction is negligible, as is often the case in the optical response[14], we can relate the nonlinear susceptibility $\chi^{(2)}$ to the molecular nonlinear polarizability $\alpha^{(2)}$ by:

$$\chi^{(2)}_{ijk} = N_S \langle G^{\lambda\mu\upsilon}_{ijk} \rangle \alpha^{(2)}_{\lambda\mu\upsilon} \tag{1}$$

where N_S is the surface density of molecules, $G^{\lambda\mu\upsilon}_{ijk}$ is a transformation matrix connecting the molecular coordinates (ξ,η,ζ) with the substrate coordinates (x,y,z) (see Fig. 1), and the angular brackets denote an average over the molecular orientational distribution. For molecules with a dominant hyperpolarizability element $\alpha^{(2)}_{\xi\xi\xi}$ along the long molecular axis ξ, we can write χ in the simple form:

$$\chi^{(2)}_{ijk} = N_S \langle (\hat{i}\cdot\hat{\xi})(\hat{j}\cdot\hat{\xi})(\hat{k}\cdot\hat{\xi}) \rangle \alpha^{(2)}_{\xi\xi\xi} \tag{2}$$

This is the case for many LC molecules, such as 4-n-octyl-4-cyanobiphenyl (8CB) we used in our experiment. Note that Eq. (2) leads to the permutation symmetry

$$\chi^{(2)}_{ijk} = \chi^{(2)}_{jik} = \chi^{(2)}_{kij} = \ldots. \tag{3}$$

which is necessarily satisfied if $\alpha^{(2)}_{\xi\xi\xi}$ is the only dominant element of $\alpha^{(2)}$. Also note that $\chi^{(2)}_{ijk}$ vanishes if the molecules do not form a net polar-oriented layer.

For an isotropic distribution of molecules in the monolayer, there are only two independent nonvanishing components of $\chi^{(2)}$. With a dominating $\alpha^{(2)}_{\xi\xi\xi}$, they are related to the molecular orientation as follows:

$$\begin{aligned} \chi_{zzz} &= N_S \langle \cos^3\theta \rangle \alpha^{(2)}_{\xi\xi\xi} \\ \chi_{zii} &= \chi_{izi} = \chi_{iiz} = \tfrac{1}{2} N_S \langle \sin^2\theta\cos\theta \rangle \alpha^{(2)}_{\xi\xi\xi} \end{aligned} \tag{4}$$

where i, j = x,y and θ is the (polar) angle between $\hat{\xi}$ and $\hat{z}$. If the molecules have a preferred alignment along $\hat{x}$ in the surface plane, then the resulting C_{1v} symmetry allows six independent, nonvanishing components of χ :

$$\chi^{(2)}_{zzz} = N_s < \cos^3\theta > \alpha^{(2)}_{\xi\xi\xi}$$

$$\chi^{(2)}_{xxx} = -N_s < \sin^3\theta > < \cos^3\phi > \alpha^{(2)}_{\xi\xi\xi}$$

$$\chi^{(2)}_{zyy} = \chi^{(2)}_{yzy} = \chi^{(2)}_{yyz} = N_s < \cos\theta - \cos^3\theta > < 1 - \cos^2\phi > \alpha^{(2)}_{\xi\xi\xi}$$

$$\chi^{(2)}_{zxx} = \chi^{(2)}_{xzx} = \chi^{(2)}_{xxz} = N_s < \cos\theta - \cos^3\theta > < \cos^2\phi > \alpha^{(2)}_{\xi\xi\xi}$$

$$\chi^{(2)}_{zxz} = \chi^{(2)}_{zzx} = \chi^{(2)}_{xzz} = -N_s < \sin\theta - \sin^3\theta > < \cos\phi > \alpha^{(2)}_{\xi\xi\xi}$$

$$\chi^{(2)}_{xyy} = \chi^{(2)}_{yxy} = \chi^{(2)}_{yyx} = -N_s < \sin^3\theta > < \cos\phi - \cos^3\phi > \alpha^{(2)}_{\xi\xi\xi} \qquad (5)$$

where ϕ is the azimuthal angle defined in Fig. 1. Note, that we have assumed independent distributions for θ and ϕ.

The above nonvanishing elements of $\chi^{(2)}$ can be measured by surface SHG as described by Eq. 1 - 7 in Chapter 2. As we showed in Chapter 3, the measured SH field depends on the sample geometry with respect to the beams and on the input/output beam polarizations. In this case, we measure the SHG as a function of sample orientation to measure as the individual components of $\chi^{(2)}$. Let Φ be the angle between the plane of incidence and the direction of the preferred molecular alignment , i.e., the $\hat{x}$-axis (see Inset in Fig. 1). We then have, for the s-in/s-out polarization combination

$$\chi^{(2)}_{eff} = \chi^{(2)}_{xxx} \sin^3\Phi L_y(2\omega)L_y^2(\omega) + 3\chi^{(2)}_{xyy} \cos^2\Phi \sin\Phi\, L_y(2\omega)L_y^2(\omega).$$

For p-in/s-out,

$$\chi^{(2)}_{eff} = \chi^{(2)}_{xxx} \cos^2\Phi \sin\Phi\, L_y(2\omega)L_x^2(\omega) \cos^2\theta_1(\omega)$$

$$+ \chi^{(2)}_{xyy} (3\sin^3\Phi - 2\sin\Phi)L_y(2\omega)L_x^2(\omega)\cos^2\theta_1(\omega)$$

$$+ (\chi^{(2)}_{xxz} - \chi^{(2)}_{yyz}) \sin2\Phi\, L_y(2\omega)L_x(\omega)L_z(\omega)[-\sin\theta_1(\omega)\cos\theta_1(\omega)]$$

$$+ \chi^{(2)}_{xzz} \sin\Phi\, L_y(2\omega)L_z^2(\omega) \sin^2\theta_1(\omega).$$

For s-in/p-out,

$$\chi^{(2)}_{eff} = \chi^{(2)}_{xyy} (3\cos^3\Phi - 2\cos\Phi)L_x(2\omega)L_y^2(\omega)\cos\theta_1(2\omega)$$

$$+ \chi^{(2)}_{xxx} \sin^2\Phi \cos\Phi\, L_x(2\omega)L_y^2(\omega)\cos\theta_1(2\omega)$$

$$+ \chi^{(2)}_{zxx} \sin^2\Phi\, L_z(2\omega)L_y^2(\omega)\sin\theta_1(2\omega)$$

$$+ \chi^{(2)}_{zyy} \cos^2\Phi\, L_z(2\omega)L_y^2(\omega)\sin\theta_1(2\omega).$$

For p-in/p-out

$$\chi^{(2)}_{eff} = \chi^{(2)}_{xxx} \cos^3\Phi\, L_x(2\omega)L_x^2(\omega)\cos\theta_1(2\omega)\cos^2\theta_1(\omega)$$

$$+ 3\chi^{(2)}_{xyy} \sin^2\Phi\cos\Phi\, L_x(2\omega)L_x^2(\omega)\cos\theta_1(2\omega)\cos^2\theta_1(\omega)$$

$$+ \chi_{xxz} \cos^2\Phi\{2L_x(2\omega)L_x(\omega)L_z(\omega)[-\cos\theta_1(2\omega)\cos\theta_1(\omega)\sin\theta_1(\omega)]$$

$$+ L_z(2\omega)L_x^2(\omega)\sin\theta_1(2\omega)\cos^2\theta_1(\omega)\}$$

$$+ \chi_{yyz} \sin^2\Phi\{2L_x(2\omega)L_x(\omega)L_z(\omega)[-\cos\theta_1(2\omega)\cos\theta_1(\omega)\sin\theta_1(\omega)]$$

$$+ L_z(2\omega)L_x^2(\omega)\sin\theta_1(2\omega)\cos^2\theta_1(\omega)\}$$

$$+\chi^{(2)}_{xzz} \cos\Phi\{L_x(2\omega)L_z^2(\omega)\cos\theta_1(2\omega)\sin^2\theta_1(\omega) +$$

$$2L_z(2\omega)L_x(\omega)L_z(\omega)[-\sin\theta_1(2\omega)\sin\theta_1(\omega)\cos\theta_1(\omega)]\}$$

$$+ \chi^{(2)}_{zzz}\left[L_z(2\omega)L_z^2(\omega)\sin\theta_1(2\omega)\sin^2\theta_1(\omega)\right]. \qquad (7)$$

In the case where medium 1 is air and medium 2 is glass with little nonlinearity, the contribution from the bulk is negligible.

We can measure SHG as a function of Φ for the four different polarization combinations and, by fitting the data with Eq. (7), we can deduce all the nonvanishing elements of $\chi^{(2)}_{ijk}$. We can then determine, from Eq. (5), $\alpha^{(2)}_{\xi\xi\xi}$ plus 5 parameters related to molecular orientation. Equation (5) yields,

$$\frac{\langle \sin^3\theta \rangle}{\langle \sin\theta \rangle} = \frac{\chi_{xxx} + \chi_{yyx}}{\chi_{xxx} + \chi_{yyx} + \chi_{xzz}}$$

$$\frac{\langle \cos^3\theta \rangle}{\langle \cos\theta \rangle} = \frac{\chi_{zzz}}{\chi_{zzz} + \chi_{zxx} + \chi_{zyy}}. \qquad (8)$$

By assuming a Gaussian distribution in θ,

$$f(\theta) = F \exp\left[- \frac{(\theta - \theta_0)^2}{2\sigma^2} \right], \qquad (9)$$

where F is a normalization constant, Eq. (8) can be used to determine the average angle θ_0 and the variance σ. For the unrubbed surface, we have $\langle \sin\theta \rangle = \langle \sin^3\theta \rangle = 0$, and

$$\frac{\langle \cos^3\theta \rangle}{\langle \cos\theta \rangle} = \frac{1}{1 + \frac{2\chi_{zyy}}{\chi_{zzz}}}. \qquad (10)$$

The distribution in ϕ can be assumed to be a truncated power series,

$$g(\phi) = \sum_{n=0}^{3} d_n \cos(n\phi). \qquad (11)$$

The coefficients d_n can then be calculated from the measured $\chi^{(2)}_{ijk}$ using Eq. (5) and knowing $f(\theta)$. The d_2 coefficient describes the surface anisotropy between x and y and is obtained from $\chi_{zxx}/(\chi_{zxx} + \chi_{zyy})$; it is independent of $f(\theta)$. The d_1 and d_3 coefficients describe the asymmetry between x and -x. They are deduced from χ_{zzx} and $(\chi_{xxx} - 3\chi_{yyx})$, respectively.

2. Nematic Liquid Crystal Bulk Contribution

In our experiment, we are also interested in the orientational distribution of an LC monolayer on a substrate in the presence of the bulk. For this case, medium 1 is the glass substrate and medium 2 is the LC bulk. The bulk contribution to the SHG is no longer zero.[15] In order to be able to deduce $\chi^{(2)}$ for the LC monolayer at the interface from the measurements via Eq. (5), we need to know $\chi^{(2)}_{bulk}$ separately. For LC, $\chi^{(2)}_{bulk}$ can be measured independently.[15] The bulk contribution comes mainly from the discontinuity across the interface of the electric quadrupole part resulting from anti-parallel pairing of molecules. The total susceptibility used in Eq. 7 is given by (see Eq. , Chapter 2)[15]

$$\chi^{(2)}_{zzz} = \chi^{surface}_{zzz} - \frac{\chi^{Q}_{zzzz}}{\varepsilon(2\omega)\varepsilon^2(\omega)}$$

$$\chi^{(2)}_{zxx} = \chi^{surface}_{zxx} - \frac{\chi^{Q}_{zzxx}}{\varepsilon(2\omega)}$$

$$\chi^{(2)}_{zyy} = \chi^{surface}_{zyy} - \frac{\chi^{Q}_{zzyy}}{\varepsilon(2\omega)}$$

with

$$\chi^{Q}_{ijkl} = \tfrac{1}{2} N_B < H^{\xi\xi\xi\xi}_{ijkl} > \alpha^{(2)}_{\xi\xi\xi} \xi_o \qquad (12)$$

where N_B is the bulk density of LC molecules, ξ_o is the separation between the chromophores of the anti-parallel molecules along $\hat{\xi}$ and H is the transformation matrix. The intrinsic quadrupole contribution from individual LC molecules is usually small in

comparison and can be neglected. Equation (16) shows that χ^{Q}_{ijkl} depends on the molecular orientation through $< H^{\xi\xi\xi\xi}_{ijkl} >$ and is therefore a function of the bulk orientational order. We consider here a bulk homogeneous alignment along $\hat{x}$. From Eq. (16), the nonvanishing χ^{Q}_{ijkl} elements for the LC bulk are

$$\chi^{Q}_{zzzz} = \tfrac{1}{2}\, N_B < \tfrac{3}{8}\sin^4\Theta > \alpha^{(2)}_{\xi\xi\xi} \xi_0 = \tfrac{1}{10} N_B \alpha^{(2)}_{\xi\xi\xi} \xi_0 \left[1 - \tfrac{10}{7} <P_2> + \tfrac{3}{7} <P_4> \right]$$

$$\chi^{Q}_{zzxx} = \tfrac{1}{2}\, N_B < \tfrac{1}{2}\sin^2\Theta \cos^2\Theta > \alpha^{(2)}_{\xi\xi\xi} \xi_0 = \tfrac{1}{30} N_B \alpha^{(2)}_{\xi\xi\xi} \xi_0 \left[1 + \tfrac{5}{7} <P_2> - \tfrac{12}{7} <P_4> \right]$$

$$\chi^{Q}_{zzyy} = \tfrac{1}{2}\, N_B < \tfrac{1}{8}\sin^4\Theta > \alpha^{(2)}_{\xi\xi\xi} \xi_0 = \tfrac{1}{30} N_B \alpha^{(2)}_{\xi\xi\xi} \xi_0 \left[1 - \tfrac{10}{7} <P_2> + \tfrac{3}{7} <P_4> \right] \quad (13)$$

where Θ is the angle between $\hat{\xi}$ and $\hat{x}$ (the rubbing direction), $P_2 = \frac{1}{2}(3\cos^2\Theta - 1)$ and $P_4 = \frac{1}{8}(35\cos^4\Theta - 30\cos^2\Theta + 3)$ are the second and fourth Legendre polynomials, respectively. Both $<P_2>$ and $<P_4>$ are finite and temperature dependent in the mesophase, jump to zero in the transition to the isotropic phase and remain zero there. For 8CB, the values of χ^{Q}_{ijkl} have already been measured.[15]

With the presence of the LC bulk contribution, $\chi^{(2)}_{eff}$ of Eq. (7) should also experience a jump at the mesomorphic-isotropic transition. The sign of the jump depends on the sign of the bulk contribution, relative to the interfacial contribution from the LC monolayer. In forming quadrupole pairs in the bulk, the LC molecules always have their polar head groups facing each other as pictured in Fig. 2. The surface and bulk contributions should have opposite signs if the surface monolayer is polar oriented with the head groups adsorbed to the substrate. There will also be a change in the local field factors resulting from the change in the index of refraction of the LC material that occurs at the transition (see Appendix A). This will also affect the value of $\chi^{(2)}_{eff}$ across the transition.

In the analysis of our SHG data, the local field factors $L(\Omega)$ in Eq. (7) are important. For spin-coated polymer films on glass substrates, multiple reflections in the polymer films also contribute to the local field factors. The functional form for the local field factors for the polymer-coated substrates are presented in Appendix A.

C. Experimental Arrangement

The experimental setup for measurements of SHG in reflection has been described elsewhere.[12] We used a frequency-doubled, CW Q-switched, mode-locked YAG laser (Quantronix 416) as the pump. The beam was incident on a sample mounted on a rotating stage. The SH output was detected by a photomultiplier and a gated integrator.

We used the liquid crystal 8CB in our experiment. It exhibits smectic-A, nematic and isotropic phases with transition temperatures $T_{AN} = 33.5\ ^{\circ}C$ and $T_{NI} = 40.5\ ^{\circ}C$ Adsorbed 8CB monolayers on substrates were prepared by evaporation, using SHG as an *in situ* probe of the deposition.[16] In all cases, the signal increased quadratically with time and then abruptly saturated, indicating that the molecules adsorbed uniformly onto the substrate until a full monolayer was formed. Evaporation of 8CB onto all the substrates under investigation exhibited similar temporal behavior.

Polymer films were prepared by spin-coating polymer solutions onto fused silica substrates, then baked to eliminate the solvent. The polymers we used are pictured in Fig. 3. The surfactant-coated substrates were prepared through deposition of silane onto the substrates from solution and then polymerized by heating. Methylaminopropyltrimethoxysilane (MAP) was the silane we studied. None of these coated substrates generated a significant SHG signal before deposition of 8CB. The SiO_x-coated substrates were prepared by obliquely evaporating a 200-Å thick film SiO_x at an angle of 60 degrees with respect to the surface normal.

Rubbing of the substrates was used to induce molecular alignment along the rubbing direction. The rubbing process was carried out by translating a substrate at a constant speed while it is in contact with a rotating wheel of velvet. The rubbing strength can be characterized by the parameter R_S, defined as[17]

$$R_S = \gamma \mathscr{L}$$

where $\mathscr{L}$ is the total length of cloth in contact with a given point on the substrate and γ is a characteristic coefficient of the interface between the rubbing cloth and the substrate. Generally, γ is a complicated function of the frictional coefficient, the density and length of cloth fibers, the rubbing pressure, etc. For our rubbing geometry, we can write $\mathscr{L}$ as

$$\mathscr{L} = N\ell \left| 1 \pm \frac{\Omega r}{v} \right|$$

where N is the number of translations under the wheel, ℓ is the length of cloth in contact with the substrate in one translation, Ω is the angular speed of the rotating wheel, v is the translational velocity of the substrate and r is the radius of the rubbing wheel. The sign is + when the directions of motion of the rotating wheel and the substrate are opposite at their point of contact. For our geometry, the sign is negative (see Inset of Fig. 1). For our rubbing machine, ℓ = 5 mm, $\Omega/2\pi$ = 68 rpm, r = 2.5 cm, and v varied from .12 to .6 cm/sec. We varied the rubbing strength both by changing the pressure on the polymer-coated substrate, and by changing N or v. Since γ is not a well-defined quantity, we cannot have absolute values for the rubbing strengths, but we can change the relative rubbing strengths by varying $\mathscr{L}$.

The LC cells were prepared by first sandwiching a 130 micron thick mylar spacer between two substrates and then filling it by capillary action with 8CB in the isotropic phase. The rubbed substrates induced a homogeneous bulk alignment which was monitored with a polarizing microscope. The anisotropy in the polymer films created by rubbing could be measured by a birefringence measurement using a standard ellipsometry set-up.[12]

D. Experimental Results

1. On polyimide-coated substrates

We monitored the SHG signal from a monolayer of 8CB on rubbed and unrubbed polyimide-coated substrates as a function of the azimuthal orientation of the sample, Φ.[6] An example of the results is presented in Fig. 4. As expected, the signal from the unrubbed substrates is isotropic in Φ. SHG with s-in/s-out and p-in/s-out geometries is forbidden by symmetry on an isotropic surface, and therefore generated no detectable signal. On the hard rubbed substrates, however, the signal dependence on Φ is strongly anisotropic and the s-in/s-out and p-in/s-out signals are nonzero. The nonzero signal from the s-in/s-out geometry is evidence that the monolayer orientation is azimuthally anisotropic with at most one mirror plane. We repeated these measurements on polyimide-coated substrates rubbed with a variety of rubbing strengths.

The individual nonvanishing components of the nonlinear susceptibility $\chi^{(2)}$ for the 8CB monolayer in Eq. (5) can be determined from the data in Fig. 4. Specifically, we could obtain $\chi^{(2)}_{xxx}$ from the result at s-in/s-out and $\chi^{(2)}_{zxx}$ at s-in/p-out with the sample oriented such that s is parallel to the rubbing direction $\hat{x}$ (Φ=90°). Then, $\chi^{(2)}_{xyy}$, $\chi^{(2)}_{zyy}$, $\chi^{(2)}_{zzz}$, and $\chi^{(2)}_{zxz}$ could all be determined from data points at special geometries according to Eq. (7). Finally, the data from the full angular scan in Fig. 4 could be fit using Eq.

(7) to reduce the uncertainty of the values of $\chi^{(2)}_{ijk}$. Our fit of Fig.4 resulted in a very small standard deviation (less than 1.5×10^{-15} esu). As mentioned in Sec. II, we can use the values obtained for $\chi^{(2)}_{ijk}$ to find approximate distribution functions in θ and ϕ. The results are listed in Table 1 as the hard rubbing case. The azimuthal distribution function is plotted in Fig. 5.

Measurements of LC monolayers on polyimide-coated substrates rubbed with different rubbing strengths were also carried out and analyzed. The results are summarized in Table 1. Sample 1 was unrubbed. Samples 2-5 were rubbed under the same pressure (i.e. identical γs). Samples 2-4 were passed under the rubbing wheel 1, 3 and 5 times, respectively, at a constant velocity of .6 cm/sec with the wheel not rotating. Sample 5 was passed under the wheel with the same conditions, except that the wheel was rotating with an angular velocity of 68 rpm. Sample 6 was rubbed at a considerably harder pressure. In all cases, we found that θ_0 [76° and σ = 5-7°. While the determination of σ is less certain (% in standard deviation), the value of θ_0 is accurate to within 2%. For the unrubbed sample, we assume a $\sigma = 5^o$ to determine $\theta_0 = 76^\circ$. If we assume a δ-function distribution in θ instead of the Gaussian distribution, we find $\theta_0 = 74°$. The results imply that rubbing of the polymer does not affect the polar orientation of the 8CB molecules.

Fig. 5 presents plots of the azimuthal orientational distributions of the LC monolayers on the differently rubbed substrates. They show explicitly that rubbing causes the molecule to lie preferentially parallel and antiparallel to the rubbing direction, more antiparallel than parallel (i.e., the chromophores of 8CB molecules tilt more in the direction of the rubbing strokes). The stronger the rubbing strength, the greater is the anisotropy in the monolayer distribution. We also measured the phase of the polar monolayer, and found that the head groups pointed toward the substrate for both rubbed and unrubbed polyimide-coated substrates. All the substrates listed in Table 1, except

the unrubbed one, were effective in inducing a bulk LC homogeneous alignment in a cell along the rubbing direction.

To see how rubbing affects the polymer films, we measured the birefringence induced in the films by the rubbing with a standard ellipsometry set-up.[12] These measurements were limited in their sensitivity by a large background anisotropy in our substrates. We could measure an induced birefringence of $\Delta\phi = .5$ mrad. Note that the induced birefringence is not a well-defined physical quantity since we do not know over what distance into the bulk of the polymer film the birefringence is distributed, though it has been estimated to be 10-20 nm.[18] However, we used these measurements to qualitatively show that rubbing did reorient the polymer chains and the degree of reorientation increased with the rubbing strength. In our measurements, $R_S = 1\gamma$ corresponds to the minimum detectable rubbing-induced birefringence. The LC cells prepared with substrates more lightly rubbed exhibited rather poor homogeneous alignment with stripes of aligned domains. The LC monolayers on such substrates showed no discernible anisotropy in the monolayers. Detailed studies on rubbing-induced birefringence on several polymers have been reported by Geary *et. al.* in Ref. 3.

We also carried out SHG measurements on an LC cell made of rubbed polyimide-coated substrates and studied the orientation distribution of the polar-oriented LC monolayer at the LC/substrate interface with the bulk in the isotropic and nematic (ordered) phases. As discussed in Sec. II, we can deduce the values of the surface susceptibility components from the total signal by subtracting out the bulk contribution. The measured SHG as a function of Φ for the four input/output polarization combinations is shown in Fig. 6. In the theoretical fit also shown in Fig. 6, we used Eq. (7) and the results for $\chi^{(2)}_{bulk}$ from Reference 12 and obtained $\chi^{(2)}_{ijk}$ for the interfacial LC monolayer from the fit. There exists some uncertainty (< 10%) in the values of $\chi^{(2)}_{ijk}$, mainly due to a 10% uncertainty in the index of refraction of LC at the

second harmonic frequency (see Table 3). This corresponds to less than a 10% uncertainty in the fitting parameters. The value of χ_{xxz} is less certain ($\leq 20\%$) because it is much smaller. Using the same functional forms for the distributions in θ and ϕ, namely $f(\theta)$ and $g(\phi)$ respectively, given in Sec. II, we found the following results. For $f(\theta)$, we calculated $\theta_0 = 71$ degrees with a width of $\sigma = 5$. The value of σ is only known within a factor of 2, but θ_0 is known within 2%. The azimuthal distribution function is given by

$$g(\phi) = 1 + .06\cos\phi + .43\cos2\phi \quad -.001\cos3\phi$$

which is plotted in Fig. 7 along with the distribution for an 8CB monolayer without the presence of the bulk. The average angles and the distribution function in ϕ for the monolayer in the isotropic cell and for the monolayer in air are very clear, indicating that the bulk has little effect on the surface ordering. Little change in the ordering of the monolayer was observed even when we raised the temperature of the bulk 25 degrees above the nematic-isotropic transition, also pointing to the fact that the short-range interaction between the rubbed polymer and the LC molecules is very strong.

We then cooled the LC cell to the nematic phase and repeated the SHG measurements to see if the ordering of the bulk could affect the orientational distribution of the first monolayer. The only experimental geometry that showed significant temperature dependence was the p-in/p-out geometry which is what we expect since the χ^Q_{zzxx} component should have the largest jump across the isotropic/nematic transition according to Eq. (13). For the other experimental geometries, the change of the ordering of the bulk had little effect on the SHG signal, implying that the overall contribution from the bulk is small. The temperature dependence of SHG in the p-in/p-out geometry is well characterized by taking into account the quadrupole contribution to SHG from the bulk orientational order and the change in the index of refraction of the

LC bulk as it goes from the isotropic to the nematic phase. The sign of the jump was correct for the bulk contribution being out of phase with the surface dipole contribution. Thus, our results are consistent with the model that the orientation distribution of the first monolayer hardly changes as the bulk goes from the isotropic to the nematic phase.

2. Different Polymers

To better understand the nature of the rubbed polymer - LC interaction, we have looked at LC monolayers on a number of different polymers. The characteristics of the polymers used and the experimental results are summarized in Table 2. Polyvinyl alcohol (PVA) produced results most similiar to the polyimide. A small , but detectable, rubbing-induced birefringence in the PVA film could be measured. LC cells made with PVA-coated substrates had good alignment parallel to the rubbing direction. The LC monolayer alignment on unrubbed and rubbed PVA-coated substrates showed roughly the same orientational distribution as on polyimide. In contrast, polystyrene (PS) has been reported to have a large negative rubbing-induced birefringence, which has been interpretted as a strong ordering of the polymer sidegroups perpendicular to the rubbing direction.[4,19] We tried substrates coated with atactic polystyrene, where the sidegroups are randomly oriented about the chain, and found no alignment although the birefringence measurements indicate substantial chain reorientation. With isotactic polystyrene, that has 99% of the sidegroups on one side of the backbone, however, we found good cell alignment perpendicular to the rubbing direction. For both forms of PS, we were not able to see any significant second harmonic signal from a monolayer evaporated onto the substrate. This is due to the fact there are no polar sites to which the 8CB headgroups could attach to form a polar layer. Polyvinylbenzylchloride (PVBC) is similiar to atactic PS, but has methylchloride groups that can act as polar sites. The rubbed PVBC substrates had a very large negative birefringence, yet they led to weak bulk alignment parallel to the rubbing direction, as evidenced by Schlieren

defects[20] on a weakly aligned background. The SHG signal from an LC monolayer on a rubbed PVBC-coated substrate was weakly anisotropic, with molecules preferentially aligned along the rubbing direction. In summary, for all these polymers, we found that rubbing leads to a definite reorientation of the polymers and when detectable by SHG, the induced LC monolayer alignment was along the same direction as the bulk alignment.

3. Nonpolymer Samples

We have conducted similar SHG measurements on 8CB monolayers evaporated onto MAP-coated substrates.[21] For both rubbed and unrubbed substrates, the SHG signal showed an isotropic dependence on sample orientation rotation about the surface normal for the s-in/p-out and p-in/p-out geometries, and vanished for the p-in/s-out and s-in/s-out geometries, indicating there is no detectable anisotropy in the distribution of the 8CB monolayer. The results indicate that the LC molecules in the monolayer are not aligned in the surface plane in all cases. From the measured values of $\chi^{(2)}_{zzz}$ and $\chi^{(2)}_{zxx} = \chi^{(2)}_{xzx}$, we found an average polar angle of $\theta_0 = 70$ degrees for the 8CB molecules on both rubbed and unrubbed sample substrates assuming a δ-function distribution for θ. We repeated the measurements on a cell made of rubbed-MAP coated substrates.[6] The cell showed good homogeneous alignment along the rubbing direction, as observed under a polarizing microscope. When the cell was in the isotropic phase, the SHG signal was isotropic with respect to the sample orientation about the surface normal, implying that both the bulk and the surface layer are isotropic in the azimuthal plane. When the LC cell was cooled to the nematic phase, we began to see the onset of an anisotropic distribution. The difference from the signal in the isotropic phase is most pronounced in the p-in/p-out geometry, as it was in the polyimide cell. These results are consistent with the signal expected from an isotropic polar-ordered LC monolayer and a homogeneously aligned LC bulk as described in Eq. (7). The contrast with the polymer

treated substrate is clear -- the MAP coating on a substrate has no effect on the LC monolayer alignment in the azimuthal plane, indicating that the surface-LC interaction responsible for the bulk LC alignment must be macroscopic in nature.

We also studied at the molecular distribution of 8CB monolayers on SiO_x substrates. Oblique evaporation of SiO_x leads to saw-tooth-like structures forming grooves on the surface.[22] It was thought that LC molecules might lie along the grooves to yield a homogeneously aligned cell. However, since the grooves are much larger than the molecular dimension of an LC molecule, we would not expect a monolayer adsorbed at the surface to be aligned. To determine the orientational distribution of a monolayer on such substrates, we did the following experiments. First, it was determined that an 8CB cell constructed with these substrates exhibited very good bulk homogeneous alignment. Second, we measured SHG from a clean obliquely evaporated SiO_x substrate as a function of the sample rotation, and observed an anisotropic dependence. This is shown in Fig. 7a. The observed anisotropy is a geometrical effect. The grooved surface causes the local input and output polarizations as well as the local angle of incidence to vary with the sample rotation about the surface normal. They can be taken into account in the calculation of the geometrical local field factors. In Appendix B, we present a model for the saw-tooth structure and calculate SHG from the surface. The observed anisotropy can be qualitatively reproduced (see Fig. 7c). Third, we heated the sample to 250°C in air, oxidizing SiO_x into SiO_2, which showed negligible SHG contribution. We then deposited an 8CB monolayer onto the SiO_2 grooved substrate by either evaporation or spreading with a solvent. The SHG signal from the sample now appeared to have an azimuthal anisotropy similar to that observed on the clean SiO_x substrate (see Fig. 7b). Note that the anisotropy observed here is markedly different from the one expected for a monolayer preferentially aligned along the direction of the grooves (see Fig. 2). For the former, the anisotropic distribution has a mirror plane perpendicular to the grooving direction, but for the latter, the mirror

plane is parallel to the grooves. This indicates that the observed anisotropy is still a geometrical effect. By analyzing our data as from a locally isotropic monolayer on a saw-tooth surface, we were able to account for the observed anisotropy in the SHG signal. Thus, the LC bulk alignment mechanism in this case must come from the long-range surface-LC interaction affected by the grooves.

The anisotropy in the surface geometry limits our ability to quantitatively measure anisotropy in the orientational distribution of an LC monolayer on the grooved surface. This is particularly true for the evaporated SiO_x surfaces as they are poorly defined in reality.

E. Discussion

Two models are commonly used to describe surface-induced homogeneous alignment of LC cells. The groove model,[2, 3] applicable to obliquely evaporated SiO_x substrates, proposes that with the LC molecules aligned along the groove direction, the bulk elastic energy from the long-range interaction is minimized. The molecular epitaxy-like model applies to rubbed polymer surfaces.[4] It suggests that rubbing reorients the polymer chains at the surface, similar to cold drawing of bulk polymer samples. The adsorbed LC monolayer is then preferentially aligned by interacting directly with the oriented polymer surface and this alignment is extended into the bulk, analogous to epitaxial growth. To date, the physics of surface-induced alignment in liquid crystals has been mostly studied through studies of the surface anchoring energy,[9] which is a macroscopic interfacial parameter that describes the interaction of an LC bulk with a surface. For $|\theta - \theta_0| << 1$, the interfacial free energy is usually written in the form[23]

$$U_{interfacial} = \frac{1}{2} A(\theta - \theta_0)^2$$

where θ is the angle of the director at the interface, θ_0 is the preferred direction, and A is the anchoring strength, or the anchoring energy. However, the microscopic picture of this surface anchoring is not very clear. Here, we try to relate our SHG measurements, which are at the microscopic level, to the surface anchoring energy measurements.[9]

Generally, two surface anchoring energies are used to describe homogeneously aligned LC films. Polar anchoring refers to resistence to distortion of the director from an easy axis in the polar angle, and azimuthal anchoring to distortion in the azimuthal angle. The two anchoring energies have been measured for rubbed surfactant-coated substrates,[24,25,26] obliquely evaporated SiO_x substrates,[27, 28,29] and rubbed polymer-coated substrates.[9,30] For rubbed MAP-substrates, the measured azimuthal anchoring energy is 5×10^{-3} erg/cm^2, and the measured values for the polar anchoring energy range from 5×10^{-3} erg/cm^2 to 5×10^{-2} erg/cm^2. The azimuthal anchoring energy for SiO_x substrates is on the order of 1×10^{-3} erg/cm^2 while the polar anchoring energy is of 1×10^{-2} erg/cm^2. In these cases, the anchoring energies are sensitive functions of temperature near the isotropic-nematic phase transition. Both the polar and azimuthal anchoring energies have been measured for rubbed polyimide as a function of rubbing strength. The polar anchoring energy is 1 erg/cm^2 and is independent of the rubbing strength. The azimuthal anchoring energy is 5-14 $\times 10^{-3}$ erg/cm^2, and is strongly dependent on rubbing strength. The polar anchoring energy of rubbed PVA is 1.5 erg/cm^2, and has little temperature dependence. The temperature dependence of the azimuthal anchoring energy for polymer-coated substrates has not yet been measured. We notice that the anchoring energies associated with the rubbed polymers are two to three orders of magnitude larger than the other surface treatments for the polar case, and up to one order of magnitude larger for the azimuthal case. This implies that the alignment force based on the short-range interaction between the rubbed polymers and the first layer of LC is significantly stronger than the one based on minimization of the elastic energy of the bulk.

Our SHG results, which can provide microscopic pictures for the two different alignment mechanisms, are consistent with these anchoring energy results. For the rubbed polymers, our experiments clearly demonstrate the existence of a strong molecular interaction between the rubbed polymers and the first layer of LC molecules. The birefringence measurements imply that the rubbing process leads to a reorientation of polymer chains on the surfaces of all the polymers we have studied.[4] The SHG results show that the stronger rubbing strengths yield better alignment of the monolayer, directly relating the polymer chain reorientation to the LC monolayer alignment. This is a clear indication that a short-range molecular interaction exists between the reoriented polymer and the liquid crystal molecules. This interaction is quite strong as evidenced by the preservation of the monolayer alignment in the presence of an isotropic bulk heated well above the transition temperature. The homogeneous bulk alignment is obviously an extension of the surface alignment via the molecular epitaxy-like interaction. The alignment of the LC bulk perpendicular to the rubbing direction for the isotactic PS-coated substrates provides further evidence to this mechanism. Crystalline polymers seem necessary for the LC alignment, further supporting the epitaxial picture. Crystallinity here means regular arrangement of the polymer chains including the side groups. Isotactic PS has a high degree of crystallinity, whereas atactic PS are not. Both atactic and isotactic PS showed the same rubbing-induced negative birefringence but only the isotactic PS led to bulk alignment. The PVBC we used was atactic and exhibited rubbing-induced negative birefringence. No LC alignment perpendicular to the rubbing direction could be observed with PVBC-coated substrates. (A weak interaction between the oriented polymer backbone and the LC molecules might be responsible for the observed weak alignment of the LC monolayer parallel to the rubbing direction.)

For the obliquely evaporated SiO_x substrates, our results suggests that the groove mechanism for the bulk LC alignment is dominant. In an LC monolayer, the LC-LC interaction is negligible compared to the LC-substrate interaction. Hence, a

monolayer of liquid crystal should not show any preferred alignment in the absence of surface-induced ordering. This is the case with the obliquely evaporated SiO_x substrates as our measurements show that the LC monolayer is isotropically distributed. Application of the "groove" model to silanes is somewhat controversial since there are conflicting reports on whether rubbing actually creates grooves on the silane-coated substrate. Our finding of no azimuthal anisotropy in the LC monolayer on such a substrate suggests that the short-range interaction is not responsible for the homogeneous bulk alignment. The above descriptions of the LC-substrate interactions are also consistent with the orientational wetting behavior of the various substrates.[5] Ellipsometry measurements show that the orientational order of a bulk nematic is greatly reduced near the surface of grooved substrates, implying that, locally, the LC molecules favor an isotropic alignment.[31] On the other hand, on the rubbed polymers, orientational order is clearly enhanced near the surface.

To connect our pictures with the anchoring energy results, we first realize that the latter are not a direct measure of the interaction between the LC monolayer and the substrate. We expect that for the rubbed polymer case, the interaction energy $U_{LC\text{-}substrate}$ per molecule is significantly larger than $U_{LC\text{-}LC}$ per molecule. If the anchoring energy were equivalent to $U_{LC\text{-}substrate}$, then for a measured polar anchoring energy of ~ 1 erg/cm^2, for example, we would have $U_{LC\text{-}substrate}$ 3×10^{-15} erg/molecule. This is less than $U_{LC\text{-}LC} \sim kT \sim 4 \times 10^{-14}$ erg/molecule, contrary to what one expects.

The anchoring energies are actually macroscopic quantities. They are related, by definition, to the orientation order parameter near a surface. A smaller order parameter results in a smaller anchoring energy. For example, a weakening of the anchoring energy on evaporated SiO_x and rubbed surfactant coated substrates as the LC approaches the isotropic-nematic phase transition is a manifestation of a reduction of the order

parameter near the surface.[29] For the polymer-coated substrates, the large surface-induced order parameter is the source of the measured high anchoring energy.

We can, however, establish a clear connection between the anisotropy in the surface LC monolayer alignment and the anchoring energies. We know from our measurements that rubbing on the polymer surface induces an anisotropic distribution in the adsorbed LC monolayer. The harder we rub, the more azimuthally anisotropic is the distribution while the polar orientation of the monolayer remains unchanged. These results are consistent with the surface anchoring energy measurements on rubbed polyimide[30]: the azimuthal anchoring energy was found to be linear in the rubbing strength while the polar anchoring energy was independent of the rubbing strength. This is expected since the polar angle distribution of LC molecules at the surface is determined by the bonding between the molecule and the surface and therefore is not likely to be influenced by rubbing. On obliquely SiO_x and rubbed MAP-coated substrates, our SHG measurements indicate that the surface LC monolayer is isotropically distributed in the plane. The azimuthal anchoring energy on these substrates was found to be appreciably smaller than on rubbed polyimide. The finite anchoring energy in these cases, however, shows again that it is not a direct measure of the LC-substrate interaction but is affected by interaction throughout the interfacial regime. In fact, the adsorbed LC monolayer should be considered as part of the substrate. We can then describe the interfacial LC-substrate interaction as occurring between the adsorbed LC monolayer and the LC bulk. Knowing the distribution of LC molecules on the surface is obviously the first step to understanding this interaction on a microscopic level. By combining the SHG results with the results from ellipsometry measurements, which can tell us the interfacial profile of the order parameter, we could expect to find a clearer picture for the surface-induced LC alignment both microscopically and macroscopically.

In conclusion, we have demonstrated that optical SHG can be used to determine quantitatively the orientational distribution of a monolayer of molecules adsorbed on a substrate. Application of the technique to liquid crystal monolayers on various substrates allows us to study how a surface can induce a bulk LC alignment. It was shown that a rubbed polymer surface can effectively align the LC monolayer along the rubbing direction, and then via the epitaxy-like LC-LC interaction, the alignment is extended to the bulk. On obliquely evaporated SiO_x and rubbed surfactant-coated surfaces, the LC monolayer was found to orient isotropically in the azimuthal plane. This indicates that the surface-induced homogeneous bulk alignment arises from minimization of the elastic interaction in the interfacial region constrained by the grooves on the boundary surface. Our results can be correlated with the known values of anchoring energies on these surfaces.

Appendix A: Local Field Corrections for Polyimide-coated substrates

In order to determine accurately the value of $\chi^{(2)}_{eff}$, we must calculate the macroscopic local field corrections (or Fresnel coefficients) to the incident laser fields and to the SH field generated at the interface. The general expressions for the local field factors, $L(\Omega)$ (where $\Omega=\omega$ for the incident field and $\Omega=2\omega$ for the SH field), are derived in Chapter 2. In this Appendix, we will outline the derivation of the local field factors used to analyze our SH signal from polymer-coated substrates. By taking into account the multiple reflections due to the finite thickness of the polymer films, we improve the accuracy of our local field factors by approximately 15%. Separate expressions must be derived for the the case when the monolayer of liquid crystals is in air and when it is in contact with the LC medium. The two geometries we must consider for the polymer coated substrates are pictured in Fig. 9.

The input local field factors for both systems are straightforward. For the monolayer case pictured in Fig. 9a, we can apply the rule of continuity of E_x, E_y and D_z across the interface to show that the input field in the polymer film is given by:

$$L^a_{xx}(\omega) \equiv \frac{E_x(\omega)|_{source}}{E_x(\omega)|_{laser}} = [\,1 - r_p\,]$$

$$L^a_{yy}(\omega) \equiv \frac{E_y(\omega)|_{source}}{E_y(\omega)|_{laser}} = [\,1 + r_s\,]$$

$$L^a_{zz}(\omega) \equiv \frac{E_z(\omega)|_{source}}{E_z(\omega)|_{laser}} = [\,1 + r_p\,]\left[\frac{n_2}{n_m}\right]^2 \qquad \text{(A3)}$$

where $r_{s,p}$ denotes the field reflection coefficient of the s or p polarized light reflected from the interface. We have,

$$r_k = \frac{r_{12k} + r_{23k}e^{2i\beta}}{1+r_{12k}r_{23k}e^{2i\beta}} \quad , \tag{A4}$$

where medium 1 = air, medium 2 = polymer, medium 3 = substrate, k = s or p polarization, r_{12} and r_{23} are linear Fresnel reflection factors at interface 1,2 and interface 2,3, respectively, and $\beta = \frac{2\pi}{\lambda_o} n_2 \, h \cos\theta_2(\omega)$, with λ_o being the laser wavelength in air, h the thickness of the polymer film, and $\theta_2(\omega)$ the transmission angle in the polymer film as determined by the continuity of the tangential component of the wavevector. The values we used for the indices of refraction are listed in Table 3. Note, for h going to zero, these equations are equivalent to Eq. (A1).

The input local field factors for the cell case, as pictured in Fig. 9b, must take into account the transmission through the air/substrate interface and transmission through the polymer film. We find

$$L^b_{xx}(\omega) = \frac{E_{source}}{E_{laser}}\Big|_x = t_p t_{13p}$$

$$L^b_{yy}(\omega) = \frac{E_{source}}{E_{laser}}\Big|_y = t_s t_{13s}$$

$$L^b_{zz}(\omega) = \frac{E_{source}}{E_{laser}}\Big|_z = t_p t_{13p}\left(\frac{n_4}{n_m}\right)^2, \tag{A5}$$

where $t_k = \frac{t_{32k}t_{24k}}{1+r_{32k}r_{24k}e^{2i\beta}}$, media 1,2,3 are air, polymer, and substrate, respectively, medium 4 corresponds to liquid crystal bulk, and β is defined earlier. If the LC is in

the nematic phase, the uniaxial property of the LC needs to be considered in calculating $t_{s,p}$.

The local field factors for the second harmonic output in the geometries of Fig. 9a can also be found. We will present the derivation for the s-component of the monolayer case, i.e. $L_{yy}(2\omega)$, in detail; the derivation of $L_{xx}(2\omega)$, and $L_{zz}(2\omega)$ is similar (see Fig. 9a). Two SH fields radiate from the LC monolayer, one in the reflected direction (-z direction) and one in the transmitted direction (+z direction). The field radiated in the +z direction will reflect off the polymer/substrate interface, leading to an additional contribution to the output field. The total contribution to the field radiating into medium 1 is

$$E_{detected,s} = E_{s_1} + r_s' E_{s_2} . \qquad (A6)$$

According to Eq. (A2), the fields are written as

$$E_{s_1}(2\omega) = \frac{4\pi i\omega \sec\theta_1(2\omega)}{c\sqrt{\varepsilon_1(2\omega)}} L^R_{yy}(2\omega) p^s_y \; ; E_{s_2}(2\omega) = \frac{4\pi i\omega \sec\theta_2(2\omega)}{c\sqrt{\varepsilon_2(2\omega)}} L^T_{yy}(2\omega)\, p^s_y$$

where $L^R_{yy}(2\omega)$ and $L^T_{yy}(2\omega)$ are the output local field factors for the air/polymer interface and have the same form as Eq. (A1) and $r_s' = \frac{r_{23k} t_{21k} e^{2i\beta}}{1+r_{12k} r_{23k} e^{2i\beta}}$ is the field reflection coefficient for the radiation back into medium 1. Using the general definition for $\mathbf{L}(2\omega)$ as given in Eq. (A2), we have for the y-component of $\mathbf{L}$ of the thin-film system,

$$L_{yy}(2\omega) = L^R_{yy}(2\omega) + \sqrt{\frac{\varepsilon_1(2\omega)}{\varepsilon_2(2\omega)}} \frac{\sec\theta_2(2\omega)}{\sec\theta_1(2\omega)} L^T_{yy}(2\omega)\, r_s' . \qquad (A7)$$

With the known expressions of $L^{R}_{yy}(2\omega)$ and $L^{T}_{yy}(2\omega)$, we can rearrange Eq. (A7) to obtain

$$L_{yy}(2\omega) = 1 + r_s ,$$

where r_s is defined in Eq. (A4). Thus, the output local field factor for the thin-film polymer sample has the same form as the input local field factor with the indices of refraction at 2ω, as in the case of a single interface. After carefully calculating the p-polarized SH radiation for a monolayer adsorbed onto a polymer-coated substrate in a similar manner, we find the expressions for $L_{xx}(2\omega)$, and $L_{zz}(2\omega)$ are also identical to the forms for the input field in Eq. (A3).

The output local field factors for the cell geometry pictured in Fig. 9b are derived in a similar way, except that we do not have to worry about the field radiated in the positive z-direction. Taking into account the transmission through each interface, we derive expressions that are identical in form to the input local field factors of Eq. (A5) for the same system.

Appendix B - Local Field Corrections for Obliquely-Evaporated SiO_x Substrates

SHG from a clean, obliquely-evaporated SiO_x surface shows an anisotropic dependence on the sample rotation about the surface normal. The observed signal is pictured in Fig. 8a. Since we know the SiO_x to be locally isotropic, we attribute the observed anisotropy to a geometrical effect. SEM pictures of obliquely-evaporated SiO_x substrates indicate that the surface morphology is very complicated and, hence, difficult to model. Here, we present a qualitative model by assuming that the surface can be described by a saw-tooth structure.

The saw-tooth surface is modelled as a single wedge of angle $\eta = 10$ degrees with the surface plane. To calculate the dependence of SHG on sample orientation, we must first transform the input fields from the lab frame (x,y,z) with $\hat{z}$ along the surface normal and $\hat{y}$ parallel to the grooves, to the local frame, (x, y',z'), with $\hat{z}'$ along the the wedge surface normal and $\hat{y}'$ perpendicular to the $\mathbf{k}$-$\hat{z}'$ plane where $\mathbf{k}$ is the wavevector (see Fig. 8d), calculate the SHG generated from the isotropic surface locally, and then transform the generated SH fields back to the lab frame. With the chosen local coordinates, the local plane of incidence lies in the $\hat{x}'$-$\hat{z}'$ plane. This allows us to use the same local field factors defined in Eq. (A1) to calculate the SHG in the local frame. The Euler transformation from the lab frame to the local frame consists of three rotations,

$$\mathbf{R} = \mathbf{R}_3\mathbf{R}_2\mathbf{R}_1$$

where

$$\mathbf{R}_1 = \begin{pmatrix} \cos\Phi & \sin\Phi & 0 \\ -\sin\Phi & \cos\Phi & 0 \\ 0 & 0 & 1 \end{pmatrix}; \quad \mathbf{R}_2 = \begin{pmatrix} \cos\eta & 0 & \sin\eta \\ 0 & 1 & 0 \\ -\sin\eta & 0 & \cos\eta \end{pmatrix}; \quad \mathbf{R}_3 = \begin{pmatrix} \cos\psi & \sin\psi & 0 \\ -\sin\psi & \cos\psi & 0 \\ 0 & 0 & 1 \end{pmatrix}$$

R_1 corresponds to a rotation about the lab $\hat{z}$-axis through an angle Φ, R_2 is a rotation through the wedge angel η about the $\hat{y}$-axis parallel to the grooves, and R_3 is a rotation about ψ about the $\hat{z}'$-axis to make the $\hat{x}$-$\hat{z}$ plane coincide with the local plane of incidence. We find, from the geometry,

$$\psi = \arctan\left[\frac{\sin\Phi\sin\theta_1}{\cos\eta\cos\Phi\sin\theta_1 - \sin\eta\cos\theta_1}\right],$$

where θ_1 is the angle of incidence in the lab frame.

The effect of the wedge surface on the azimuthal dependence of SHG is two-fold. First, it leads to a mixing of polarizations of a beam; i.e. a pure s or p input polarization in the lab frame will have both s and p components in the local frame. This mixing will depend on the sample orientation. The wedge also leads to a local angle of incidence that is dependent on sample orientation in the following way:

$$\theta_1' = \arccos(\cos\Phi\sin\eta\sin\theta_1 + \cos\eta\cos\theta_1)$$

where θ_1' is the local angle of incidence. When calculating the SH fields in the local frame, we must use local field factors as defined in Eq. (A1), with the local angle of incidence defined above. This leads to local field factors that are dependent on sample orientation.

The results of the calculation are pictured next to the observed anisotropy in Fig. 8c. As can be seen, the qualitative feature of the observed anisotropy is reproduced.

References

[1]J. Cognard, Mol. Cryst. Liq. Cryst. **51**, 1 (1982).

[2]D. Berreman, Phys. Rev. Lett. **28**, 1683 (1972).

[3]D. Berreman, Mol. Cryst. Liq. Cryst. **23**, 215 (1973).

[4]J. Geary, J. Goodby, A. Kmetz, J. Patel, J. Appl. Phys. **62**, 4100 (1987).

[5]T. Sluckin, A. Poniewierski, *Fluid Interfacial Phenomena* C. Croxton, Eds. (Wiley, New York, 1986), pp. Chapter 5 .

[6]W. Chen, M. B. Feller, Y. R. .Shen, Phys. Rev. Lett. **63**, 2665 (1989).

[7]K. Miyano, Phys. Rev. Lett. **43**, 51 (1979).

[8]H. Mada, J. Chem. Phys. **75**, 372 (1981).

[9]H. Yokoyama, Mol. Cryst. and Liq. Cryst. **165**, 265 (1988).

[10]J. Spong, *et al.*, **338**, 137 (1989).

[11]M. B. Feller, W. Chen, Y. R. Shen, Phys. Rev. A **43**, 6778 (1991).

[12]W. Chen, L. Martinez-Miranda, H. Hsiung, Y. Shen, Phys. Rev. Lett. **62**, 1860 (1989).

[13]G. Marowsky, G. Lupke, R. Steinhoff, L. Chi, D. Mobius, Phys. Rev. B **41**, 4480 (1990).

[14]G. Berkovic, T. Rasing, Y. Shen, J. Opt. Soc. Am. B **4**, 945 (1987).

[15]P. Guyot-Sionnest, H. Hsiung, Y. R. Shen, Phys. Rev. Lett. **57**, 2963 (1986).

[16]C. Mullin, P. Guyot-Sionnest, Y. Shen, Phys. Rev. A **39**, 3745 (1989).

[17]T. Uchida, M. Hirano, H. Sakai, Liq. Cryst. **5**, 1127 (1989).

[18]S. Kuniyosu, *et al.*, Jpn. J. Appl. Phys. **27**, 827 (1988).

[19]S. Ishihara, H. Wakemoto, K. Nakazima, Y. Matsuo, Liq. Cryst. **4**, 669 (1989).

[20]P. G. de Gennes, *The Physics of Liquid Crystals* (Clarendon, Oxford, 1974).

[21]F. Kahn, Appl. Phys. Lett. **22**, 386 (1973).

[22]J. Janning, Appl. Phys. Lett. **21**, 173 (1972).

[23]A. Rapini, M. Papoular, J. Phys. (Paris) Colloq. **30**, C4 (1969).

[24]G. Barbero, E. Miraldi, C. Oldano, M. Pastello, P. Valabrega, J. Phys. (Paris) **47**, 1411 (1986).

[25]S. Naemura, J. Phys. (Paris) Colloq. **40**, C3 (1979).

[26]C. Rosenblatt, J. Phys. (Paris) **45**, 1987 (1984).

[27]S. Faetti, M. Gatti, V. Palleschi, T. Sluckin, Phys. Rev. Lett. **55**, 1681 (1985).

[28]S. Faetti, V. Palleschi, Liq. Cryst. **2**, 261 (1987).

[29]H. Yokoyama, S. Kobayashi, H. Kamei, J. Appl. Phys. **61**, 4501 (1987).

[30]T. Oh-Ide, S. Kuniyasu, S. Kobayashi, Mol. Cryst. Liq. Cryst. **164**, 91 (1988).

[31]G. Barbero, S. Durand, Phys. Rev. A **41**, 2207 (1990).

TABLE 1. Results of fits and distribution function parameters for LC monolayers on polyimide-coated substrates that are rubbed at a variety of rubbing strengths.

Sample]	R_s	d_1	d_2	d_3	$\theta_o(\sigma)$	$\Delta\phi$ (mrad)
1	0	0	0	0	76(5)	<.5
2	1γ	.019	.027	.002	75(7)	<.5
3	3γ	.070	.135	.015	73(5)	<.5
4	5γ	.069	.148	.003	76(7)	<.5
5	10γ	.099	.483	.036	77(5)	1.8
6	hard	.167	.762	.050	77(5)	2.5

Description:

γ: interfacial parameter; function of rubbing pressure

d_i: coefficients for azimuthal distribution function defined in Eq. (11)

θ_o: average molecular polar angle for Gaussian distribution defined in Eq. (10)

σ: width of Gaussian distribution for molecular polar angle defined in Eq. (10)

$\Delta\phi$: rubbing - induced birefringence in polymer films

TABLE 2. Physical properties of polymers used

Polymer Coating	Film Thickness[a] (Å)	% wt/vol solution	Structure	$\Delta\phi$[b] (mrad)	LC Cell Alignment[c]	Monolayer Alignment[d]
Polyimide (PI)	1200		crystalline	2.5	↑ ↑	YES
Polyvinyl-alcohol (PVA)	300	1.5% water	crystalline	.5	↑ ↑	YES
Isotactic Polystyrene (PS-I)	500	1.5% toluene	crystalline	-7	↑ ↔	NO
Atactic Polystyrene (PS-A)	500	1.5% toluene	amorphous	-7	Schlieren	NO
Polyvinyl-benzyl-chloride (PVBC)	600	1.5% toluene	amorphous	-18	Schlieren + ↑	SLIGHT

Description:

a. Thickness of spin-coated films are measured by ellipsometry

b. Rubbing-induced birefringence in polymer films measured by ellipsometry

c. First arrow indicates rubbing direction; second arrow indicates direction of cell alignment relative to rubbing direction. Cell alignment was determined by polarizing microscope.

d. Results of SHG measurements on distribution of 8CB monolayer evaporated onto treated substrates.

TABLE 3. Indices of refraction used to calculate local field corrections

Medium	$n(\omega)$	$n(2\omega)$
air	1.00	1.00
fused silica substrate	1.46	1.50
polyimide	1.60[b]	1.80 + .03i[b]
8CB bulk - isotropic	1.56[a]	1.4 + .2i[b]
8CB bulk - nematic, e	1.65[a]	1.36 + .41i[c]
8CB bulk - nematic, o	1.52[a]	1.45 + .10i[c]
8CB - monolayer (ε_m)	1.00	1.00

[a]. D. A. Dunmar, M. R. Manterfield, W. H. Miller, and J. K. Dunleavy, Mol. Cryst. Liq. Cryst. 45, 127 (1978).

[b]. Reflectivity measurements conducted by authors. Uncertainty in measurements in ±.02.

[c]. Reflectivity measurements conducted by authors. Uncertainty in measurements is 10%.

Figure Captions

Figure 1: The long molecular axis ξ in relation to sample coordinates (x,y,z) and lab coordinates (X, Y, Z = z). θ and ϕ are polar angle and azimuthal angle of $\hat{x}$, respectively, θ_1 is the angle of incidence of the laser beam, and Φ is the sample rotation. The plane of incidence is X-Z. Inset: schematic for the rubbing process. The rubbing direction is along the x-axis in the sample frame.

Figure 2: Schematic depiction of an antiparallel 8CB molecule pair in the bulk.

Figure 3: Molecular structures of polymers studied (except polyimide). a) polyvinyl alcohol (PVA), (b) isotactic polystyrene (PS-I), (c) atactic polystyrene (PS-A), (d) atactic polyvinylbenzylchloride (PVBC).

Figure 4: Square root of second harmonic signal (arbitrary unit) vs. sample rotation Φ from an 8CB monolayers on rubbed and unrubbed polyimide-coated substrates. Open squares are data from unrubbed substrates, filled circles are data from substrates rubbed under a hard pressure, and solid lines are the theoretical fits. The input-output polarization combinations are (a) p-in / p-out; (b) s-in / p-out; (c) s-in / s-out; (d) p-in / s-out. The arrow indicates the rubbing direction defined by the arrow in the inset of Fig. 1. Inset: Schematic of preferred orientation of molecular monolayer described by the orientational distribution function.

Figure 5. Azimuthal orientational distribution functions of an 8CB monolayer on polyimide-coated substrates prepared with different rubbing strengths. The squares were for a sample prepared with a rubbing strength $R_S = 1\gamma$, the circles were for $R_S = 5\gamma$ the squares were for $R_S = 10\gamma$. The solid line corresponds to a sample rubbed with $R_S >> 10\gamma$.

Figure 6. Second harmonic output field (arbitrary unit) vs. sample rotation Φ from an 8CB cell made with rubbed polyimide-coated substrates. Open circles are data from the cell in the isotropic phase, filled triangles are data from the cell in the nematic phase, and solid lines are the theoretical fits for the isotropic case. The input-output polarization combinations are (a) p-in / p-out; (b) s-in / p-out; (c) s-in / s-out; (d) p-in / s-out.

Figure 7. Azimuthal orientational distribution functions of an 8CB monolayer on rubbed polyimide-coated substrate (solid line), and an 8CB interfacial layer between a rubbed polyimide-coated surface and an 8CB bulk (dashed line).

Figure 8. a.) Second harmonic output field (arbitrary unit) vs. sample rotation Ï from a bare obliquely-evaporated SiO_x substrate.

b.) Second harmonic output field (arbitrary unit) vs. sample rotation Ï from an 8CB monolayer on an obliquely-evaporated SiO_2 substrate.

c.) Results of model calculations for output second harmonic field (arbitrary unit) vs. sample rotation Ï from a wedged substrate.

For all three sets of plots, the input-output polarization combinations are (i) p-in / p-out; (ii) s-in / p-out; (iii) s-in / s-out; (iv) p-in / s-out.

d.) Schematic of SiO_x sample

Figure 9. Schematics for the interfaces used to calculate the local field factors for an 8CB molecular monolayer adjacent to a polymer-coated substrate. a) 8CB molecules are in air; b.) 8CB molecules are in contact with 8CB bulk.

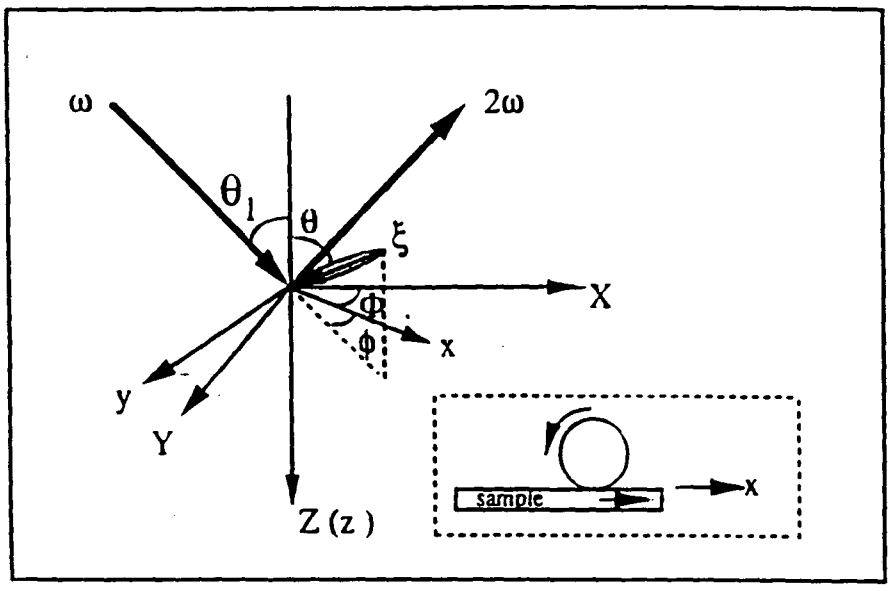

XBL 911-4610

Figure 1

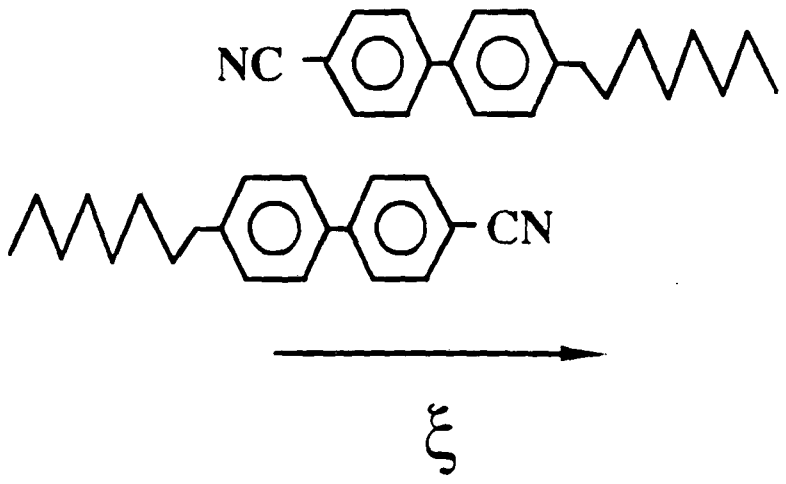

XBL 911-4611

Figure 2

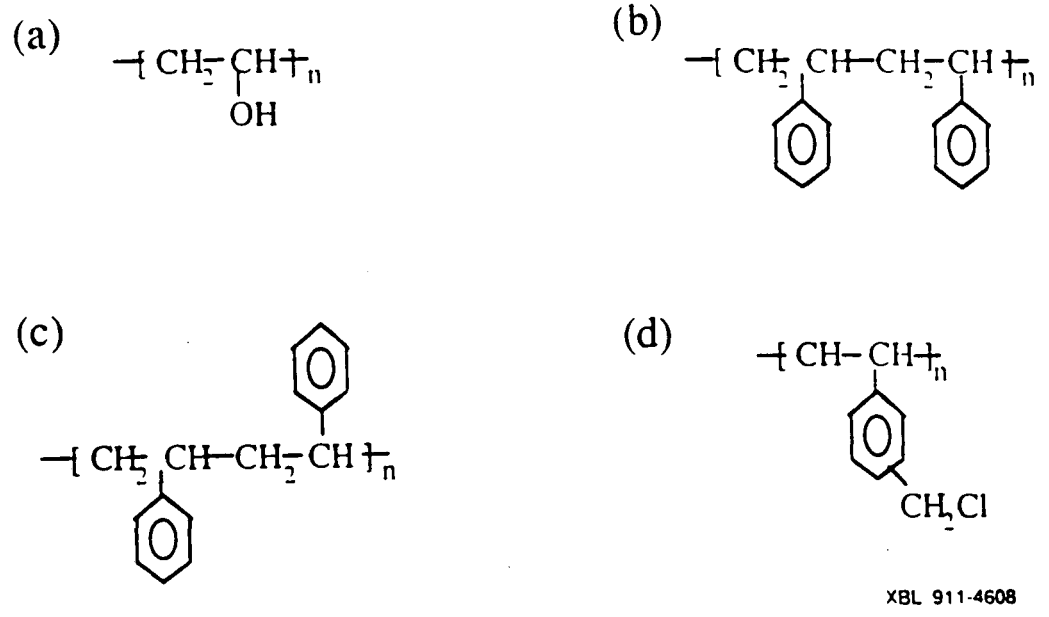

Figure 3

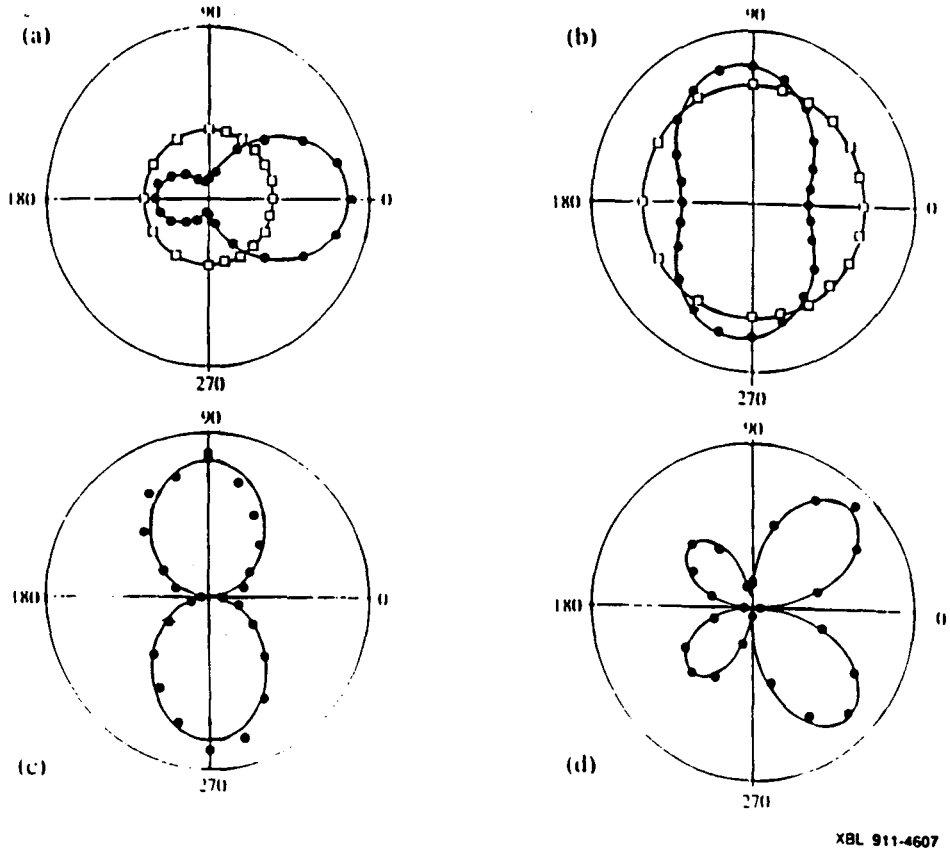
(a)
90
180
0
270
(b)
90
180
0
270
(c)
90
180
0
270
(d)
90
180
0
270
XBL 911-4607

Figure 4

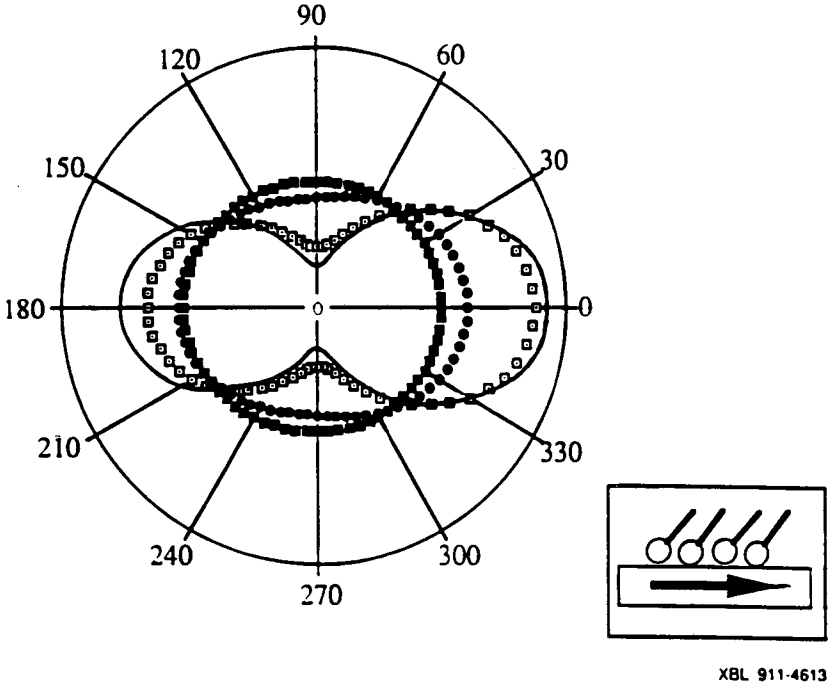

Figure 5

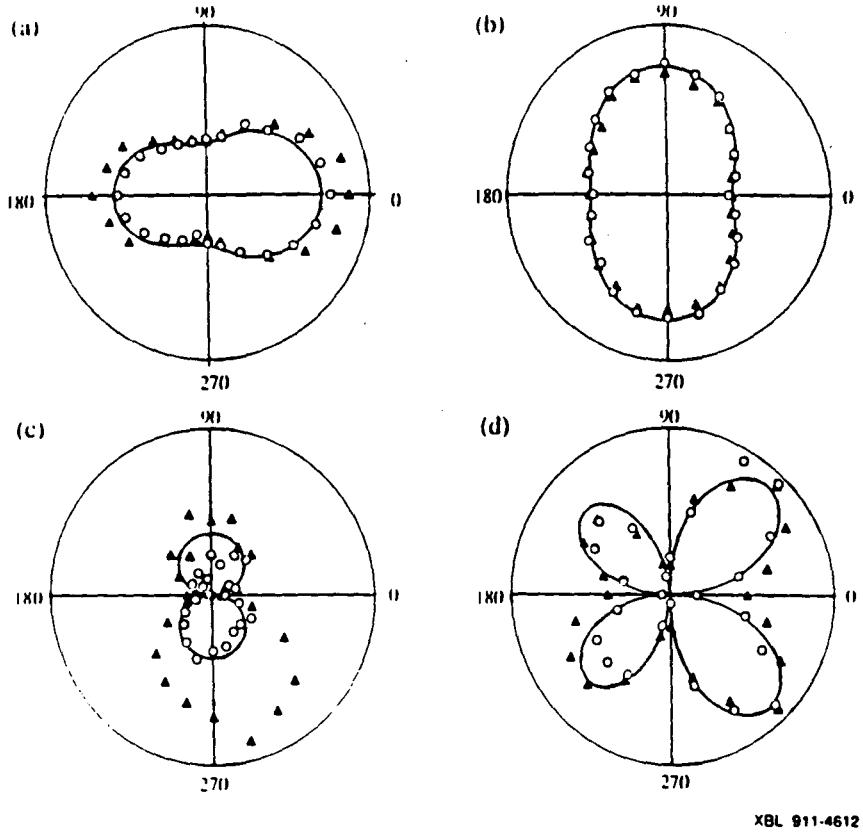
(a)
90
180
0
270
(b)
90
180
0
270
(c)
90
180
0
270
(d)
90
180
0
270
XBL 911-4612

Figure 6

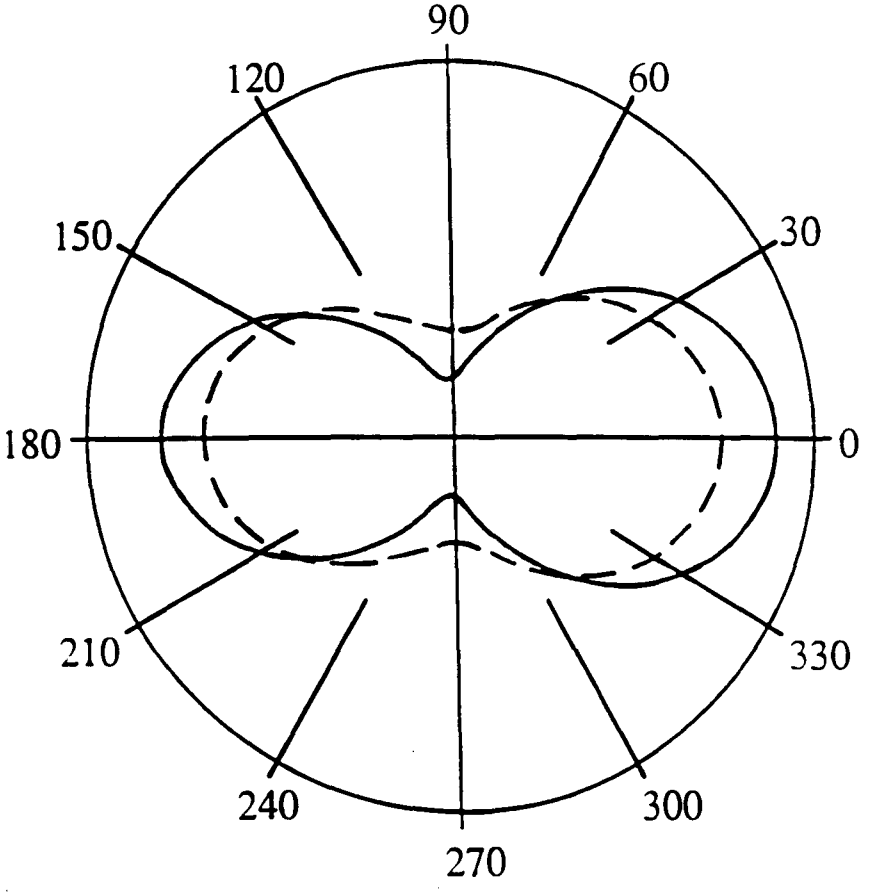

XBL 911-4614

Figure 7

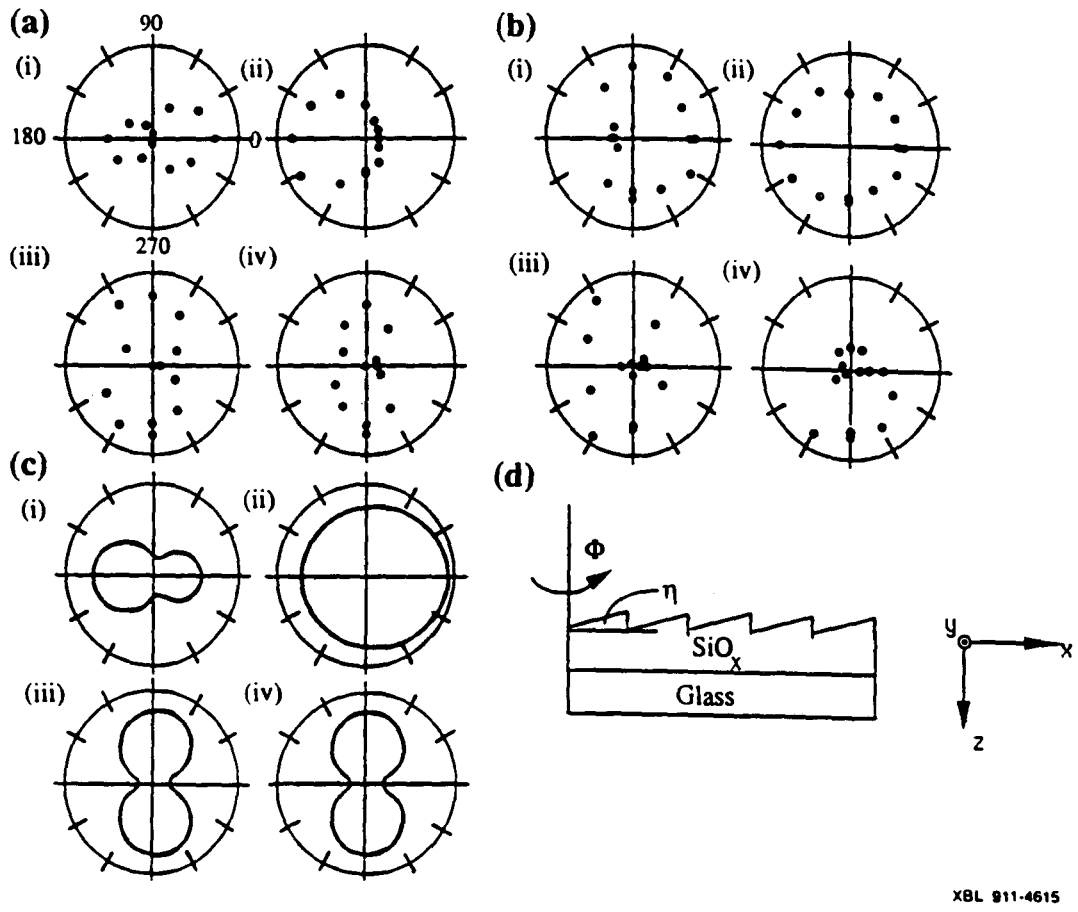
(a)
90
(i)
(ii)
180
0
270
(iii)
(iv)
(b)
(i)
(ii)
(iii)
(iv)
(c)
(i)
(ii)
(iii)
(iv)
(d)
Φ
η
SiOx
Glass
y
x
z
XBL 911-4615

Figure 8

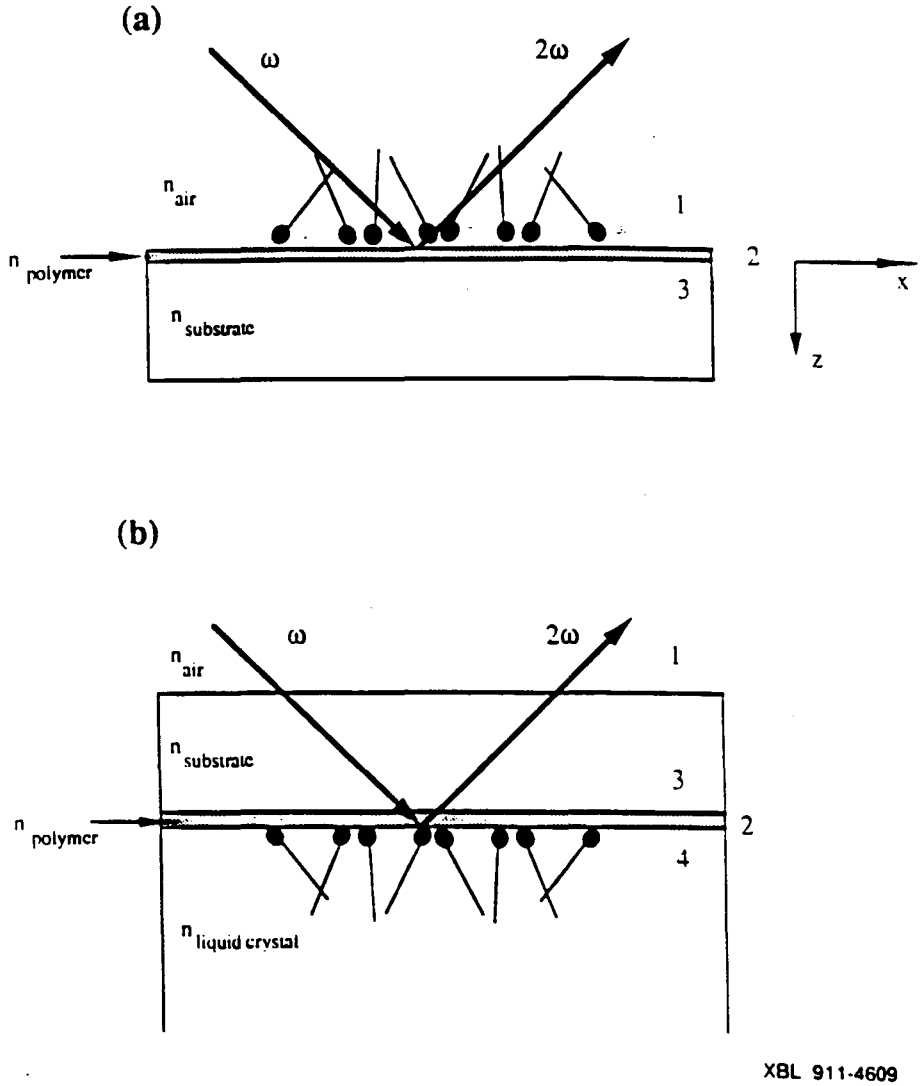
(a)
ω
2ω
n air
1
n polymer
2
3
n substrate
x
z
(b)
ω
2ω
n air
1
n substrate
3
n polymer
2
4
n liquid crystal
XBL 911-4609

Figure 9

V. SHG Investigation of the Memory Effect at an LC-Polymer Interface

A. Introduction

The surface memory effect (SME) is a phenomenon where an initially isotropic surface is rendered anisotropic by being in contact with an ordered LC phase. The SME was first reported by Friedel[1] who found that placing a glass surface in contact with a crystal of rod-shaped molecules rendered the glass anisotropic. The effect was again demonstrated by Noel Clark in 1985[2] with a liquid crystal-polymer interface. He studied the interface between several different polymers and a liquid crystal that has several smectic phases, a nematic phase, and an isotropic phase. He concluded that the SME only occurred on polymers that have hydrophobic surfaces and that only the smectic phases of the liquid crystal could induce the effect. Recently, we studied the SME in cells made from polyimide-coated glass substrates (see Fig. 1). One substrate of the cell was heavily rubbed, the other unrubbed. The liquid crystal is introduced into the cell in the isotropic phase. It is then cooled to a smectic phase with a temperature gradient, so the smectic layers will nucleate from the rubbed surface, leading to alignment of the cell. Initially, in the nematic phase, there is very poor bulk ordering. After the cell has been in the smectic A phase for more than 12 hours, the nematic phase exhibits mono-domain ordering. The cell can then be heated to the isotropic phase and when cooled to nematic phase again, the ordering will remain. Hence, the smectic phase has somehow "printed" its ordering at the LC-polymer interface. This is the memory effect. If the cell is kept in the isotropic phase for an extended period of time, the memory effect can be destroyed.

What is the origin of this effect ? In Chapter IV, we found that two different surface-originated mechanisms are effective in aligning a liquid crystal bulk: one based on short-range, molecular interactions and the other on more long-range bulk elastic interactions.[3,4] We showed that for rubbed polymers, a short-range molecular interaction is responsible for the alignment of the first monolayer which then aligns the bulk. Since

we observed the memory effect at an LC-polymer interface, we expect that the origin of the memory effect is also short-range in nature, i.e. the smectic A phase has somehow modified the molecular interaction to break the symmetry at the surface in a way sufficient to lead to mono-domain alignment of the nematic phase. As in the rubbed polymer case, we expect this asymmetry to manifest itself in the first monolayer of LC molecules at the interface.

We demonstrated in Chapter IV the ability of the SHG to be used to determine the orientation distribution function of an interfacial monolayer of 8CB in both absence and presence of a bulk of LC. We want to apply this technique to monitor the in-plane asymmetry of the first layer of LC molecules next to a substrate that has undergone the memory effect. The asymmetry of the orientation of the molecules will give a quantitative measurement of the magnitude of the effect. By combining these results with pretransitional birefringence results, we can develop a thorough understanding of the interface and start to understand the nature of the LC-polymer interaction that leads to the SME.

In this Chapter, we will report on the details of the SHG studies on the problem of the surface memory effect. In Sec. B, we will apply the results of Chapter IV to show how SHG can be used to quantitatively measure the anisotropy of the LC monolayer at an SME interface. The bulk contribution, including the contribution from the smectic phase, will be discussed. In Sec. C, we will present the experimental results for SHG measurements of the interfacial monolayer for several different phases of the LC cell. The results from a variety of other measurements that were conducted by members of the group will be summarized in Sec D. Finally, in Sec. E, the possible mechanism for the surface memory will be discussed in the context of all the experimental results, and a quantitative analysis of the measured anisotropy will be presented.

B. General SHG Considerations

Since we studied the SME at a bulk LC/polymer interface, the analysis in Chapter IV, Sec. B applies to this problem. However, in contrast to the rubbed surface which had a single mirror plane of symmetry, there is nothing to break the symmetry parallel and antiparallel to the rubbing direction at the "printed" surface, so we can expect a surface susceptibility with C_{2v} symmetry.[5] This implies there are only three independent, nonvanishing components of χ :

$$\chi^{(2)}_{zzz} = N_s < \cos^3\theta > \alpha^{(2)}_{\xi\xi\xi}$$

$$\chi^{(2)}_{zyy} = \chi^{(2)}_{yzy} = \chi^{(2)}_{yyz} = N_s < \cos\theta - \cos^3\theta > < 1 - \cos^2\phi > \alpha^{(2)}_{\xi\xi\xi}$$

$$\chi^{(2)}_{zxx} = \chi^{(2)}_{xzx} = \chi^{(2)}_{xxz} = N_s < \cos\theta - \cos^3\theta > < \cos^2\phi > \alpha^{(2)}_{\xi\xi\xi} \qquad (1)$$

where ϕ is the azimuthal angle defined in Fig. 1, Chapter IV.

The above nonvanishing elements of $\chi^{(2)}$ can be measured by surface SHG as described by Eq. 7 in Chapter IV. These equations are simplified due to the higher symmetry of the surface: For s-in/p-out,

$$\chi^{(2)}_{eff} = \chi^{(2)}_{zxx} \sin^2\Phi\, L_z(2\omega) L^2_y(\omega) \sin\theta_1(2\omega) + \chi^{(2)}_{zyy} \sin^2\Phi\, L_z(2\omega) L^2_y(\omega) \sin\theta_1(2\omega)$$

For p-in/p-out

$$\chi^{(2)}_{eff} = \chi^{(2)}_{xxz} \cos^2\Phi \{2 L_x(2\omega) L_x(\omega) L_z(\omega) [-\cos\theta_1(2\omega) \cos\theta_1(\omega) \sin\theta_1(\omega)]$$

$$+ L_z(2\omega)L_x^2(\omega)\sin\theta_1(2\omega)\cos^2\theta_1(\omega)\}$$

$$+\chi^{(2)}_{yyz}\ \sin^2\Phi\{2L_x(2\omega)L_x(\omega)L_z(\omega)[-\cos\theta_1(2\omega)\cos\theta_1(\omega)\sin\theta_1(\omega)]$$

$$+ L_z(2\omega)L_x^2(\omega)\sin\theta_1(2\omega)\cos^2\theta_1(\omega)\}$$

$$+\chi^{(2)}_{zzz}\left[L_z(2\omega)L_z^2(\omega)\sin\theta_1(2\omega)\sin^2\theta_1(\omega)\right].$$

For p-in/s-out,

$$\chi^{(2)}_{eff}=\left(\chi^{(2)}_{xxz}-\chi^{(2)}_{yyz}\right)\sin2\Phi\, L_y(2\omega)L_x(\omega)L_z(\omega)[-\sin\theta_1(\omega)\cos\theta_1(\omega)] \qquad (2)$$

We expect no signal for the s-in/s-out polarization combination.

The bulk contributions will be the same as those in Chapter IV, Eq. 12-13. Note, all of the surface components are mixed with bulk components. We rewrite Eq. 12 from Chapter IV here for convenience.

$$\chi^{(2)}_{zxx}=\chi^{surface}_{zxx}-\frac{\chi^{Q}_{zzxx}}{\varepsilon(2\omega)}$$

$$\chi^{(2)}_{zzz}=\chi^{surface}_{zzz}-\frac{\chi^{Q}_{zzzz}}{\varepsilon(2\omega)\varepsilon^2(\omega)}$$

$$\chi^{(2)}_{zyy}=\chi^{surface}_{zyy}-\frac{\chi^{Q}_{zzyy}}{\varepsilon(2\omega)}$$

where

$$\chi^{Q}_{ijkl} = \frac{1}{2} N_B < H^{\xi\xi\xi\xi\xi\xi}_{ijkl} > \alpha^{(2)}_{\xi\xi\xi\xi\xi\xi} \xi_o \qquad (3)$$

and $H^{\xi\xi\xi\xi\xi\xi}_{ijkl}$ is a function of $<P_2>$ and $<P_4>$, the Legendre components of the order parameter. We used $<P_2> = .65$ and $<P_4> = .175$ for the smectic A phase (T=25° C), and $<P_2> = .55$ and $<P_4> = 0$ for the nematic phase (T=35°C).[6]

The experiment is identical to that described in the last chapter; we measure the SHG as a function of Φ and fit the results to the above equations to deduce the values of $\chi^{(2)}_{ijk}$. The parameter we will use to characterize the monolayer anisotropy is,

$$A = \frac{<\cos^2\phi> - <\sin^2\phi>}{<\cos^2\phi>} = \frac{\chi^{(2)}_{zxx} - \chi^{(2)}_{zyy}}{\chi^{(2)}_{zxx}}$$

The value of *A* varies between zero for a completely isotropic surface to one. Since the SME has an extremely small effect on the monolayer distribution, it is necessary to define a minimum detectable anisotropy. The estimate for the minimum detectable values for *A* was based on how much anisotropy must exist in the data so that a significant improvement in the fit occurs when we have $\chi^{(2)}_{zxx} - \chi^{(2)}_{zyy} \neq 0$, which is determined by our signal-to-noise ratio. The signal-to-noise for observing the interfacial LC monolayer in the presence of the bulk of LC is significantly smaller than for a monolayer in air because of the small variation in the index of refraction across the polymer/bulk LC interface (leading to a smaller values for the macroscopic local field factors), and because of the fluorescence from the bulk.

Since all of the effective surface susceptibilities have bulk contributions, special care must be taken to independently determine the monolayer anisotropy. In the isotropic phase, $\langle P_2 \rangle$ and $\langle P_4 \rangle = 0$ which implies

$$\chi^{Q}_{zzxx} - \chi^{Q}_{zzyy} = 0$$

Hence, in the isotropic phase, the anisotropy of the monolayer, A , can be measured independent of a bulk contribution. Any reorientation of the interfacial molecules that occurs during the smectic A phase "printing" should persist when the bulk is in the isotropic phase. Otherwise, keeping the system in the istropic phase for even a short eriod of time would destroy the memory effect. Hence, the SHG measurement in the istropic phase will give us the clearest indication of an anisotropy in the monolayer distribution. Since the non-isotropic phases of the bulk generate anisotropic contributions to the SHG, we need to have a reliable value for the bulk signal to be able to determine the surface contribution in these phases. By comparing the value of $\chi^{(2)}_{zxx} - \chi^{(2)}_{zyy}$ in the nematic and isotropic phases, we can deduce the value of the bulk contribution, assuming the monolayer distribution does not change. Though the bulk contribution is known from previous experiments,[7] this gives us an independent calibration. We can then use this value of the bulk to deduce the values of the surface contributions from the fitting parameters for all phases.

The data analysis in the smectic phase is somewhat complicated by the fact that the bulk alignment has a "Chevron" structure orients the smectic layers approximately 7 degrees with respect to the surface normal.[8] By doing a coordinate transformation to the local frame and calculating the bulk contribution, we see an apparent asymmetry in the alignment that might be constructed as an anisotropic surface contribution. See Appendix A for a derivation of the expected signal from a tilted, smectic bulk alignment.

We used the macroscopic local field factors $L(\Omega)$ as derived in Chapter IV-A for the data analysis. For the nematic and smectic phase data, we approximated the anisotropic indices of refraction by the values for the isotropic phase 8CB in the calculation of the local field corrections (see Table 1, Chapter IV). This allowed us to assume isotropic local field factors that were independent of the sample orientation, greatly simplifying the analysis. The anisotropy in the indices of refraction for the mesophases is at most 10% , leading to an uncertainty in the local field factors of less than 10%. Hence this approximation does not significantly increase the uncertainty of the data analysis in the values of the χ's.

C. Experimental Arrangement

The experimental set-up was identical to that of the experiments described in Chapter IV: we used a frequency-doubled, CW-modelocked, Q-switched, Nd:YAG laser as the pump beam for the second harmonic. To improve the signal to noise, we added a reference arm consisting of a photodiode (EG&G FND-100) to monitor the power of the 532 nm light coming from the laser. The output of the diode was read by a gated integrator; we normalized all of our data to the square of the diode output. We also took independent scans of the fluorescence contribution by detuning the monochromator by 5 nm from the peak of the SHG. See Figure 2 for an a plot of the fluorescence vs wavelength for a monolayer of 8CB molecules on a polymer-coated substrate in air and for a cell.

The samples used were quite similar to ones used in the bulk experiments described in the last chapter. We used the liquid crystal 8CB in these experiments, which has a smectic A to nematic transition at T_{AN}=33.5° C and a nematic to isotropic transition at T_{NI}=40.5°C. We spin-coated polyimide (JIB-1, Japan Synthetic Rubber) onto fused silica substrates and baked the substrates for 60 minutes at 150°C to dry the polymers. This is in contrast to Clark's work, where he left the polymers "wet" so they would be more pliable. One substrate was subject to "hard rubbing" which corresponded to a rubbing

strength greater than 20γ on the scale defined in the last chapter; the other substrate was left unrubbed. The liquid crystal was introduced into the cells in the isotropic phase. The sample was cooled to the smectic phase with the rubbed side at a lower temperature than the unrubbed side. This allowed the smectic A layers to nucleate on the rubbed side and propagate their order through the cell to the other substrate. A single cell was made with two different size spacers, one 75 microns and one 25 microns. This was done so we could spatially separate the beam reflected at the top interface from the beam reflected at the bottom interface, since the substrates are not parallel. The bulk ordering in the cell was monitored by a polarizing microscope.

D. SHG Experimental Results

We monitored the SHG from the interface of a cell as a function of sample orientation for an 8CB cell made of one rubbed and one unrubbed polyimide-coated glass slide for a variety of phases. We looked at the phases in the following order: a) the initial isotropic phase; b) the nematic phase; c) smectic A immediately after the nematic phase; d) the smectic A phase 2 days later; e) the smectic A phase 3 days later; f) the nematic phase; g) the isotropic phase and ; h) the nematic phase. An example of the results are presented in Fig. 3. For each experimental geometry for each phase, we did an independent scan of the fluorescence so that we could subtract its contribution from each data point. For the p-in/p-out and s-in/p-out geomtry, the fluorescence was less than 10% of the total detected signal. However, the SHG generated in the s-in/s-out configuration was difficult to discern from the fluorescence background, which is consistent with our assumption that our surfaces have C_{2v} symmetry (see Fig. 3). Only in the smectic A phase did we detect any SHG for the p-in/s-out geometry significantly above the fluorescence background. In the smectic phase, the SHG data versus sample orientation, Φ, has C_{1v} symmetry, implying a breaking of the symmetry parallel and anti-parallel to the rubbing direction. This anisotropy can be explained by the chevron-structure bulk contribution (see Appendix

A). (Note, we saw this asymmetry immediately after the cell went into the smectic phase, i.e. before the memory effect had time to take effect, further indicating it is not an interfacial effect associated with the SME. The signal from the smectic A phase was identical for the entire three dayswe kept the sample in this phase.) The value of A was determined for each of the monolayer distributions by fitting Eq. 2 to the data. The results are summarized in Table 1.

Since the measured anisotropies are so low, it is important to determine the minimum detectable anisotropy. We estimate that we can measure an $A = 7\%$ for an LC monolayer in contact with a bulk of LC. This estimate was based on the signal-to-noise of our data, which is significantly smaller for observing the interfacial LC monolayer in the presence of the bulk of LC than for a monolayer in air. From the monolayer measurements reported in the last chapter, we estimate that the minimum detectable anisotropy in the absence of an LC bulk is 1%.

To test whether the memory effect somehow affected the rubbed side of cell, we did a series of SHG measurements to monitor the in-plane symmetry of the monolayer next to the rubbed-polymer substrate. We saw a strong anisotropy similar to that described in Chapter IV, but we observed no change in the monolayer alignment during the "printing" process.

To take advantage of the better sensitivity to anisotropies in monolayer alignment for LC monolayers in air, we compared the texture of an SME cell with the texture of a cell that is made of one strongly rubbed side and one weakly rubbed side. This will allowed us to roughly "calibrate" the monolayer alignment on the "printed" substrate with previous measurements done on monolayer distribution vs. rubbing strength. It appears that a substrate aligned with 3γ rubbing strength (barely touching, passed 3 times under a stationary wheel) leads to the same texture as the SME cell. The anisotropy of a monolayer distribution on this substrate was approximately 3%, so it was consistent with the SHG results above. When the cell alignment was compared with a cell made with a substrate

with a rubbing strength of 1γ, the quality of the alignment as observed through a polarizing microscope was much worse. The anisotropy of a monolayer on a 1γ-rubbed substrate is 1%. This implies that the anistropy of the monolayer is somewhere between 1% and 3%.

E. Other Experimental Results

In this section, we briefly summarize other measurements that were carried out by Yukio Ouchi and Tom Moses on SME cells. First, to give a clearer demonstration that the "printing" of the smectic alignment occurred on the unrubbed side of the cell, the two plates of the cells were twisted with respect while the cell was in the isotropic phase and then cooled to the nematic phase. A polarizing microscope was used to determine whether the bulk LC alignment was twisted or whether it remained parallel to the rubbing axis of the rubbed polymer-coated substrate. Since the length scale of the twisted bulk (on the order of 25 micron) is much longer than the wavelength of the light, the polarization of the light propagating through the cell should follow the twist of the LC bulk director. Hence, if the bulk of the LC twists, one of the polarizers on the microscope will have to be rotated the same amount as the substrate in order to extinguish the light. They found they could see a twisted alignment for the plates twisted 90 degrees with respect to each other . If the unrubbed side had been unaffected by the smectic phase of the LC, the alignment in the cell would simply follow the rubbed side instead of remaining anchored to the unrubbed side. This is strong evidence that the "printing" does occur on the unrubbed side of the cell.

They also conducted ellipsometry measurements to determine the pre-transitional wetting behavior of the printed substrates in the istropic phase approaching the nematic-istropic transition. They first looked at rubbed polymer-coated substrates and found that there was strong pretransitional wetting, implying a large surface order parameter at the rubbed polymer-coated substrates. When they repeated the measurements for the printed substrate, they saw absolutely no pretransitional wetting behavior. This sets an upper limit

on the surface order parameter of .02, implying a very weak orientational coupling between the polymer and the LC bulk. Though it is difficult to directly compare the surface order parameter and the monolayer distribution quantitatively, the two measurements have yielded consistent results.

We also found that is was possible to destroy the memory effect by keeping the sample at an elevated temperature. We found that if we kept the cell at 80°C, the effect was detroyed in 3 hours. If we kept the cell at 60°C, it took 10 hours to destroy the effect. To estimate the strength of the interaction that is responsible for the memory effect, we can assume a simple diffusion model, described by the equation

$$\frac{1}{\tau} \propto \exp(-\frac{U}{kT})$$

From these two measurements, we can estimate the well-depth to be on the order of 80 kT. Later, a more careful set of measurments were done on how long it takes to destroy the effect for different temperatures. By assuming the same diffusion model, the depth of the potential well was estimated to be 82 kT.

F. Discussion

Our samples have clearly demonstrated a surface memory effect, i.e the smectic ordering of the bulk of the LC has changed the LC-polymer interface in some reversible way that enables the interface to align a bulk nematic. In Chapter IV, we presented the two possible mechanisms for surface-induced alignment of LC cells - a short-range molecular interaction and a bulk elastic interaction. It is extremely unlikely that the bulk smectic A phase has printed grooves into the polymer so that a bulk elastic interaction would be responsible for the cell alignment. Hence, the origin of the memory effect must be a short-range molecular interaction between the LC molecules and the polymer which enhances the

azimuthal coupling. This interaction could be a modification of the polymer surface, or it could be that the smectic A phase deposits LC molecules in an ordered fashion onto the polymer where they remain pinned. Our SHG measurements indicate that the printing of the anisotropic ordering of the smectic A phase has a very weak effect on the orientation of the first layer of LC molecules at the interface. The sensitivity of the direct measurements of the interfacial layer are limited by the signal-to-noise ratio to measure an anisotropy of 7%. The detected anisotropy was less than 7%, below the minimum detectable anisotropy. However, by comparing to aligning ability of substrates rubbed at different strengths, we know that the anisotropy lies somewhere between 1% and 3%. The ellipsometry measurements also indicate a very weak coupling between the interface and the LC bulk. So, what is going on?

To discuss these results in terms of a physical picture, it is useful to relate our results to the surface anchoring energy of the interface. To date, no surface anchoring energy measurements have been conducted on a "printed" surface, so a quantitative comparison of our results is difficult. However, a discussion of the anchoring energy for this system can give a good qualitative understanding of the nature of the rotational coupling that is responsible for the surface memory effect.

As discussed in the last chapter, the anchoring energy is a macroscopic parameter that is a measure of the interfacial interaction. It has two contributions - one that is a measure of the interaction between the first monolayer and the substrate, and a second which is a measure of the strength of the coupling between the first monolayer and the bulk.[9] The two contributions to the free energy from the interface can be written as

$$\mathcal{F}_{\text{interfacial}} = \frac{1}{2}\frac{U_{\text{LC-substrate}}}{a^2}\theta^2(0) + \int_0^a K_I(z)\left(\frac{\partial\theta}{\partial z}\right)^2 dz$$

where $\theta(z)$ is the orientation of the director at a position z in the cell, $\theta(0)$ is the orientation of the director at z=0, $K_I(z)$ is the interfacial elastic constant, and a is the width of the interfacial regime. Physically, $\theta(0)$ corresponds to a finite interaction between the substrate and first layer of LC and $K_I(z)$ corresponds to variations in the elastic constant due to changes in the LC interactions. The contributions to $K_I(z)$ are broken into two categories: energetic (Van der Waals LC-LC interactions) and entropic (excluded volume and order parameter variations). The Maier-Saupe theory of LC-LC interactions lead to an elastic constant that depends on the square of the order parameter. I will refer to the first term in the expression as the coupling between the LC and the polymer and the second term as the interfacial contribution to the anchoring energy.

The anchoring energy is mathematically defined as the difference in free energy for a system with an interfacial regime, and the free energy of a system that has no interfacial region, i.e. behaves like a bulk nematic all the way to the substrate. We can relate this definition to the expression presented in the last chapter through the following definition:

$$\mathcal{F}_{\text{interface+ bulk}} - \mathcal{F}_{\text{bulk}} = \int_0^a (K_I(z) - K_B)\left\{\frac{\partial\theta}{\partial z}\right\}^2 dz = \frac{1}{2} U_{\text{interaction}}\theta_o^2$$

where θ_o is defined as the angle the first layer of molecules makes with respect to the easy axis and $\mathcal{F}_{\text{bulk}}$ is given by

$$\mathcal{F}_{\text{bulk}} = \int_0^\infty K_B\left(\frac{\partial\theta}{\partial z}\right)^2 dz .$$

where K_B is the bulk elastic constant. By minimizing the free energy using the Euler-Lagrange equations, we can solve for $\theta(z)$ throughout the entire LC cell. By using the

boundary condition $\theta(z) = \theta_0$, we can relate θ_0 to the known physical parameters of the system. Thus, we can use this equation to derive an expression for $U_{interaction}$, the surface anchoring energy coefficient.

Previous measurements on the azimuthal anchoring energy at polymer-coated substrates indicate a significant rotational coupling between the LC bulk and the polymer.[10, 11] Their results can be attributed to the interfacial contribution since pretransitional wetting experiments indicate a strong surface-induced ordering of the bulk in the isotropic phase near the isotropic-nematic transition Our recent SHG results[3, 4] show that the reorientation of the polymer causes a strongly aligned monolayer that persists in the isotropic phase indicating that the LC-polymer interaction is also strong. In contrast, the LC-polymer interface that has undergone the memory effect has an extremely small surface order parameter, implying the interfacial contribution to the anchoring energy will be insignificant. However, the size of the LC-polymer interaction is less clear. The measurement of an 80 kT well-depth for the rotational potential wells indicates a very strong interaction between the LC molecules and polymer. However, the SHG results indicate that very few of these potential wells exist, i.e there are not a large number of sites where molecules are attached anisotropically. Given the strong coupling between the monolayer and the substrate, and the weak coupling between the monolayer and the bulk, it is hard to predict what would be the measured strength of the surface anchoring energy.

It is important to note that although the measured anisotropy of the monolayer is weak, it is sufficient to align a bulk of liquid crystal in the nematic phase. The nematic phase is composed of many domains that exhibit orientational ordering. If the bulk nematic is in contact with any small perturbation to break the symmetry, it costs very little energy for these domains to become a single domain. Thus it is possible for a very weakly perturbing surface, like one that has undergone the SME, to lead to monodomain alignment of the nematic phase.

In conclusion, we have applied the technique of surface second harmonic generation to study the surface memory effect at an LC-polymer interface. We found the anisotropy of the interfacial monolayer to be below the minimum detectable anisotropy of our technique for measuring the monolayer in the presence of an a bulk of LC. By describing the interface in terms of the anchoring energy, we know that the interfacial contribution to the anchoring energy is weak since the ellipsometry measurements of pretransitional behanvior measured a very small sureface order parameter. The LC-polymer interaction can be described by rotational potential wells, whose depths we measured to be quite large (80 kT) but which are sparsely located, since they do not lead to a measurable anisotropy in the monolayer distribution. This is the first microscopic characterization of an interface that has undergone a memory effect

Appendix A - SHG Bulk Contribution from the Smectic-A Phase

SHG from a homogeneously aligned LC cell in the Smectic-A phase shows an anisotropic dependence on the sample rotation about the surface normal. We attribute this to the fact that Smectic-A chevron-layer structure occurs at 7° with respect to the surface normal. Since we trying to isolate the surface contribution that is mixed with a bulk, this anisotropy could be mistaken for an anisotropic surface contribution. Here we present a calculation that predicts how this bulk contribution will depend on sample rotation (see Fig. 4).

The calculation occurs in the following five steps:

1. Relate the incident field to the field within the LC medium with macroscopic local field corrections $L(\omega)$ as defined in Appendix IV-A.

2. Transform the fields from the lab coordinates (x,y,z), where $\hat{z}$ is along the surface normal and $\hat{x}$ is parallel to the direction of rubbing, to the local LC frame (x',y',z'), where $\hat{x}'$ is parallel to the director, and $\hat{z}'$ is normal to the LC molecules. The Euler transformation from the lab frame to the local frame consists of two rotations,

$$R = R_2 R_1$$

where

$$R_1 = \begin{pmatrix} \cos\Phi & \sin\Phi & 0 \\ -\sin\Phi & \cos\Phi & 0 \\ 0 & 0 & 1 \end{pmatrix}; \quad R_2 = \begin{pmatrix} \cos\psi & 0 & \sin\psi \\ 0 & 1 & 0 \\ -\sin\psi & 0 & \cos\psi \end{pmatrix}$$

R_1 corresponds to a rotation about the lab $\hat{z}$-axis through an angle Φ, R_2 is a rotation of the director through ψ which we know from x-ray data to be 7°.

3. Calculate the SHG in the local frame from the bulk contributions of the LC pairs listed in Eq. 3 of the text.

4. Transform back to the lab frame to get the SHG field in the LC medium

5. Use output local field factor L(2ω) to relate SHG field in LC medium to detected field.

The results of the calculation are shown in Figure 5. Also shown is the expected signal from the smectic bulk with the molecules parallel to the surface. Note, the tilted smectic bulk contribution has the same symmetry as the rubbed monolayer, namely there is a single mirror plane symmetry parallel to the rubbing direction. The magnitude of the contribution.is on the order of 10% of the surface contributions. See Fig. 6 for a comparison of the calculated bulk contribution to the measured contribution from both the surface and bulk.

References

[1]G. Friedel, Ann. Phys. (Paris) **18**, 273 (1922).

[2]N. A. Clark, Phys. Rev. Lett. **55**, 292 (1985).

[3]W. Chen, M. B. Feller, Y. R. .Shen, Phys. Rev. Lett. **63**, 2665 (1989).

[4]M. B. Feller, W. Chen, Y. R. Shen, Phys. Rev. A **43**, 6778 (1991).

[5]Note the LC film has a "Chevron" structure which implies that the symmetry parallel and anti-parallel to the rubbing direction may be broken. See Figure 5a. However, this anisotropy associated with the Chevron structure is very small, and bulk observations indicate that Chevron structures kinked parallel to the rubbing direction are equally likely as structures kinked in the opposite direction. Since the assymmetry is so weak, we do not expect it to break the monolayer symmetry, though it will manifest itself in the bulk contribution, as described later in the text. See Reference 8.

[6]M. Constant, D. Decoster, J. Chem. Phys. **76**, 1708 (1982).

[7]P. Guyot-Sionnest, H. Hsiung, Y. R. Shen, Phys. Rev. Lett. **57**, 2963 (1986).

[8]Y. Ouchi, Y. Takanishi, H. Takezoe, A. Fukuda, Jpn. J. Appl. Phys. **28**, 2547 (1989).

[9]P. G. de Gennes, *The Physics of Liquid Crystals* (Clarendon, Oxford, 1974).

[10]H. Yokoyama, Mol. Cryst. and Liq. Cryst. **165**, 265 (1988).

[11]T. Oh-Ide, S. Kuniyasu, S. Kobayashi, Mol. Cryst. Liq. Cryst. **164**, 91 (1988).

Table 1: Results of data fits.

Phase	$\chi^{surface}_{zzz}$	$\chi^{surface}_{zxx}$	$\chi^{surface}_{zyy}$	A
	($\times 10^{-16}$ esu)			(%)
a) istropic	1.75	11.8	11.7	.8
b) nematic	1.37	11.6	11.5	.8
c) smectic	1.87	16.6	15.0	1.0
d) nematic	.65	16.5	16.3	1.2
e) isotropic	1.2	15.85	15.1	4.7
f) nematic	.65	15.90	15.3	3.8

Figure Captions

Figure 1: Schematic of memory effect. a) The first cell is prepared with one rubbed polymer-coated substrate and one unrubbed substrate. The LC is introduced into the cell in the isotropic phase. b)The cell is cooled to the nematic phase. Multidomain nematic ordering is observed. c) The cell is cooled to the Smectic-A phase, with the rubbed substrate at a colder temperature than the unrubbed. The cell has monodomain smectic A ordering. The cell is held at this temperature for more than 24 hours. d) The cell is then heated to the nematic phase. Monodomain ordering is observed. If the cell is heated to the isotropic phase for a short period of time and then cooled back down to the nematic phase, the monodomain ordering remains. All bulk alignment observations were made through a polarizing microscope.

Figure 2: Fluorescence vs. wavelength for a) a monolayer in air, and b) a monolayer in an LC cell.

Figure 3: Square root of second harmonic signal (arbitrary units) vs. sample rotation Φ from 8CB cell in several phases of the memory effect. Circles are data and the solid lines are fits. For each phase we have shown the data for the p-in/p-out polarization combination in the left column, and the data for the s-in/p-out polarization combination in the right column. The signal plotted has the fluorescence contribution subtracted off. a.) Initial isotropic phase, b) Smectic phase, c)Nematic phase after unrubbed substrate has undergone the memory effect, d) Isotropic phase after substrate has undergone memory effect.

Figure 4: SHG and fluorescence vs. sample rotation Φ from 8CB cell in nematic phase for s-in/s-out polarization combination. Open circles are SHG signal and closed circles are fluorescence; There is no significant difference between the two.

Figure 5: a) Geometry assumed for the calculation describe in Appendix A; b.) Results of model calculations for output second harmonic field vs. sample rotation Φ from a smectic-A bulk that is tilted by 7° with respect to the interface; c.) Results of the calculation for a smectic-A bulk that is aligned parallel to the interface.

Figure 6: Comparison on magnitude of the calculated smectic A contribution to the results of the data fit. Though the bulk is approximately 10% the size of the total measurd signal, it can account for the asymmetry parallel and anti-parallel to the rubbing direction observed in the data.

a) Isotropic Phase

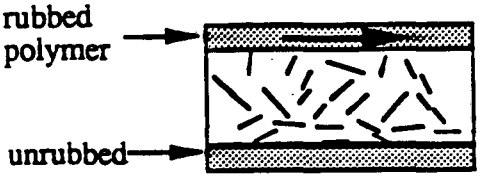

b) Nematic Phase

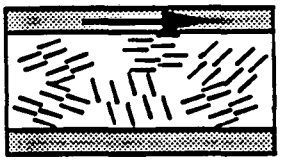

c) Smectic-A Phase

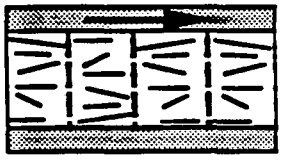

d) Nematic Phase

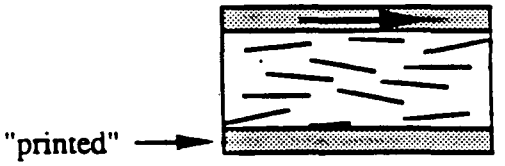

Fig. 1

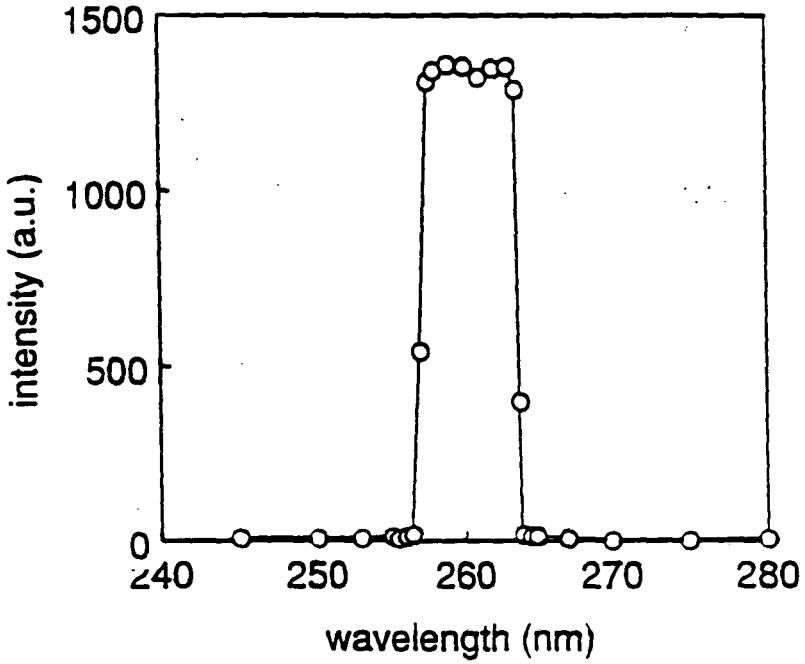
1500
1000
500
0
intensity (a.u.)
240
250
260
270
280
wavelength (nm)

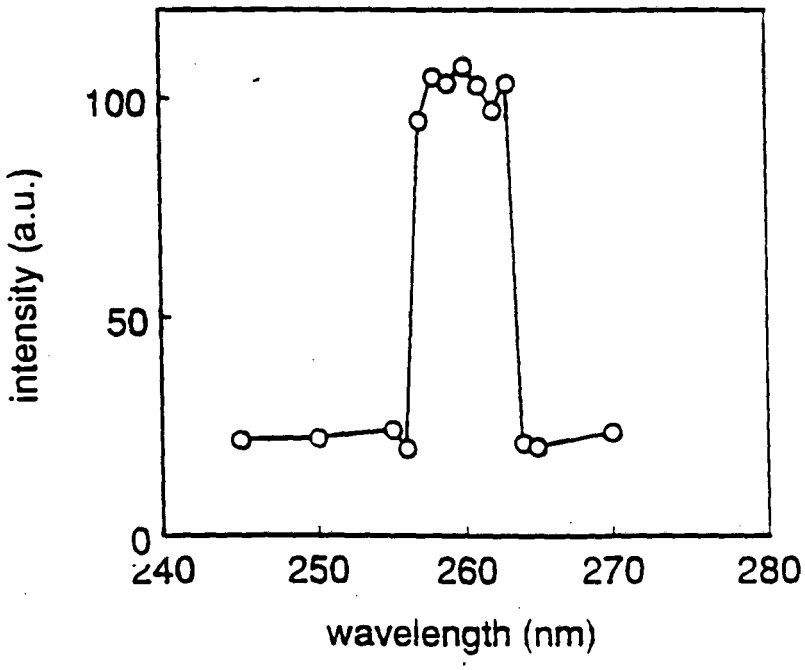
100
50
0
intensity (a.u.)
240
250
260
270
280
wavelength (nm)

Fig. 2

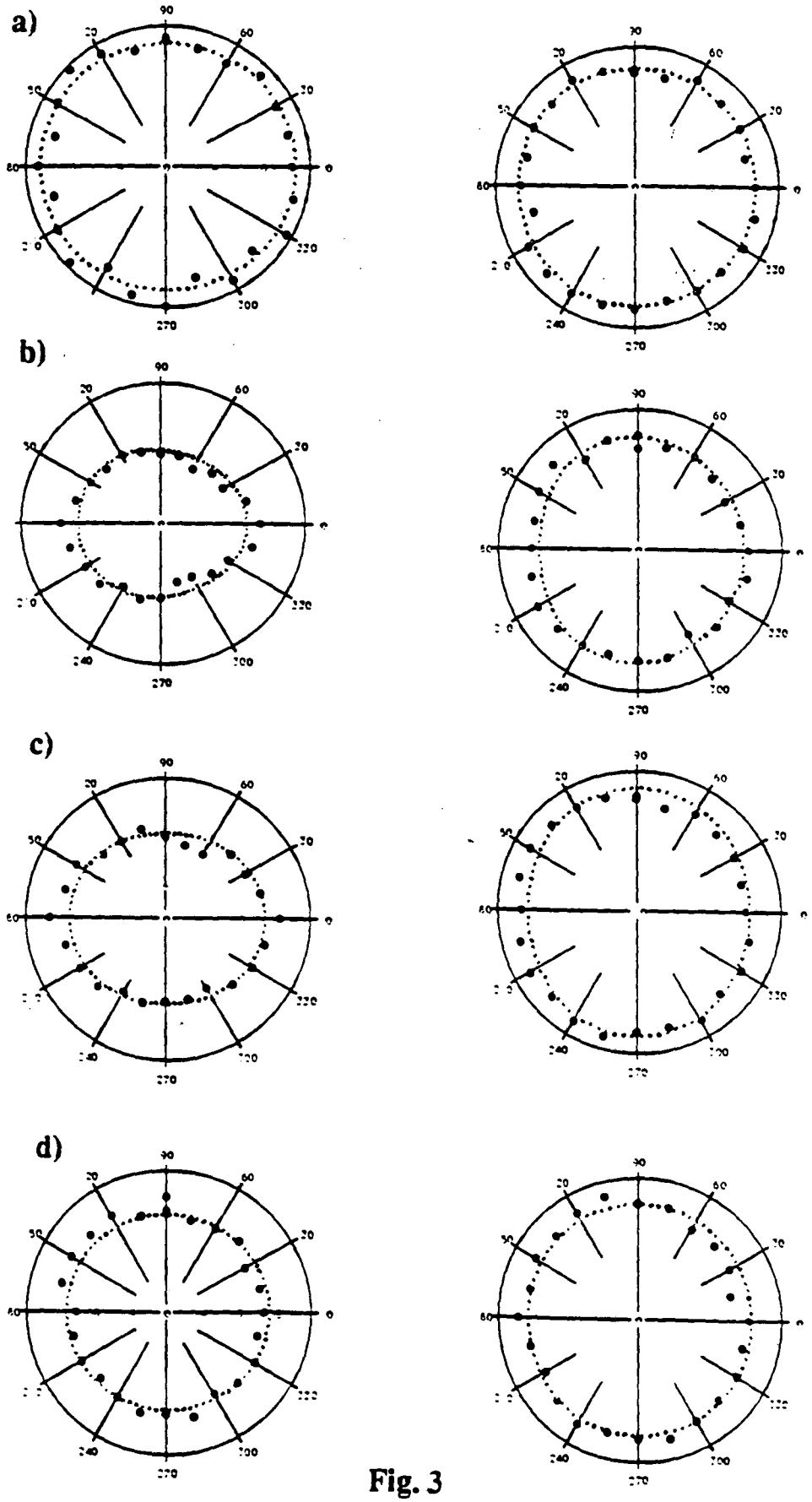

Fig. 3

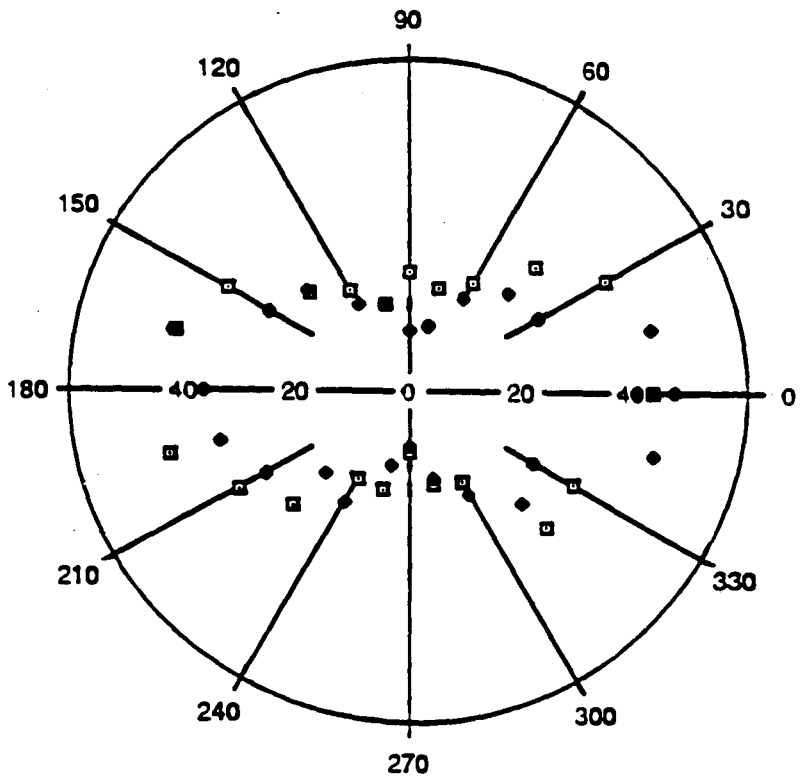

Fig. 4

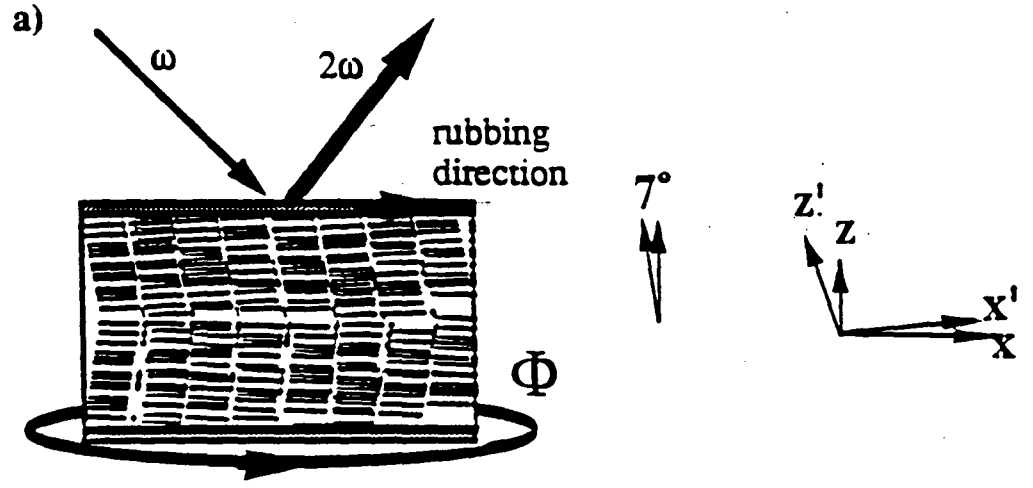

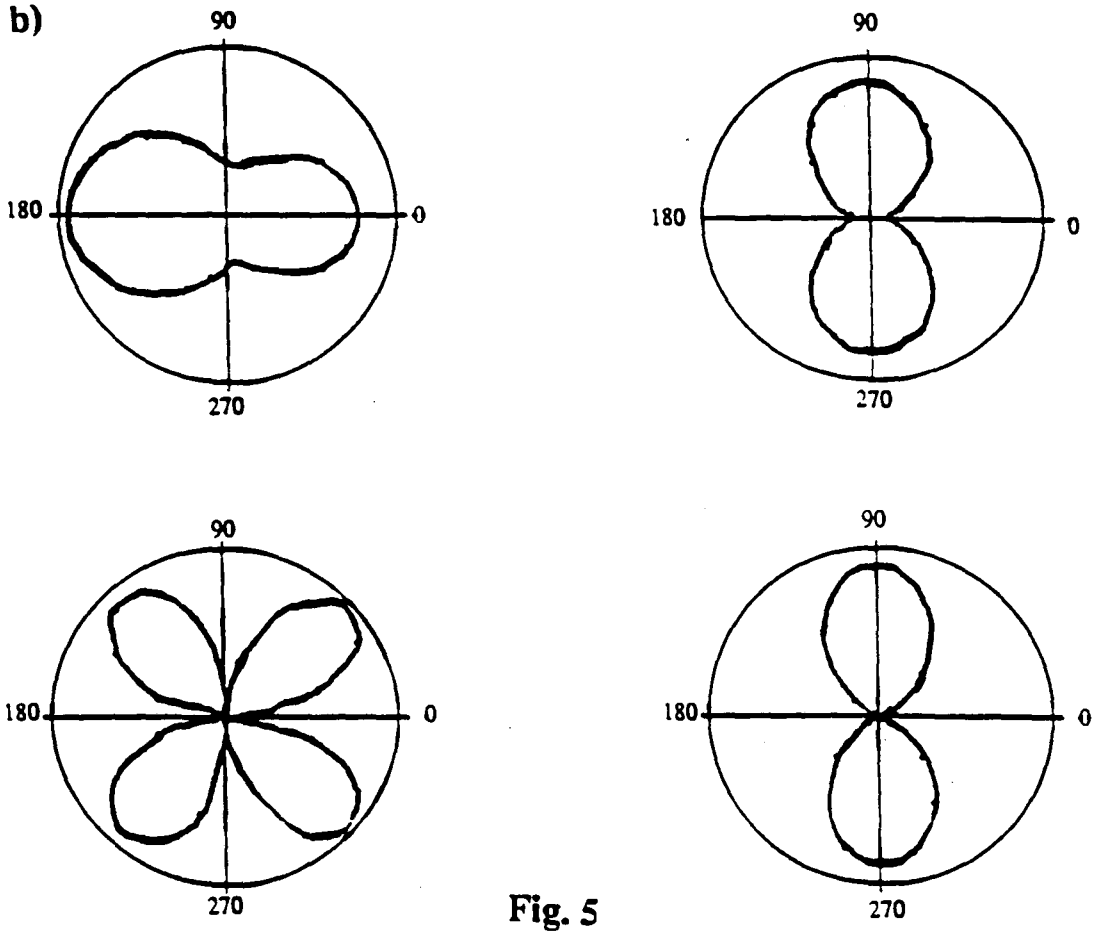

Fig. 5

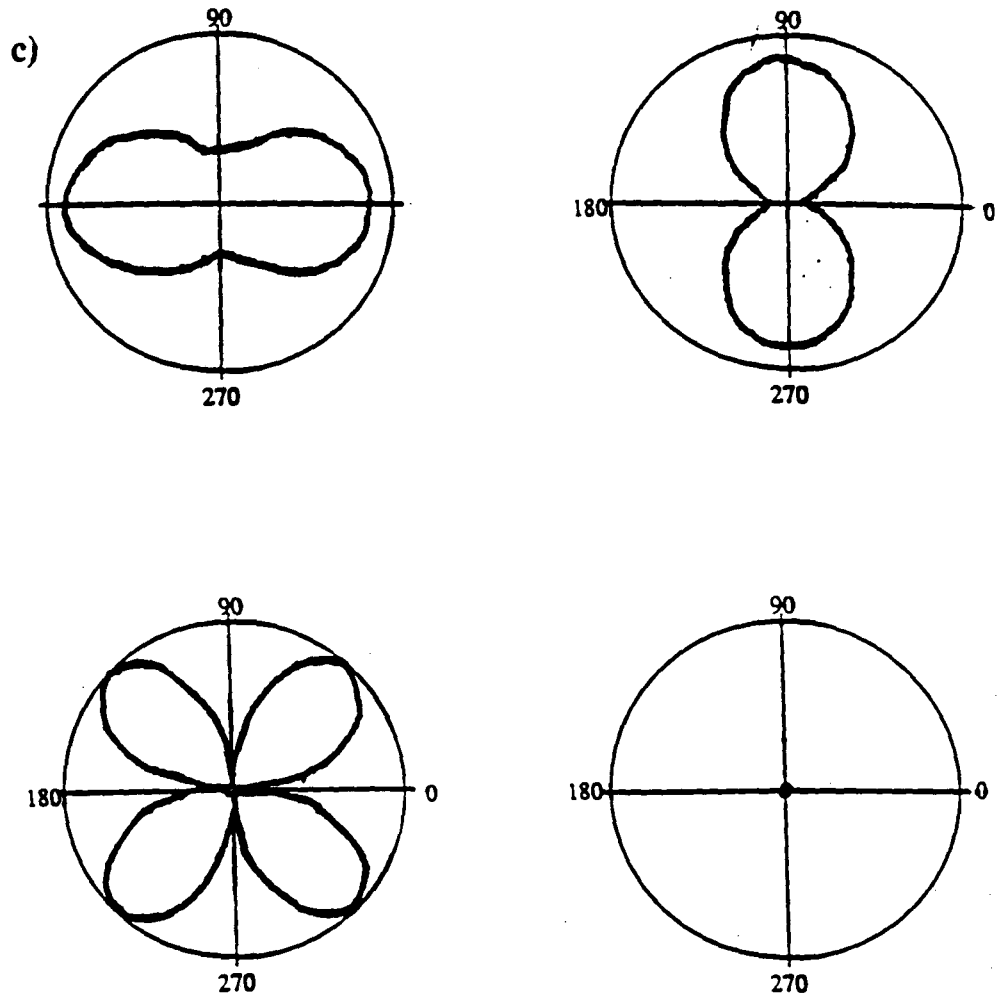

Fig. 5

a)

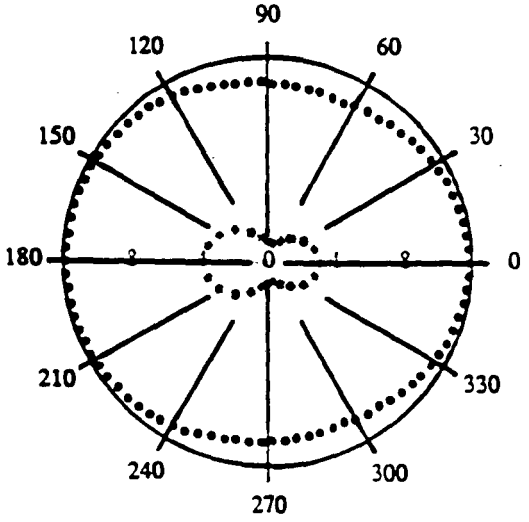
90
120
60
150
30
180
0
210
330
240
300
270

b)

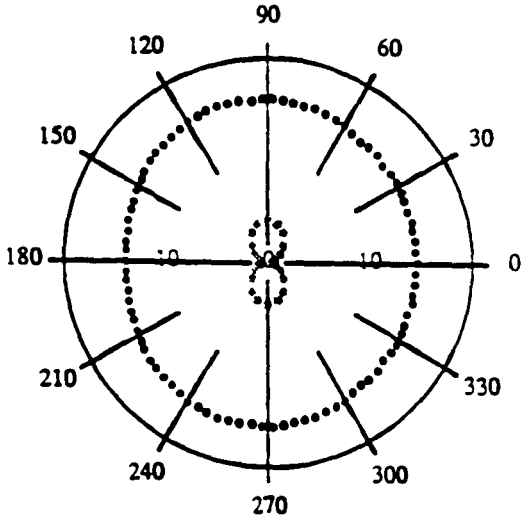
90
120
60
150
30
180
0
210
330
240
300
270

Fig. 6

VI. Construction of an Amplified Tunable Picosecond Dye Laser

We were interested in doing a time-resolved measurement to identify the process responsible for generation of second-harmonic light in a gaseous medium. To do this, we needed a tunable picosecond laser of 10^7-10^8 W/cm^2. The experimental set-up consisted of a synchronously pumped dye laser that was amplified at 10 Hz. The dye laser is pumped by a CW-modelocked neodimium-doped yttrium-lanthenum-fluoride (Nd:YLF) laser with a repetition rate of 100 MHz. The components for the Nd:YLF laser were purchased from Quantronix corporation. The second harmonic generation unit, the dye laser, and the amplifier chain were all built in our laboratory and in the Department shops.

A. The Nd: YLF Laser

In the last few years, researchers have been using Nd:YLF lasers to replace Nd:YAG lasers as a pump source for dye lasers to produce picosecond and subpicosecond optical pulses. CW lasing operation of a Nd:YLF crystal was first reported and carefully characterized,[1] elucidating the advantages and disadvantages of Nd:YLF as a replacement for Nd:YAG. Nd:YLF crystals have a three times larger spectral linewidth than Nd:YAG, allowing it to generate shorter pulses. Also, the index of refraction of Nd:YLF has a much weaker dependence on temperature, so it does not have the strong thermal focussing that occurs in Nd:YAG lasers. Nd:YLF has a birefringence that is much larger than thermally induced depolarization. This leads to more stability against thermal fluctuations. It is uniaxial, so it has a naturally polarized output at two emission wavelengths, at 1.053 for light polarized parallel to the c-axis of the crystal, and 1.047 micron for light polarized perpendicular. Its fluorescence lifetime is twice as long as Nd:YAG, so it has a lower lasing threshold and good potential as a Q-switched source. The major drawback to using a Nd:YLF crystal is that the crystals are not as high an optical quality as Nd:YAG and hence cannot make large diameter rods. Since the emission cross-section or Nd:YLF at

1.053 micron is lower than the emission cross-section of Nd:YAG at 1.06 micron, it does not generate as high average power. It was demonstrated, that replacing a Nd:YAG crystal with a Nd:YLF crystal under the same pumping conditions, the Nd:YLF crystal generates less than half the power. Also, shorter pulses, which come from the larger lasing bandwidth, puts more stringent requirements on the mechanical stability of the laser in general, especially the cavity length.

Several of these difficulties were overcome by introducing additional optics into the cavity. First, a spherical lens is needed to expand the beam so that it fills the rod to optimize lasing in the TEM_{oo} mode A cylindrical lens is added to compensate for the asymmetry in the thermal focusing of the light. (More recently, an identical laser head with a crystal whose c-axis is oriented 90 degrees with respect to the first, has been added to the cavity to adjust for this asymmetry dynamically.[2]) Two similar cavity designs consisting of these optics were developed[3] and led to average powers comparable to those produced by Nd:YAG rods on comparable dimensions. The configuration we used is based on a configuration introduced by the Quantronix Corporation (see Fig. 1).

Initially, we tried to harmonically modelock the cavity to further shorten the pulses.[3,4] We used a Fluke synthesizer (Model 6060B) and an ENI amplifier (Model 325LA) to generate the 100 MHZ required to drive the harmonic modelocker (Quantronix, Model 351). Harmonic modelocking proved to be too difficult to achieve due to phase noise in the source and the increased sensitivity of pulse stability to cavity length, so we abandoned the scheme.

We tried several different cavity configurations using the optics of the Quantronix design to optimize several different performance characteristics of the laser, including laser pulsewidth, pulse stability, average power, noise, and pulse jitter. We measured the pulsewidth and the pulse stability using a homebuilt, 500 picosecond scan-range autocorrelator.[5] We measured the pulse energy with a Coherent power meter. We measured the noise (defined as the AC noise divided by the DC offset) with a photodiode

(EG&G, FND100). We measured the pulse jitter by monitoring the pulse position on a 7904 Tektronix Oscilliscope using a set of sampling plug-ins (time base 7T11, amplitude base 7SA and sampling module S-6 terminated in 50 ohms) which had a 35 picosecond time constant and an Antel diode which has a deconvolved time response of 65 psec FWHM. The convolved time response of the system is 100 psec FWHM. The pulse stability and jitter was a sensitive function of the temperature of the modelocker and the RF power to the modelocker. We settled on an operating temperature of 18.0°C for the modelocker bath (Fisher Scientific Model 910), and 15 watts of RF power. For this configuration, we have the following performance characteristics: Average power was 15 watts in a TEM_{00} mode, 55 psec pulse, 2% AC noise/DC offset, and less than 30 psec pulse jitter. See Fig. 2 for an autocorrelation of the pulse.

To determine the propagation properties of the output of our laser, we measured the radius of the beam waist at three locations outside the cavity. The beam cross-sections were fit to gaussian pulse-shapes. By knowing the beam radius at three locations, we were able to use gaussian optics to determine the position and size of the beam waist and the beam divergence. We found a waist of .22 mm was located 7.8 cm from the output coupler outside the cavity. The beam divergence was approximately 1 milliradian. We also performed an ABCD calculation for this cavity. We did not include the thermal lensing effects of the YLF crystal or the cylindrical lens in this calculation. The thermal focusing of the YLF is extremely weak and thus difficult to model properly. Its focal length has been measured experimentally to be +800 cm on the axis parallel to the c-axis of the crystal, and -800 cm perpendicular to the c-axis.[6] The cylindrical lens in introduced to compensate for this asymmetry. The results of these calculations, as performed on the Software PARAXIA™, are drawn in Fig. 1. The results correspond to a waist of .2 mm, located 1 centimeter from the output coupler, which agrees well with our measurement. According to this calculation, the waist of the beam through the YLF crystal is approximately one millimeter. This corresponds to a 2 mm FWHM for the beam, which implied that the 4 mm

rod acts as the aperture in the cavity, cutting off the tails of the beam profile. The maximum beam waist of 2.8 mm FWHM occurs at the spherical lens.

To satisfy the stringent cavity length requirements we built a cavity length feedback, based on a design introduced by Herman Vanherzeele.[6] Instead of using software to perform the feedback, we copied a circuit designed by Tom Moses and John O-Brien.[7] The circuit was designed to compensate for slow thermal drifts in the cavity length. The feedback signal is the voltage produced by the output of a double-balanced mixer (Minicircuits SB-1). This output is proportional to the phase difference of the RF source for the modelocker (Vetron oscillator CO226) and the output of a photodiode (EG&G FND-100) which is monitoring the output of the laser. The output voltage of the feedback circuit drives a piezo translator (Burleigh PZL-007) on which the high reflector of the cavity is mounted. This active stabilization compensates for thermal and mechanical drifts of the cavity and significantly decreases the warm-up time of the cavity.

To pump our dye laser, we needed to frequency double the output of the Nd:YLF laser. We used a 3x3x5 mm potassium titanyl phosphate (KTP) crystal. The nonlinear properties of KTP have been studied extensively.[8] To achieve Type II phase matching for 1.053 micron light the crystal was cut so the surface contained the z-axis and intersected the x-y plane 34 degrees with respect to the crystal x-axis. The reported damage threshold of KTP crystals were as high as 10-30 GW/cm^2 for picosecond pulses,[9, 10] and 2-3 GW/cm^2 for nanosecond pulses.[11] However, we damaged our crystals at intensities around 100 MW/cm^2. To raise the damage threshold of our crystal, we heated the crystal to 100°C. The damage mechanism for KTP crystals is formation of color-center defects that then absorb the green light.[12] The onset of these damage spots can be seen by discolorations in the crystal. If nothing was done, these discolorations would eventually turn into permanent damage spots. We found this discoloration reversible when the crystal was heated for an hour at 100°C. Continuous heating of the crystal slightly changed the indices of refraction, changing the phasematching angle by less than one degree.

The optics used in the second harmonic generation unit are pictured in Fig. 3. We used a half-wave plate to to adjust the polarization of the 1.053 micron output of the laser. The input lens is AR-coated for 1.053 micron. The output lens is AR coated for 527 nm light. The crystal is mounted on a prism mount (Klinger PO32) that allows for adjustments in three angles. The crystal is in contact with a "frigichip" (Melcor), a solid state device that uses the Peltier effect for cooling. By reversing the leads, the chip can be used for heating. The crystal is wrapped in aluminium foil to allow for more uniform heating. We built a circuit that stabilizes the temperature to within 0.1°C. The temperature of the crystal is read via a temperature transducer (AD590AF) which is in thermal contact with the crystal.

We needed 600-800 mW of 527 nm light to pump the dye laser. By positioning the input lens 6 cm from the center of the KTP crystal we generated a waist of approximately 50 microns at the KTP interior, corresponding to a peak intensity of 45 MW/cm^2, which is below the published damage threshold. We found that by focussing a bit harder to approximately a 30 micron waist, we could generate more than 1.5 Watts of 527 nm light, corresponding to a conversion of approximately 10%.

B. Synchronously Pumped Dye Laser

Dye lasers have been used in a variety of configurations to generate short optical pulses.[13] Organic dyes have a broad gain spectrum due to a continuum of vibrational and rotational levels within the ground and excited electronic states. The thermalization of these levels is fast enough to sustain femtosecond pulses. This broad gain spectrum also allows for a wide-range of tunability.[14]

A variety of techniques have been applied to mode-lock dye lasers.[15] We used the technique of synchronous modelocking. Synchronous pumping of a dye laser was first achieved in 1968[16] using the frequency-doubled output of a modelocked Nd:glass laser as

a pump source. When the cavity length of the dye laser matches the length of the pumping resonator, a pulse shortening occurs. This pulse shortening phenomenon can be explained in the following way. Pumping the dye medium with 40 picosecond pulse brings the medium above the lasing threshold for a short period of time in the latter part of the pump pulse. Since the length of the dye laser is nearly the same as the pump laser cavity, the dye laser pulse exists in the gain medium simultaneous with the pump laser pulse. Through stimulated emission, the dye pulse then quickly brings the dye medium below the lasing threshold, resulting in a dye laser pulse that is substantially shorter than the pump laser pulse. A schematic of the synchronous pumping is shown in Fig. 4.

We used the standard three-mirror folded cavity for our synchronously pumped dye laser.[17] A schematic of our cavity is shown in Fig. 5. There are several considerations that went into this cavity configuration. A subcavity is needed in order to create a tight focus in dye jet while maintaining a long enough cavity to match the 100 MHZ repetition rate of the Nd:YLF laser. The subcavity consists of two 5 centimeter focal length mirrors that have thin-film dielectric coatings for the 560-620 nm regime. The mirrors are placed 15 centimeters apart. The dye jet is placed within the subcavity 5 centimeters from the folding mirror and 10 centimeters from the end mirror. The orientation of the dye jet is approximately at Brewsters angle to minimize reflection losses. The angle of the fold in the cavity is chosen to compensate for the astigmatism created in passing through the jet at Brewster's angle.[18] The output coupler is chosen (from an extremely limited selection) to maximize the output power of the cavity. We used a 5% transmission, flat output coupler. The pump beam optics are chosen to maximize the overlap within the jet between the pump beam mode and the TEM_{00} lasing mode of the dye laser cavity. The pump optic had a 5 cm focal length and had a thin-film dielectric coating for 527 nm. We used D-shaped mirrors for the pump optic and the end mirror. This way the pump beam can be located very closely to the lasing beam. Given this cavity configuration, we had an average lasing

power of 160 mW with 600 mW of pump energy without the tuning element in the cavity. We measured the astigmatism of the output beam of the laser to be less than 2%.

The design of the nozzle for the dye jet is critical to the performance of the laser. Ethylene glycol is used as the solvent because it is extremely viscous fluid and can generate a smoother jet stream. The nozzles are machined out of sapphire, in order to create very smooth surfaces. The nozzles were by the Specialty Shops at Lawerence Berkeley Labs based on the design by Interoptics (see Fig. 6). We used a shim of 300 micron. The circulation system was based on a design by a group at Bell Labs to create a stable, contaminant free, temperature and pressure regulated dye flow. A schematic of the circulation system we built is shown in Fig. 7. The circulation system consisted of a stainless steel, 1 liter reservoir, a single speed motor (Micropump 641), magnetically coupled pump (Micropump 210), a pressure regulator (Cashco) to control the pressure through the jet, a viton bladder precharged to 25 psi with nitrogen (Greer-Olaer) that is used to damp out remaining vibrations from the pump, a filter with 1 micron holes to remove impurities (Balston), a stainless steel pipe that is filled with ball bearings to provide a turbulent path for the dye to pass through to remove bubbles, a pressure gauge (Wika, 0-160 psi), and a ball valve for on-off control to prevent air bubbles during start-up. We found that an operating pressure of 55 psi for the dye jet minimized the broadband noise in the dye laser output (less than 100 kHz). All of the pipe and tube fittings are stainless steel to prevent corrosion. Quarter-inch teflon tubing was used throughout the system. We regulated the temperature of the dye to counteract the heating from the pump pulse by circulating temperature regulated water through a copper pipe that was attached to the stainless steel pipe that contains that ball-bearings. The schematic of the temperature regulator of the cooling water is given in Fig. 8. Wall water was used to regulate the temperature of the bath. The temperature controlled electronics were built in the Electronics Shop (Job #87-128).

We chose Rhodamine 6G as the dye for the gain medium for the laser because it is very stable, has a high conversion efficiency and is tunable from 560 nm to 650 nm. We dissolved the Rhodamine 6G in methanol and then adjusted the concentration to achieve 80-90% absorption of our pump beam.

Tuning of the dye laser wavelength was achieved with a 2-plate birefringent filter[19](Coherent) which has a free spectral range of 80 nm and a bandwidth of approximately 100 GHz. The birefringent filter consists of two plates of birefringent material that is placed in the cavity at Brewster's angle. The optic axis of the material is in the plane of the glass. The light in the dye laser cavity is p-polarized, so it will pass through the first surface of the plate with little loss. Since the birefringent material changes the polarization of the light as it travels through, only light that has the wavelength that corresponds to a 180 degree rotation of the polarization (or some multiple) will not suffer a loss at the second Brewster angle surface. As the plate is rotated, the index of refraction seen by the polarized laser changes and hence the wavelength that suffers the least amount of loss at the second surface will change. In effect, rotating the plate corresponds to selecting which part of the gain spectrum will be above the lasing threshold. The second plate does not change the tuning range, but does narrow the bandwidth that is allowed to lase. We also tried as three-plate filter, but its limitation on the bandwidth (approximately 40 GHz) led to a broadening of our pulse and our experiment did not require that narrow of a bandwidth. A plot of output power and pulsewidth versus lasing wavelength is shown in Fig. 9. Since we did not see a significant drop in power on the red side of the tuning spectrum, we believe that our tuning range is limited by the coating of our optics in the cavity.

Sensitivity of synchronous pumped dye lasers to cavity length mismatch has been investigated extensively.[20, 21, 22] In general, the dye laser cavity is a few microns longer than the pump laser cavity to get the optimal modelocking. We mounted our output coupler on a shop-built translation stage and used an 80 pitch screw for control of the cavity length.

We measured our optical pulses using a home-built spinning-mirror autocorrelator.[23] We observed the following features. For cavities that are too long we saw a coherence spike. For a cavity length that was too short, we saw satellite pulses (See Fig. 10). We operated using the length that corresponded to the pulse in Fig. 10c, which corresponded to an autocorrelation width of 2.9 picoseconds. The signal-to-noise of our autocorrelation limits our ability to fit our autocorrelation uniquiely to a particular pulse shape. If we assume a hyperbolic secant-squared pulse, we have a deconvoltuion factor of $\tau_p/\tau_{AC} = .65$. This leads to a pulsewidth of 1.9 picoseconds. We measured the bandwidth of our laser to be approximately 2 Å. This gives us a time-bandwidth product $\Delta\nu\Delta\tau$ approximately equal to the .3, which is the transform limit of a hperbolic secant-squared pulse.[24]

C. Four-Stage Amplifier

Our experiment required tunable optical pulses of peak powers greater than 10^9 W/cm^2. This corresponds to an amplification of the dye laser by a factor 10^5-10^6. In order to achieve this amount of gain, the design of the dye amplifier was based on a design recently published by Murnane et. al.[25] and modified by Steve Doig and Phil Reed.[26] The details of the design are strongly dictated by our particular scientific needs, limited budgets, and time.

1. Theory

The theoretical issues regarding high gain amplifiers have been studied extensively over the last 15 years.[27] In general, the small signal, unsaturated gain is defined as

$$G_0 = I(z)/I(0) = e^{\Delta N \sigma z} = e^{g_0 z} \qquad (1)$$

where I(z) is the intensity of the signal pulse as a function of position in the gain medium, ΔN is the difference in population densities between the excited state and ground state

populations (molecules/cm^3), σ is the stimulated emission cross-section for the molecules (cm^2), g_o is the small signal gain coefficient, and z is the distance travelled in the gain medium. According to Eq. 1, in the absence of any limiting effects, the gain of a medium should increase exponentially with distance travelled through a medium.

We can estimate the amount of small signal gain available in a system with the following expression:

$$g_o = \Delta N \sigma = \frac{E_p}{h\omega_p} \frac{\tau_{inversion}}{\tau_{pulse}} \eta \frac{\sigma}{(2r)^2 L} \qquad (2)$$

where E_p is the energy per pump pulse, $h\omega_p$ is the energy per photon in the pump beam, $\tau_{inversion}$ is the inversion lifetime of the dye, τ_{pulse} is the pulsewidth of the pump laser, η is the efficiency of the dye, r is the cell radius and L is its length. This expression corresponds to the number of excitations that occur within a pulsewidth, $\left\{ \frac{E_p}{h\omega_p} \frac{\tau_{inversion}}{\tau_{pulse}} \eta \sigma \right\}$, within the pumping volume for a transverse-pumped cell, $\left\{ (2r)^2 L \right\}$. The value of g_o calculated from this expression for each cell is given in Table 1. Since small variations in the value of g_o lead to large variations in the expected gain, this expression has little practical importance but it does give us an idea how the gain of the cell depends on various physical parameters.

There are two effects that limit the amount of gain that can be obtained from an amplifying medium. It can be shown that the population difference ΔN saturates under strong pumping. For CW pumping, this leads to a saturation of the gain coefficent that can be written as

$$g = \frac{g_o}{1 + \frac{2I\sigma\tau}{h\omega}}$$

where g_o is the small signal gain coefficient, $\hbar\omega$ is the energy per photon of the signal pulse, σ is the emission cross-section and τ is the recovery time of the molecule. It is useful to define a quantity called "the saturation intensity", as

$$I_{sat} = \frac{h\omega}{2\sigma\tau}$$

The saturation energy is defined as the intensity at which the gain is reduced to half its value. Since we are pumping with a pulsed source, each molecule can only be pumped once (and then it is removed from the active region) so the recovery time has no real meaning. Hence, we speak of *saturation fluences* instead of saturation intensities. The saturation fluence corresponds to energy required to de-excite one molecule located within the cross-sectional area. This can be written simply as[27]

$$U_{sat} = \frac{h\omega}{2\sigma} \qquad (3)$$

For Rhodamine 6G, this saturation fluence is approximately 1 mJ/cm^2. When the input pulse fluence approaches the value of the saturation fluence, the pulse will experience linear gain instead of the exponential gain of Eq. 1. Though the gain for the cell is lower, the amount of energy exrtracted from the medium will increase (see Fig. 11 for an example). The advantage of operating in the saturation regime is that the output beam fluctuations will be proportional to the input beam fluctuations instead of being amplified exponentially. The last stage is usually operating well into the saturation regime in order to achieve this pulse stability.

The other phenomenon that limits the small signal gain of a laser amplifier is amplified spontaneous emission (ASE). Once the pump pulse establishes an excited state population, it is possible for some of the molecules to relax through spontaneous emssion.

A spontaneously emitted photon can then propagate down the medium and compete with the signal pulse for gain. The amount of gain experienced by the spontaneously emitted photon will be influenced by the geometry of the amplifying medium. A long, narrow medium will have less ASE then a short fat medium since it subtends a smaller solid angle into which the ASE can radiate. If we assume a rectangular medium of radius r and length L, the amount of gain that a spontaneously emitted photon will see by the time it reaches the end of the medium (ignoring saturation effects) is given by,

$$G_{max} = \frac{4\pi L^2}{r^2} \frac{\tau_{spont}}{\tau_2} \qquad (4)$$

where L and r are the cell length and radius respectively, τ_{spont} is the spontaneous lifetime, and τ_2 is the fluroescence lifetime. This expression gives us a practical limit on the amount of gain we can see from a cell; any additional pumping of the system will mostly go into amplifying the spontaneously emitted photons. Since the dyes we use are quite efficient, we can approximate the ratio of the relaxtion times as one. This implies that the maximum amount of gain that can be obtained from an amplifier is determined by its geometry and is independent of pumping parameters. Note, ASE does not effect the amount of energy which can be extracted from the medium. As discussed above, this is determined by how well the amplfying medium is saturated.

2. Construction

Given our scientific requirement of 1 millejoules per pulse, Eq. 3 implies we need a cell approximately 1 cm in radius. Given the output of our dye laser, 100 microjoules requires a gain of 10^5. To obtain a gain of this magnitude, Eq. 4 says we need a cell at least 4 meters long. To avoid his practical impossibility, we break up the amplification process into multiple stages. The first cells will be designed for high gain, but can have

small radii since they do not have to support that much energy. The later cells will have larger radii to sustain more energy, but will have lower gain. It is also practically helpful to operate the later stages well into the saturation regime to maintain pulse stability. In addition to these considerations, we need to isolate the individual gain stages to suppress unwanted ASE so it does not propagate from one stage to the next, and compete with the laser pulse for stored energy. This requires the use of saturable absorbers, which put an additional requirement on the energy generated in a given stage and limits the overall gain of the system.

In addition to these theoretical constraints, there are many practical constraints that act as guidelines for the construction of a multi-stage amplifier. The following is a description of the 4-stage amplifier built by Chris Mullin and me. For each part of the amplifier, I will motivate the decisions we made by elucidating these contraints.

A schematic of the amplifier is given in Fig. 12. The amplifier consists of four stages of amplification. The dye cells used are transverse-pumped Bethune cells. They are constructed from 90-degree prisms with a hole bored lengthwise near the right angle of the prism. The hole is positioned so that it is possible to illuminate the dye which passes through the channel from all fours sides (see Fig. 13). This design allows a uniform illumination even for a spatially inhomogeneous pump beam, and enhances the pump beam alignment stability. The prisms used were surplus prisms from army tanks and were drilled to the proper bore size with diamond tipped drill bits. The endplates for the cells were designed to allow dye flow through the cell with a minimum amount of turbulence while allowing optical access for the dye laser beam that was to be amplified. The windows used were "punched" from 3/8" glass slab and AR-coated for less than .1% reflection loss. Each cell had an independent circulation system for the dye (Fig. 14), except for cells 2 and 3 which shared one system. The circulation system consisted of a stainless steel reservoir, a self-priming pump with variable speed motors (Micropump), a

ball valve, an in-line filter (Balston), and a flow meter. The dyes were cooled by circulating wall water through coils immersed in the dye reservoirs.

Our four stages have the following bore sizes: 1mm x 2.5 cm, 2.5 mm x 6 cm, 2.5 cm x 6 cm., 6 mm x 8 cm. The size of the first cell was determined by the radius of the smallest diamond-tipped drill available at the LBL glass shop and its length was determined by the length of the drill bit. We used a Melles-Griot, 1", 90° prism, AR-cotated for 532 nm for the first cell. The size of the remaining cells is based on the design of the amplifer by the Mathis group. Using Eq. 4, these cell geometries lead to maximum practical gains listed in Table 1.

In order to effectively extract the energy from the dye medium, it is helpful to have a beam fill 80-90% of the bore of the dye cell. If the gaussian output of the dye laser were passed directly through a cell, the energy would not be evenly distributed across the bore. Instead, we uniformly illuminate a pinhole to give us a near flat-top beam, and then image the pinhole into each individual gain stage using a relay imaging technique (see Fig. 15). This technique limits losses due to diffraction and more efficiently fills the aperture. We used a 600 micron pinhole, which corresponded to transmitting 30% of our pulse intensity. A schematic of the image relay system is shown in Fig. 16.

The optics used to couple the pump energy into the Bethune cells are shown in Fig. 16. We used thin glass windows and microscope slides to couple approximately 12% of the beam for each of the first three stages with the remaining energy going to the final stage. We used the Quantel laser (Model YG580) to pump the dye amplifiers. This laser has the maximum pulse stability and the minimum timing jitter when it was run at near maximum output, which gave us a total available energy at 532 nm of 360 mJ/pulse. This is approximately twice as much energy as we need to pump a single amplifier chain. Since over-pumping the cell leads only to additional ASE, we restricted the amount of power incident on each stage by placing a glass slide in the beam path and controlling the amount of energy transmitted by varying the angle of incidence upon the slide. We used at most

three optics per amplifier stage to couple the pump energy in as efficiently as possible: two cylindrical lens were used as a telescope to give us the correct aspect ratio and a diverging lens to enlarge the beam so it illuminated the bored hole and its three images. Since the position of the bores were not perfect, there were gaps between the images, leading to less effective coupling of the pump beam. This was most significant for stages 2 and 3, since there was a loss of approximately 25% due to bad positioning of the bore hole.

The dyes chosen in each stage are strongly dependent on the wavelength range over which you want to amplify. Although our dye laser tuning range goes from 565 nm to 620 nm, the range of tunability of an amplified pulse is only about 10 nm for a given set of dyes. We chose to amplify around the region centered on 595 nm, based on the design of the Mathis group. In the first cell, it is common practice to use a dye that has a fluorescence peak that is shifted from the wavelength at which you want to amplify so the ASE generated in the cell will not compete with the amplifed pulse for gain in the second cell. This will limit the gain you can expect from the cell, since you will not be operating at the peak of the emission cross-section. The other cells, you want to use dyes that give you maximum gain with minimum absorption at the wavelength you want to amplify. Kiton Red is used in the fourth stage because its emission peak is slightly shifted from Rhodamine 610, thus providing less gain for the ASE generated in previous stages.

We used the following dye combination: Stage 1 - Rhodamine 590 (Rhodamine 6G), Stage 2 and 3 - Rhodamine 610 (Rhodamine B), Stage 4 - Kiton Red. The dye concentrations are chosen so that

$$\text{Absorption} = 10^{-\alpha r} = \frac{1}{2}$$

where α is the absorption coefficient at 532 nm and r is the bore radius. This condition ensures uniform pumping. (Note, we use base 10 because that is how the absorption

coefficient, α for the dyes are usually quoted). The concentrations we used are listed in Table 1.

Although ASE is generated by a spontaneous process, it can leave the cell fairly collimated. To prevent the propagation of ASE from one cell to the next, it is important to isolate each of the stages. Between Stage 1 and Stage 2, we used a pinhole, to spatially separate the divergent ASE from the dye pulse. Since the fluoresence peak is shifted from the dye laser wavelength, we found that by using a Corning Color Filter #237, we were able to pass more than 90% of the amplifed beam and transmit less than 10% of the ASE. We also found most of the ASE generated in the first stage (which is peaked at 560 nm for Rh 6G) was absorbed by the Rh 610 in the second cell, so we eventually removed the color filter from the set-up. Between Stage 2 and Stage 3, and between Stage 3 and Stage 4, we made use of the differing temporal properties of ASE (approximately 5 nanoseconds) and the amplified dye pulse (2 picoseconds) by using a saturable absorber to suppress ASE. In choosing a saturable absorber, it is important to choose a dye with a recovery time longer than the amplified dye pulse, but much shorter than the ASE pulse. This way, the leading edge of the amplified pulse can bleach the absorber, while the ASE will be absorbed. It is important for the dye to have a quick recovery time, so the ASE *after* the dye pulse will also be absorbed.

We used crystal violet as our saturable absorber. It has a quick recovery time (on the order of 2 picoseconds). After two stages of amplification, we have a pulse energy of approximately 200 nJ. We used the following expression to estimate the concetration we needed to saturate the absorber medium

$$E_{sat} = A\,L\,N\,h\omega$$

Namely that the energy required to saturate the medium is equal to the total number of absorber molecules times the energy per excitation. Since we know what pulse energy we have, we can use this expression to approximate the concentration.

Since bleaching of the absorbers requires high intensities, we dissolved the crystal violet in ethylene glycol and flowed it through open jets. The jets were borrowed from Roger Falcone's group. They were both 300 microns thick. The circulation systems for the saturable absorbers were identical to those for the Bethune cells.

We used a divider circuit (Spectra-Physics SM-1) to control the timing betwen the dye pulse and the pump pulse. The circuit used the input from the rf source to the modelocker of the YLF and controlled the firing of the Q-switch. We also adjusted the timing between the dye pulse and the pump pulse by adjusting the delay. The jitter was then determined by the output of the Quantel, corresponding to 500 picoseconds.

The output from the amplifier we used for the experiment was 600-800 μJ/pulse, with less than 5% ASE. To obtain this, we optimized the amplifier stage by stage. For each stage, we optimized the gain/ASE ratio by adjusting the pump power into each cell , the concentration in the cells and in the saturable absorber jets, and the timing. The optimized performance characteristics for each cell are summarized in Table 1. A plot of output energy vs. wavelength is given in Fig. 17. An autocrrelation of the amplified laser pulse is given in Figure 18.

References

[1]T. M. Pollak, W. F. Wing, R. J. Grasso, E. P. Chicklis, H. P. Jenssen, IEEE J. Quantum Elect. **QE-18**, 159 (1982).

[2]H. Vanherzeele, Appl. Opt. **28**, 4042 (1989).

[3]H. Vanherzeele, Rev. Sci. Instrum. **60**, 59 (1989).

[4]A. M. J. Johnson, W. M. Simpson, Opt. Lett. **8**, 554 (1983).

[5]H. Hade, H. Burggraf, Opt. Comm. **38**, 1981 (1981).

[6]H. Vanherzeele, Appl. Opt. **27**, 3608 (1988).

[7]T. Moses, *et al.*, Rev. Sci. Instrum. **submitted**, (1991).

[8]J. Q. Yao, T. S. Fahlen, J. of Appl. Phys. **55**, 65 (1984).

[9]J. D. Bierlein, H. Vanherzeele, J. Opt. Soc. A. B. **6**, 622 (1989).

[10]R. F. Belt, G. Gashurov, Y. S. Liu, **October**, (1985).

[11]F. Ahmed, Appl. Opt. **28**, 119 (1989).

[12]M. G. Roelofs, J. Appl. Phys. **65**, 4976 (1989).

[13]F. P. Shafer, *Dye Lasers* (Springer-Verlag, Berlin, 1977).

[14]C. V. Shank, Rev. Mod. Phys. **47**, 649 (1975).

[15]J. D. Simon, Rev. Sci. Instrum. **60**, 3597 (1989).

[16]B. H. Soffer, J. W. Linn, J. Appl. Phys. **39**, 5859 (1968).

[17]P. K. Runge, R. Rosenberg, IEEE J. Quant. Electr. **8**, 910 (1972).

[18]H. W. Kogelneck, E. P. Ippen, A. Dienes, C. V. Skank, IEEE J. Quant. Elect. **QE-8**, 373 (1972).

[19]A. L. Bloom, J. Opt. Soc. Am. **64**, 447 (1974).

[20]J. M. Catherall, G. H. C. New, P. M. Radmore, Opt. Lett. **7**, 319 (1982).

[21]D. M. Kim, J. Kuhl, R. Lambrich, D. v. d. Linde, Opt. Comm. **27**, 123 (1978).

[22]J. Herrmann, U. Motschmann, Appl. Phys. B **27**, 27 (1982).

[23]Z. A. Yasa, N. M. Amer, Opt. Comm. **36**, 406 (1981).

[24]K. L. Sala, G. A. Kenney-Wallace, G. E. Hall, IEEE J. Quant. Elect. **QE-16**, 990 (1980).

[25]M. M. Murnane, R. W. Falcone, J. Opt. Soc. Amer. B **5**, 1573 (1988).

[26]S. J. Doig, (University of California, Berkeley, 1991),

[27]A. E. Siegman, *Lasers* (University Science Books, Mill Valley, California, 1986).

Table 1: Physical parameters for amplifier chain

Cell	one	two	three	four
dimensions	1× 25.4	2.5× 50	2.5× 50	6× 80
dye	Rh 6G	Rh B	Rh B	KR
N	3×10^{16}	1.6×10^{16}	same	1×10^{16}
E_p	25 mJ	38 mJ	35 mJ	200 mJ
σ_{abs}(532 nm)	10^5	5×10^4	same	3.5×10^4
σ_{emis}(595 nm)	5×10^{-19}	10^{-16}	same	10^{16}
g_{max}	3.2×10^4	2×10^4	same	10^4
$G_{measured}$	100	550 (450)	60 (8)	50
U	3 nJ	1.6 μJ (1.4 μJ)	20μJ (12 μJ)	600 μJ
ASE	2.5%	<1%	10%	15%

dimensions: mm
dye: Rh6G - Rhodamine 590, Rh B - Rhodamine 610, KR - Kiton Red
N: concentration (molecules/cm^3)
E_p: pump laser energy incidenct on cell (mJ)
α: absorption coefficient for dyes as defined in Eq. 5 (L/mol-cm)
σ: emssion and absorption cross-sections for dyes (cm^2)
g_{max}: Maximum gain allowed as determined by ASE
$G_{measured}$: The value of U_{out}/U_{in} measured for each cell.
U: energy of amplified pulse. Value in parenthesis is with saturable absorber.
ASE: Amplified spontaneous emission for each cell as a percentage of energy produced. Value in parenthesis is with saturable absorber

Figure Captions

Figure 1: Schematic of Nd:YLF laser cavity configuration. The numbers under the elements indicate the position of the optical element in the cavity as measured from the output coupler. The beam waist is a result of an ABCD calculation for the cavity as s performed on PARAXIA. The calculation did not include the cylindrical lens or the astigmatic thermal focussing of the rod.

Figure 2: Autocorrelation of 1.053 micron output of Nd:YLF laser. Assuming a gaussian pulse shape, this corresponds to a 55 picosecond pulsewidth at FWHM.

Figure 3: SHG unit. a) Schematic of optics used in SHG unit. Input and output lens are f= 5 cm. b) Details of temperature controlled mount for KTP crystal. See text for description.

Figure 4: Pulse-shortening due to Synchronous Pumping of a dye laser. The 35 picosecond pump pulse brings the gain medium above threshold (small signal gain curve). The dye pulse arrives soon after the medium goes above threshold to deplete the population through stimulated emission, resulting in a shortened dye pulse.

Figure 5: Cavity configuration for synchronously pumped dye laser.

Figure 6: Exploded drawing of the sapphire nozzle construction. The channel is formed by the inner pieces C, C', together with the glass shim used as spacers D, D', wrapped in teflon tape E, E'. The holders A,B and the endplates are machined from stainless steel. (Drawing from Interoptics)

Figure 7: Flow schematic of circulation system for dye laser. See text for description of details.

Figure 8: Flow schematic for temperature controlled system for dye laser. See text for description of details.

Figure 9: Dye laser output power and pulsewidth vs. wavelength.

Figure 10: Dye laser pulse shape dependence on cavity length. a) Corresponds to a cavity that is too short. b) corresponds to a cavity that is too long c) Corresponds to the operating length. Assuming a hyperbolic secant pulse shape, this corresponds to a pulsewidth of approximately 2 picoseconds.

Figure 11: Pulse output energy versus the pulse input energy for a saturable amplifier with a small signal gain $G_0 = 1000$. (Drawing from Siegman, Fig. 10.5)

Figure 12: Schematic of dye laser amplifier including all the important components, such as mirrors, beam splitters, dye cells, pinholes, and saturable absorbers. The drawing is not to scale. (Drawing done by Subo Ko)

Figure 13: a) Diagram of an ideal Bethune cell showing the four distinct and tangent images of the bored hole; b) Diagram of an actual Bethune cell showing the effect of drilling the hole further from the edge of the prism than required to get tangent images. The presence of the gaps between images leads to a lower pumping efficiency; c) Diagram of a Bethune assembly showing the method used to seal the dye cell with the end plates. The wing nuts are tightened until no leaks are detected between the cell and endplate (or until the prism breaks). (Drawing done by Subo Ko)

Figure 14: Schematic of the dye circulation system and cooling system for the Bethune cells. Cells 2 and 3 share a circulation system. Each circulation system consists of a variable speed pump, flow meter, ball valve and stainless steel reservoir. Cooling water is run through all of the reservoirs in series to maintain temperature stability. (Drawing done by Subo Ko).

Figure 15: Diagram of relevant dimensions of the imaging relay lens pair. the location of the object is at d1 and the location of the image is at d2. The magnification of the image is given by
$m = \frac{f2}{f1}$. (Drawing done by Subo Ko).

Figure 16: Diagram showing the positions of components and lens specification for image relay and pump beam optics. All focal lengths and distances are given in centimeters. Unspecified dimensions are not critical. (Drawing done by Subo Ko).

Figure 17: Amplified dye laser pulse energy vs. wavelength

Figure 18: Autocorrelation of amplified dye laser pulse. Second small pulse is due to an autocorrelation with a second reflection from the beam splitter.

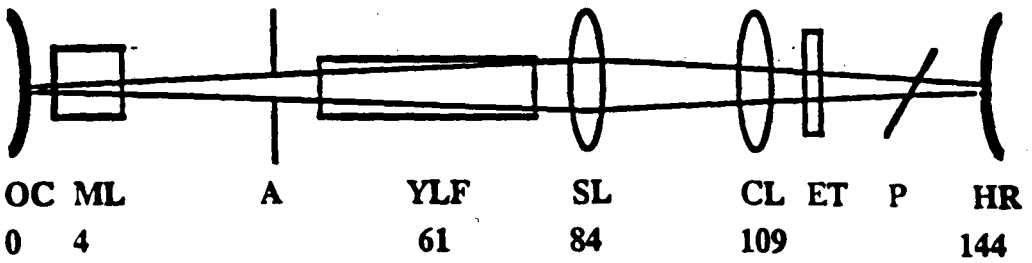

OC: output coupler, f=-120 cm, T= 12%
ML: acousto-optic modelocker , 50 MHz, Quantronix Model 352
A: Aperture, .78 mm
YLF: 4x104 mm Nd:YLF crystal
SL: spherical lens, f=35 cm
CL: cylindrical lens, f=108 cm
ET: etalon, 250 micron thick
P: polarizer shutter unit
HR: high reflector, f= -120 cm

Figure 1

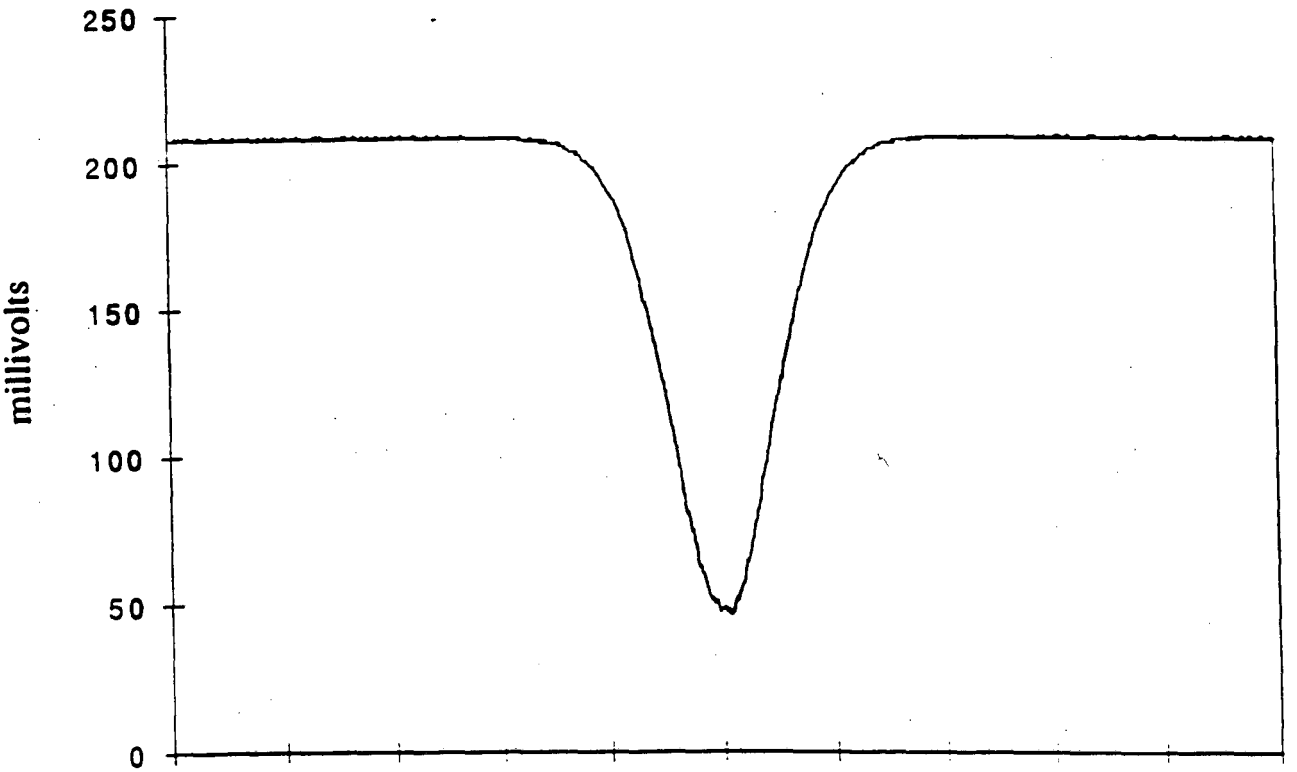

Figure 2

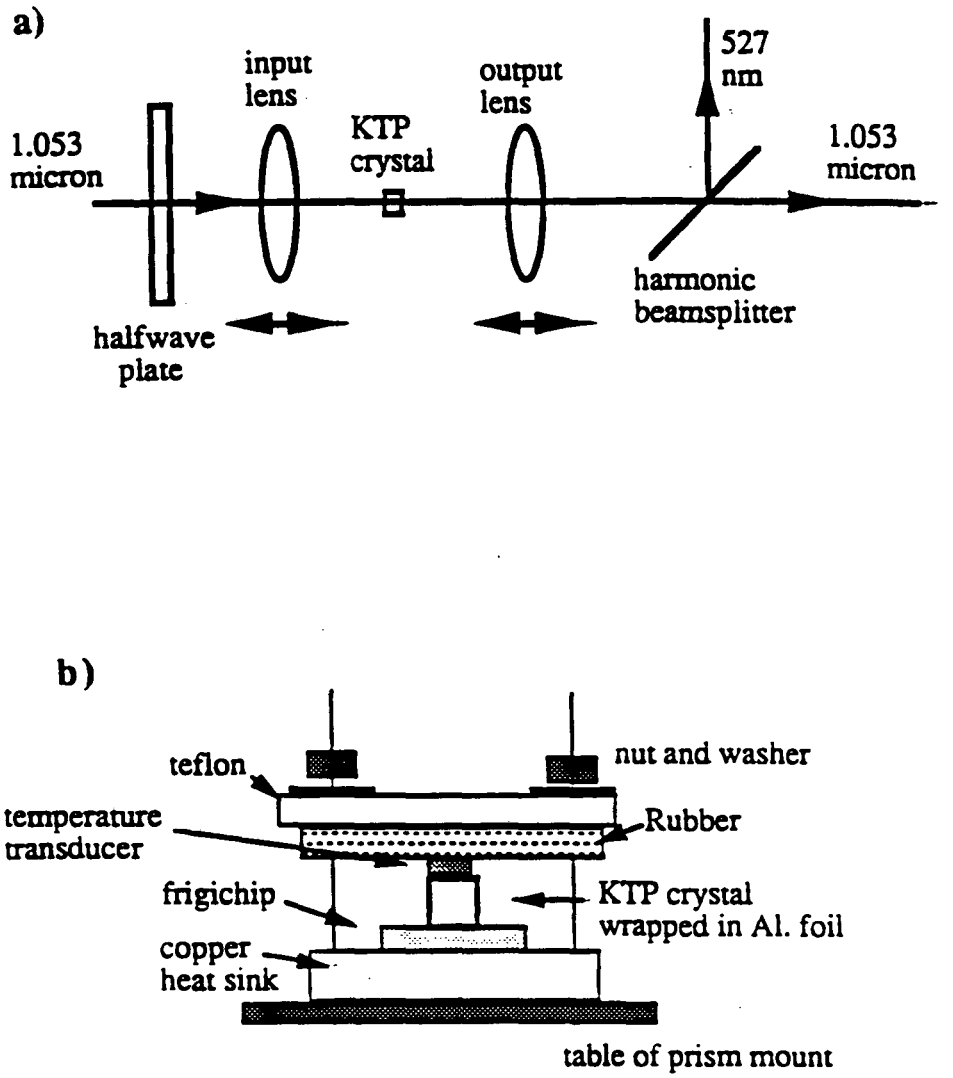
a)
input lens
output lens
527 nm
KTP crystal
1.053 micron
1.053 micron
harmonic beamsplitter
halfwave plate
b)
teflon
nut and washer
temperature transducer
Rubber
frigichip
KTP crystal wrapped in Al. foil
copper heat sink
table of prism mount

Figure 3

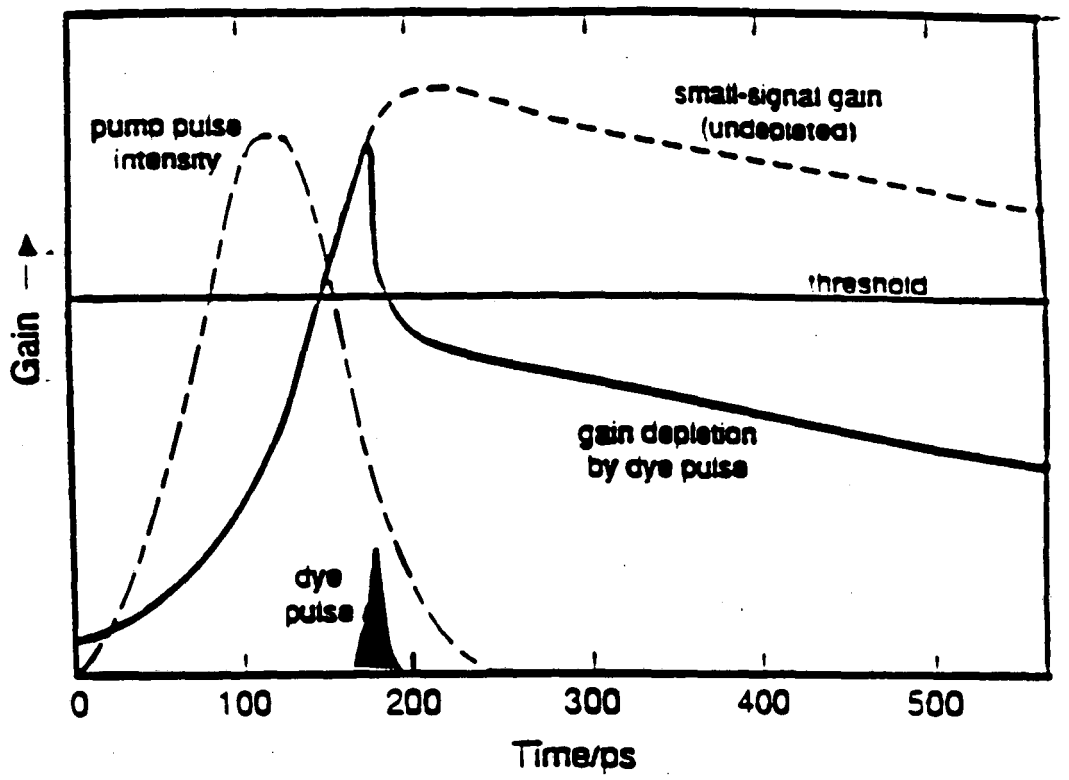
pump pulse
intensity
small-signal gain
(undepleted)
threshold
Gain
gain depletion
by dye pulse
dye
pulse
0
100
200
300
400
500
Time/ps

Figure 4

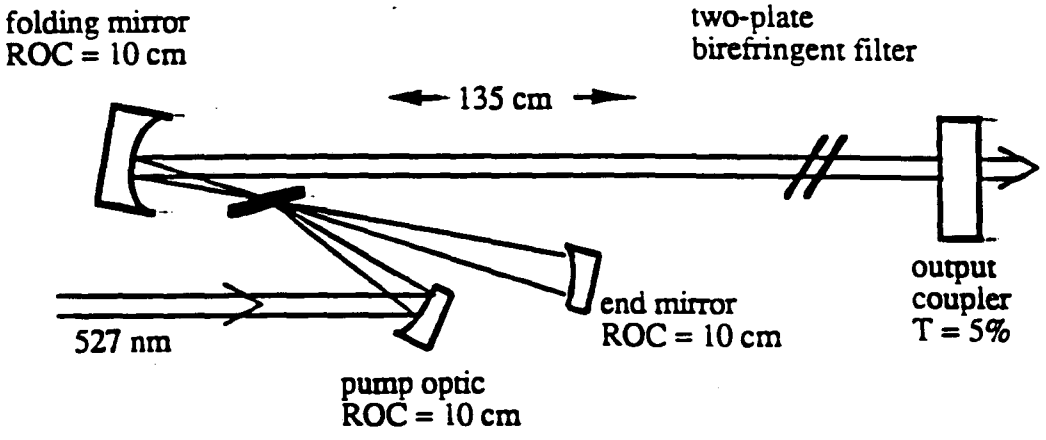
folding mirror
ROC = 10 cm
two-plate
birefringent filter
135 cm
output
coupler
T = 5%
end mirror
ROC = 10 cm
527 nm
pump optic
ROC = 10 cm

Figure 5

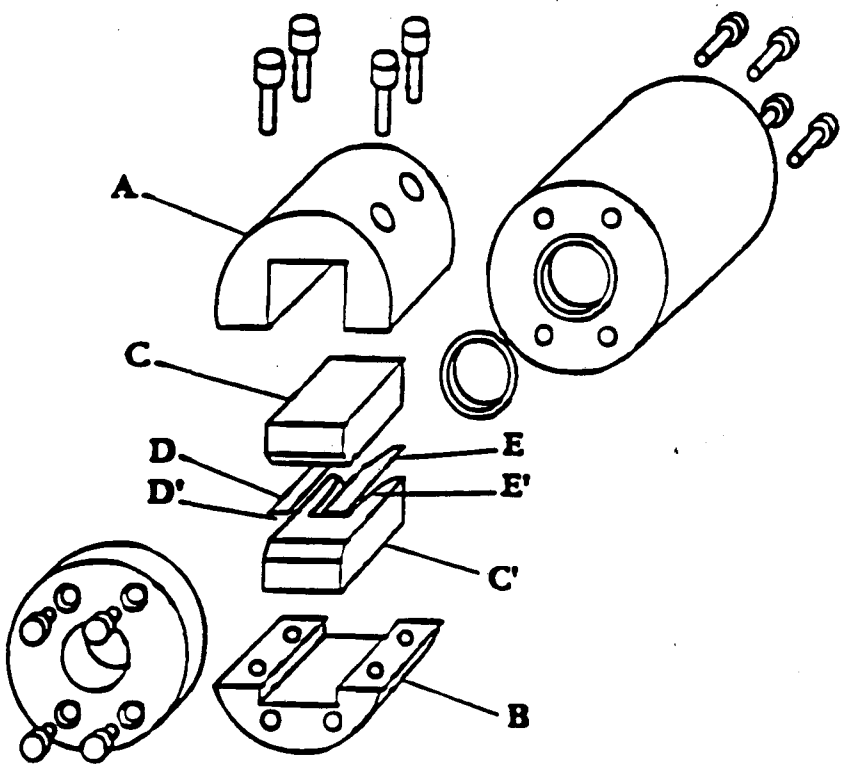

Figure 6

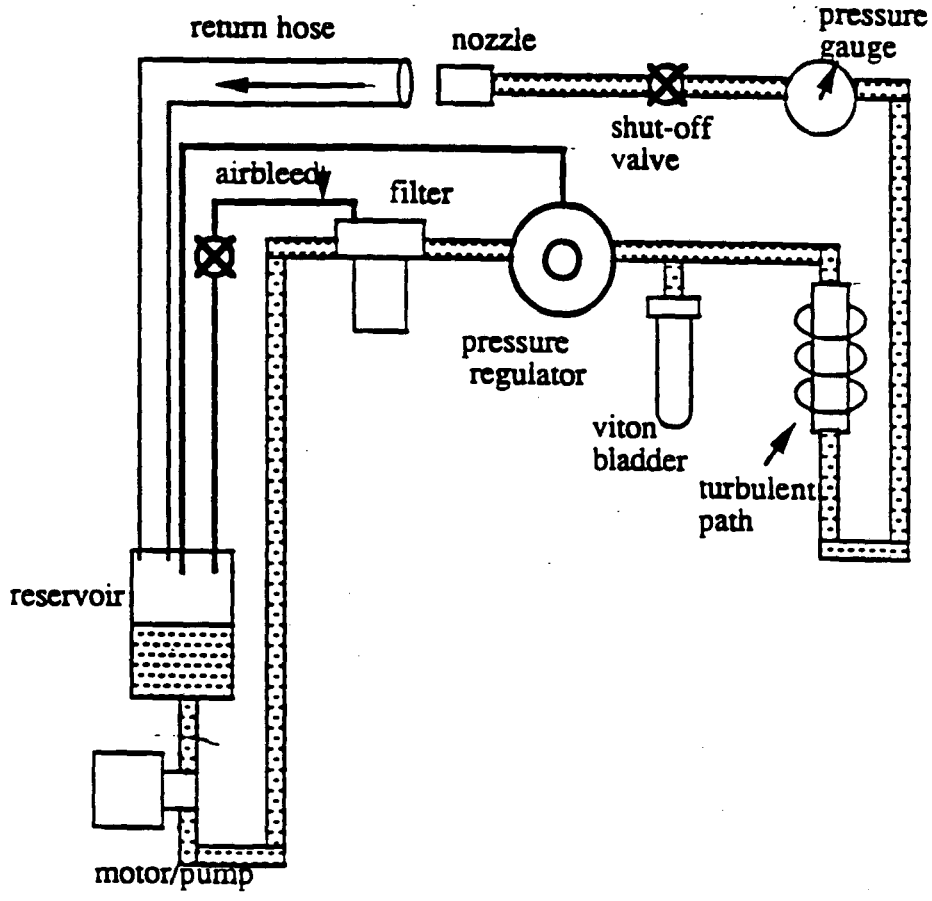
return hose
nozzle
pressure gauge
shut-off valve
airbleed
filter
pressure regulator
viton bladder
turbulent path
reservoir
motor/pump

Figure 7

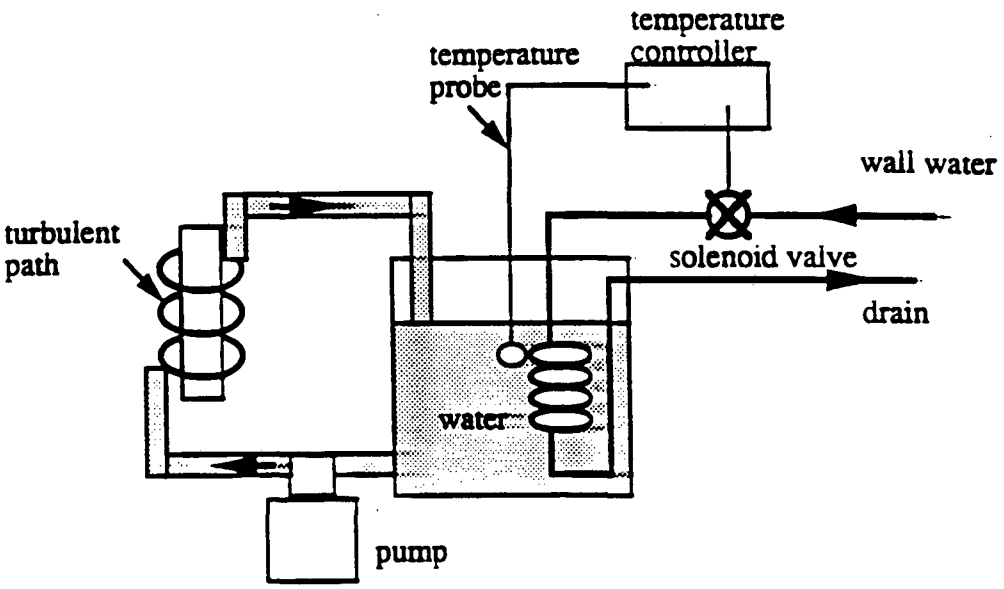
temperature
controller
temperature
probe
wall water
turbulent
path
solenoid valve
drain
water
pump

Figure 8

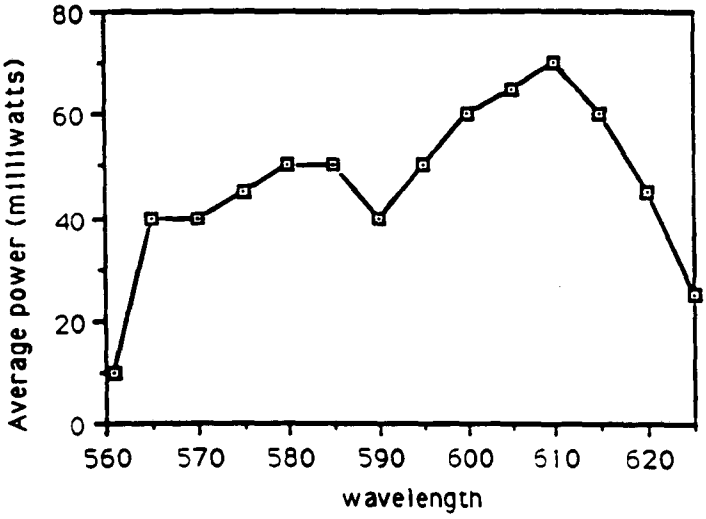
80
60
40
20
0
Average power (milliwatts)
560
570
580
590
600
610
620
wavelength

Figure 9

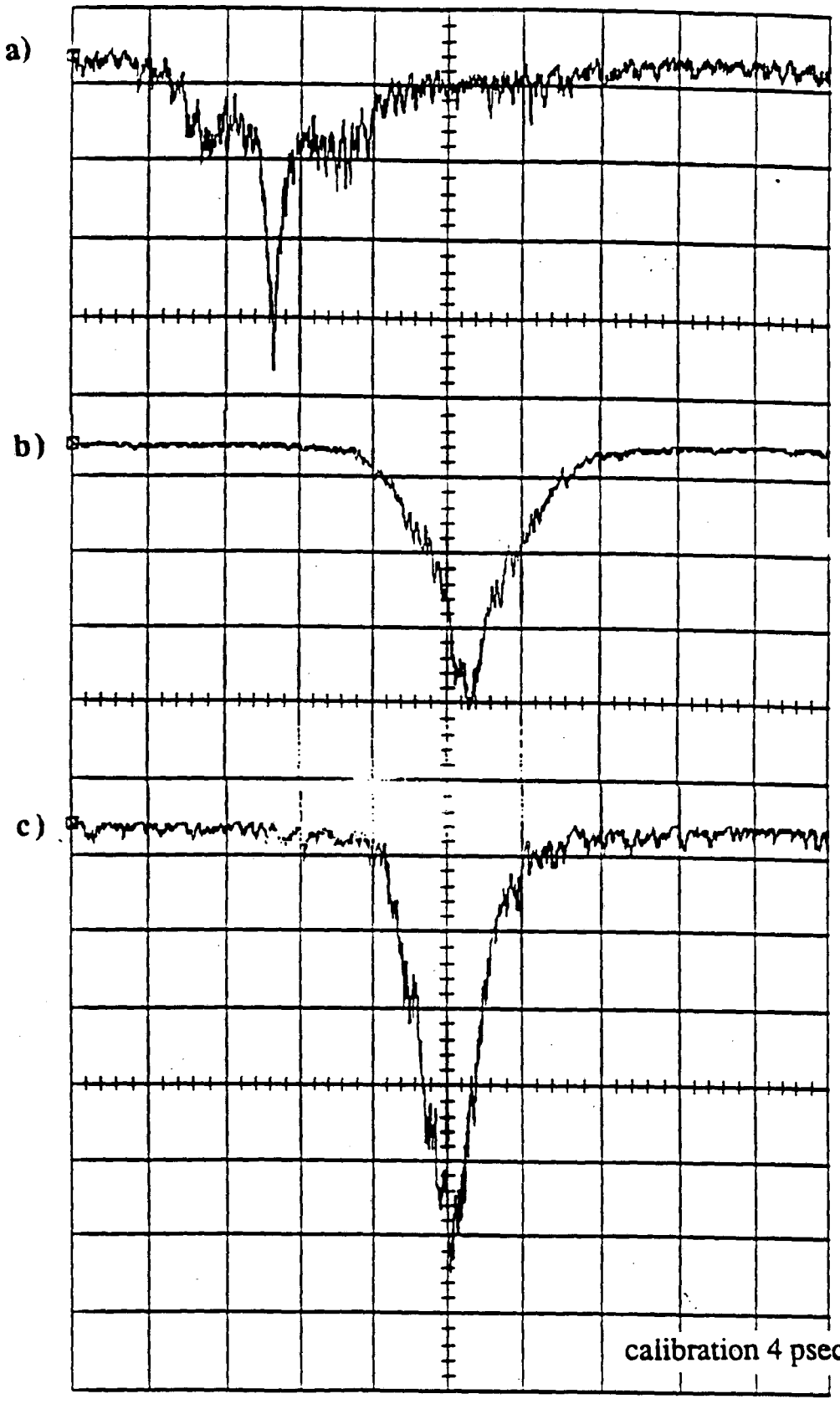

Figure 10

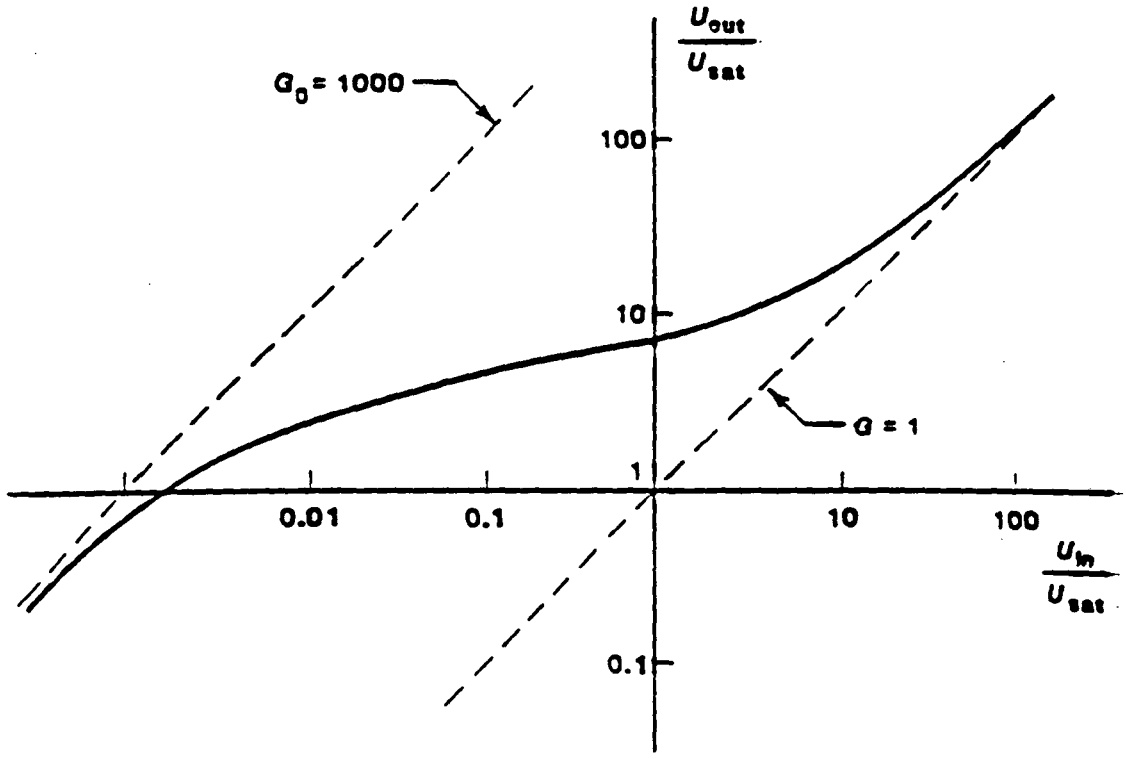

Figure 11

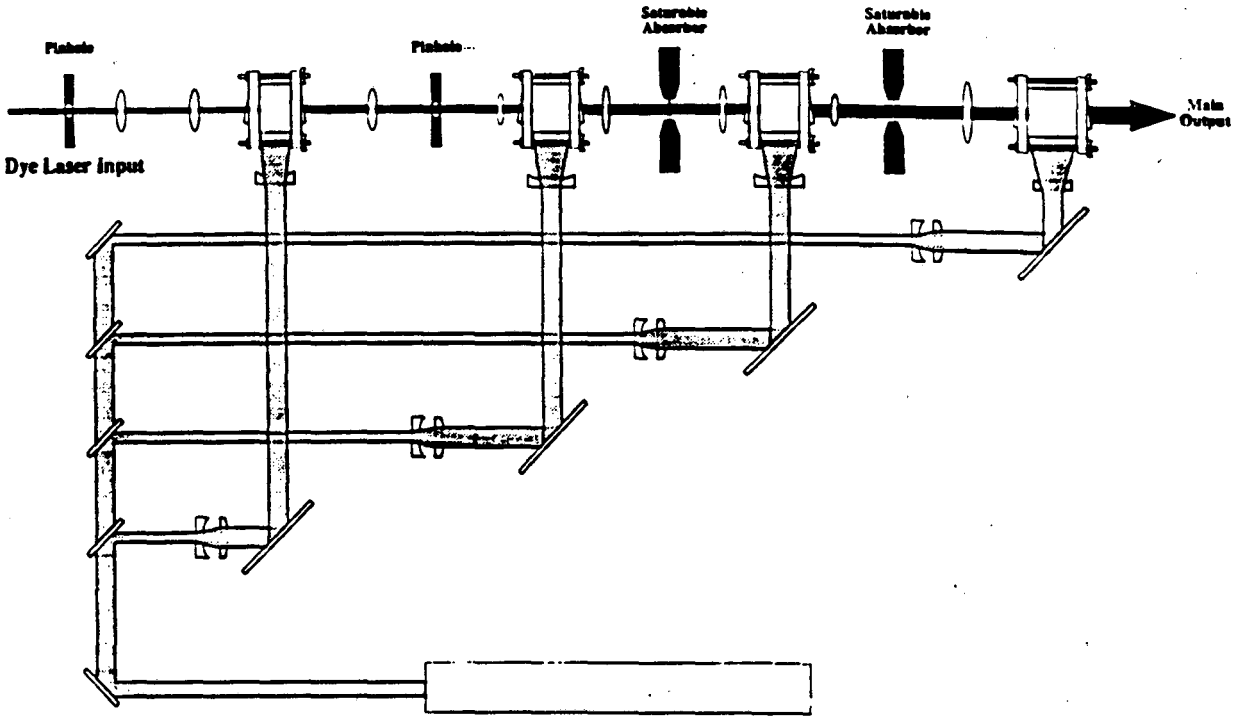
Pinhole
Pinhole
Saturable Absorber
Saturable Absorber
Main Output
Dye Laser Input

Figure 12

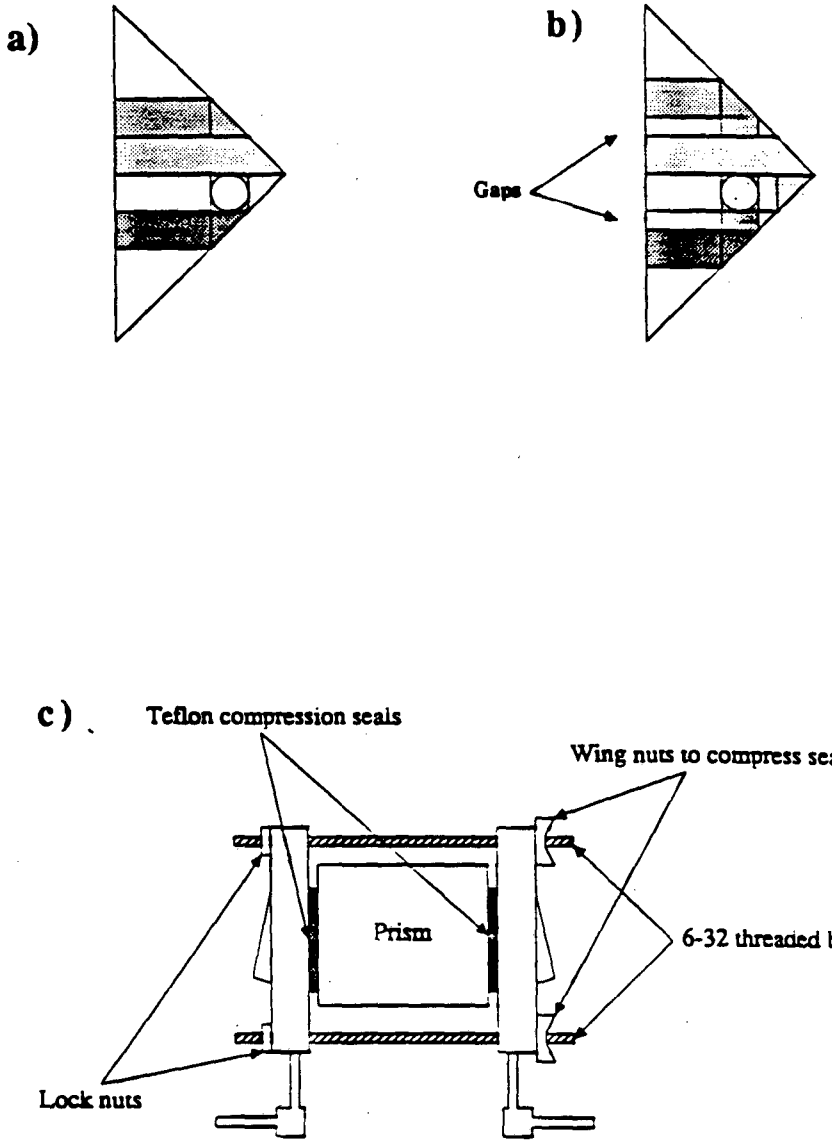
a)
b)
Gaps
c)
Teflon compression seals
Wing nuts to compress seals
Prism
6-32 threaded bar stock
Lock nuts

Figure 13

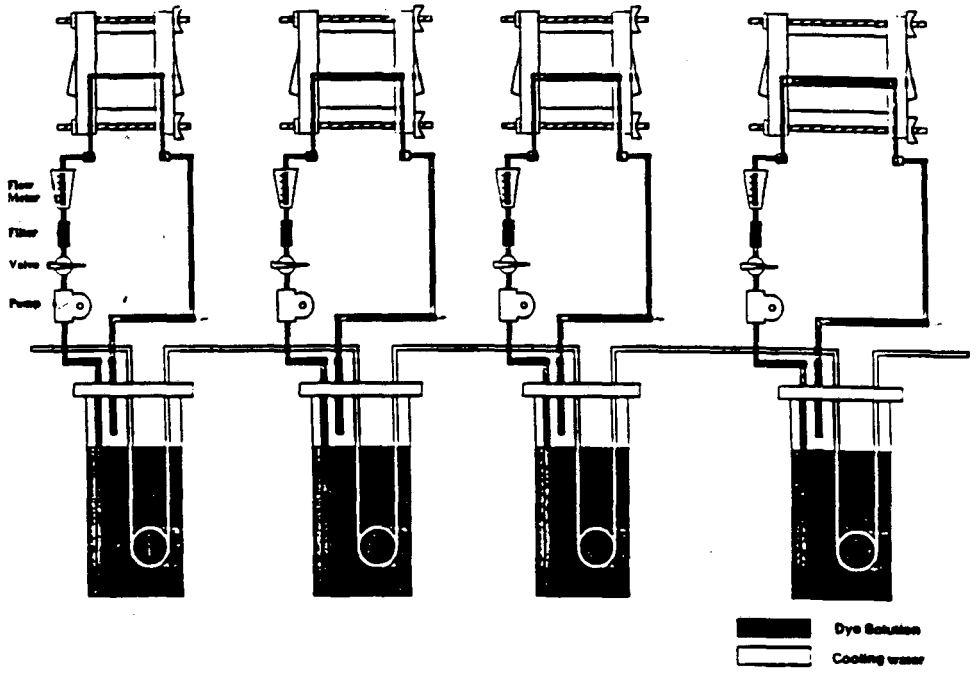

Figure 14

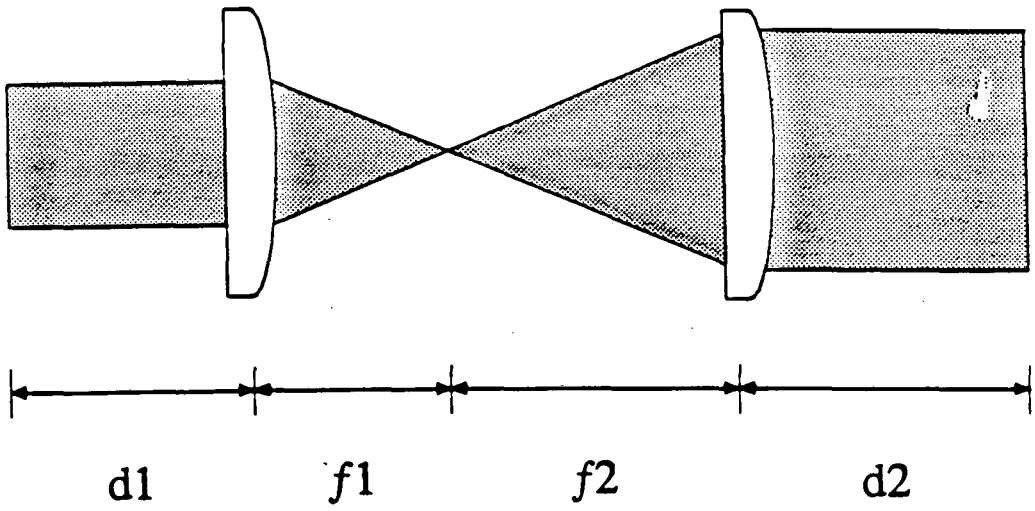

Figure 15

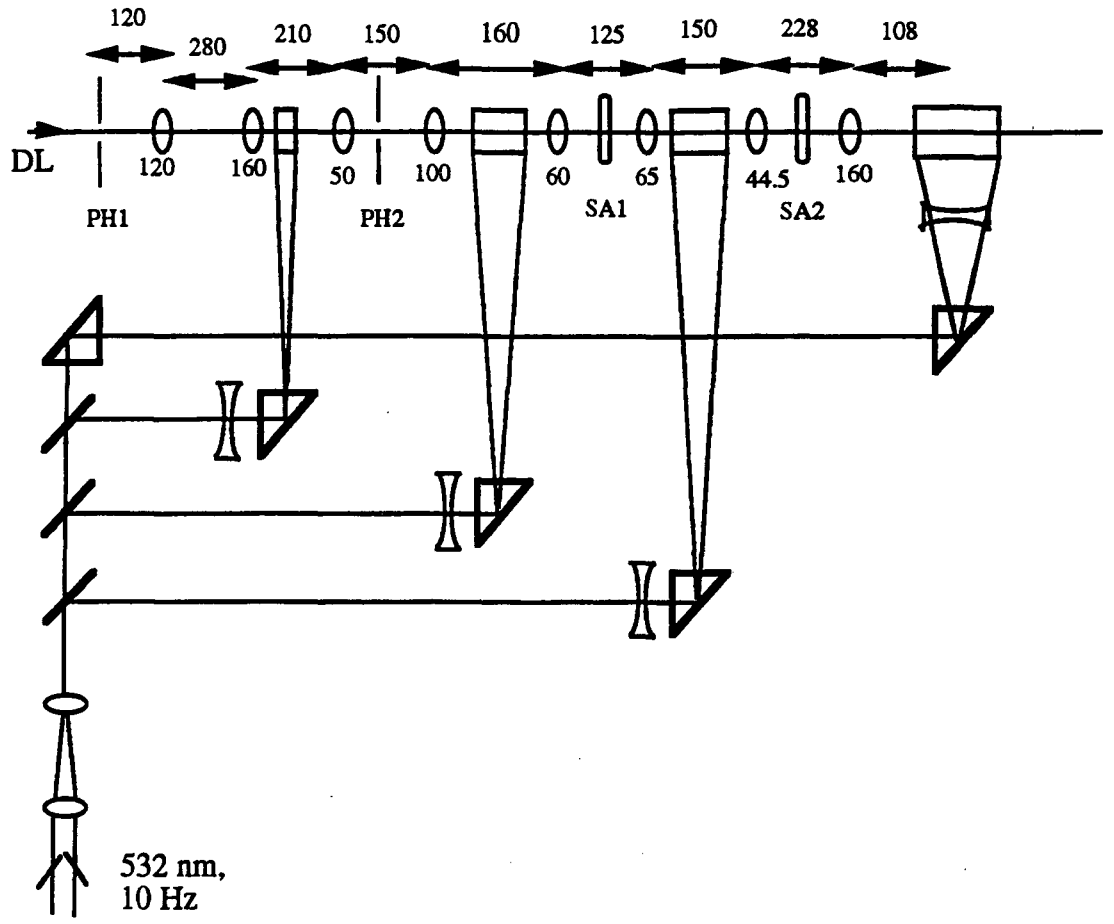

PH1: 600 micron diameter pinhole
PH2: 400 micron diameter pinhole
SA1: first saturable absorber jet
SA2: second saturable absorber jet
DL: dye laser output

Figure 16

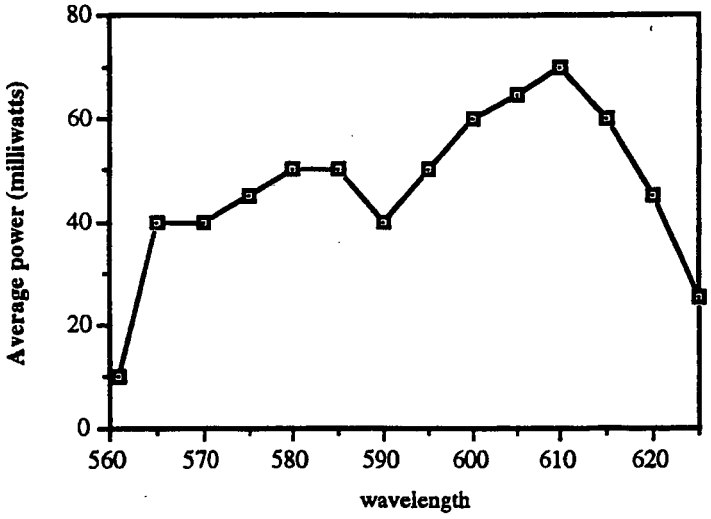
Average power (milliwatts)
80
60
40
20
0
560
570
580
590
600
610
620
wavelength

Figure 17

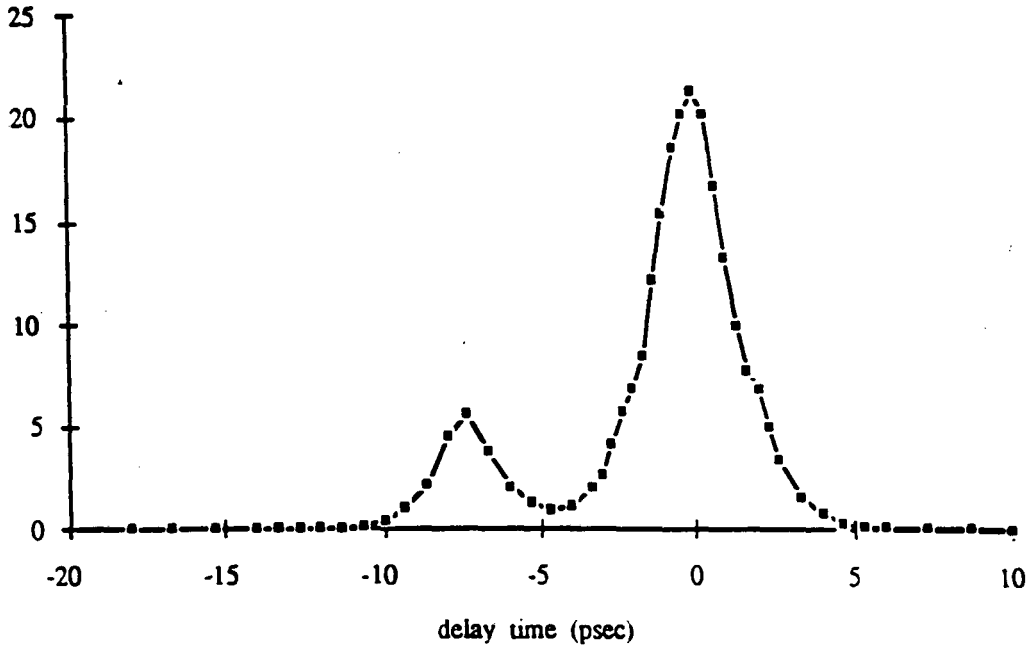

Figure 18

VII. Second Harmonic Generation in Potassium Vapor

A. Introduction

Second harmonic photons have been generated in several different metal vapors, the most thoroughly studied being sodium[1-6] and potassium[7-11]. Generating SH photons coherently in vapor is forbidden by symmetry on both a microscopic level because the individual atoms in the vapor do not possess a dipole, and on a macroscopic level because the atoms are isotropically distributed.[12] For all the vapors studied, the generation of second harmonic photons has been resonantly enhanced near two-photon transitions allowed by symmetry (s-d and s-s) and two-photon transitions not-allowed by symmetry (s-p levels).

Several explanations for this phenomenon have been presented. The most successful explanation thus far is based on a model proposed by Mossberg et. al.[13] to describe harmonic generation in Tl and later modified to accommodate other results.[14, 15] The belief is that free electrons created by a laser-induced multiphoton process are spatially separated from the heavier ions by either the pondermotive potential of the laser or the kinetic energy from ionization. The resulting microscopic charge separation creates a radial DC field. There are then two equivalent explanations for SHG: either the DC field breaks the isotropic symmetry locally and the second harmonic is generated from a $\chi^{(2)}$ process, or the DC field mixes with the incident field in a $\chi^{(3)}$–process, which is allowed by symmetry in an isotropic medium.[15] The time required to establish a DC field is estimated to be on the order of 1-200 picoseconds, depending on the laser intensity and pulsewidth and the density of the gas. A different model, introduced by Dinev, et. al.[1, 7, 16], claims that collisions lead to a mixing of angular momentum states that lead to a breaking of the microscopic symmetry of vapor molecules.

There are several experimental checks that can be done to test the validity of these models, including careful spectroscopic studies of the conversion efficiency as a function

of incident laser intensity and polarization, beam profile, and gas pressure. Most of the measurements have been conducted with nanosecond lasers in the frequency domain. Several investigations have been conducted on potassium. The low n-states were investigated by Lu et. al. [9, 10] They measured the conversion efficiency of SHG for the s,p and d states between n = 3 to 9 as a function of input intensity and vapor pressure. To test the validity of the DC-field model, they did simultaneous measurements of the ionization current. They found that two-photon transitions which generated higher ionization current had lower conversion efficiency into the second harmonic. They claim that although higher ionization current corresponds to a larger DC field, it also depletes the population of the ground state, leading to an overall decrease in the conversion efficiency of the gas. (Similar correlations between the conversion efficiency and ionization current were seen in Mg.[17]) At low n, the p states are separated far from the s and d states, hence, angular momentum mixing from collisions would require large energy shifts. These shifts were not detected implying that the l-state mixing explanation is not relevant for these atomic transitions. Dinev et. al.[7] conducted a thorough investigation of SHG in potassium for the two-photon resonances for the s, p and d levels between n=7 -34. They measured the conversion efficiency as a function of input intensity and vapor pressure. They also did an investigation of the polarization dependence of the SHG. The intensity dependence of the SH output, and the polarization results are consistent with the DC-field three-wave mixing model. However, the dependence on vapor pressure is better described by the angular-momentum mixing model.

SHG has also been generated with a one picosecond source in krypton [18] and a 30 picosecond source in xenon [19]. These experiments were conducted off-resonance with 1 micron light. They found complicated dependencies of the SHG conversion efficiency on vapor pressure of the gas and the input field intensities, and deduced a qualitative correspondence between SHG and the multi-photon ionization rates. Both experiments explain their results in terms of the $\chi^{(3)}$, DC-field model.

In this chapter, we describe a propsed experiment on resonant enhanced second - harmonic generation in potassium gas performed with a tunable picosecond dye laser. Our goal is to measure the time scale of the mechanism responsible for SHG by doing a pump-probe measurement. We overlap two pulses of approximately equal intensity in the potassium vapor and vary the time delay between them. If the process responsible for generating SHG is significantly shorter than our laser pulse (2 picoseconds), then the maximum SHG output will occur at zero delay time and will not change as a function of delay. However, if the process is longer than our laser pulse, the SHG output will peak at some finite delay time. We can then monitor this delay as a function of a variety of experimental parameters to better understand the process responsible for SHG in vapors.

B. Proposed Experiment

A schematic of the experimental set-up is shown in Fig. 1. The experiment is being conducted with the laser described in Chap. VI. We use a 50% beam splitter to generate two arms of approximately 200-300 microjoules pulses. We use a collinear geometry for the pump and probe beams. A 1-meter spectrometer is used to measure the SHG output, which provides us with .5 angstrom resolution. The signal is being detected using a photomultiplier tube, and gated electronics for photon counting. We couple out a small percentage of the pump and probe beams for an SHG reference arm which we use to monitor the laser peak intensity fluctuations. To determine the position of the delay arm that corresponded to zero-time delay, we did a collinear autocorrelation measurement in the quartz crystal of the reference arm. The potassium vapor is generated in a standard heat pipe [20] with 10-50 torr of argon gas used as the buffer to the windows. We plan to simultaneously measure the ionization current to see if there was a correlation between SHG output and the amount of ionization current measured.

Given the amplified laser output energy was maximum around 595 nm, we chose to probe the 11s, 9d and 10p levels of potassium. Recently, a series of measurements were

conducted by Dr. Hai Tian Zhou and Professor Jing-yuan Zhang with a nanosecond dye laser to determine the dependence of the conversion efficiency of these levels on laser input intensity, and gas density. They monitored the ionization current as a function of input laser frequency and intensity as well. They found the following results: For the 10s and 11d levels, they found that the SHG conversion efficiency went as the input intensity to the sixth power for input laser intensities below 10^6 W/cm^2. Above 10^6 W/cm^2, they saw a square dependence on the input laser intensity. For the s and d levels, they saw a resonance peak in the ionization current measurements, but for the p-level the ionization current was below their minimum detectable current.

Based on these measurements, we expect to have signal-to-noise ratio greater than 1000 to 1, assuming the process responsible for SHG occurs on a time scale faster than our laser pulse. However, if a DC electric field mechanism is true, we should see a conversion efficiency that depends on time. In Reference 15, Bethune outlines the physical processes that will determine the timescale of SHG generation in a vapor. There are two possible forces that can propel the electrons - the pondermotive potential which is proportional to the gradient of the intensity, and the kinetic energy left over after ionization. Using the expression,

$$V_{pondermotive} = \frac{2\pi e^2}{m\omega^2} E_o^2$$

we estimate the pondermotive potential to be approximately .1 eV. Assuming we are in the mutliphoton ionization regime, we estimate the kinetic energy to be the difference between three photon excitation with 595 nm light and the ionization limit for potassium. This gives a kinetic energy of approximately 1 eV. Three time scales are important: $\tau_p \sim \omega_p^{-1}$ where ω_p is the plasma frequency; τ_l, the laser pulsewidth; and τ_f, the amount of time it takes the for the electrons to move a beam radius. The shortest of these three times will determine how long it takes to establish the maximum DC field and its magnitude. Assuming a

density of 10^{16} electrons/cm^3 , we estimate $\tau_p \sim 10^{-13}$ sec. Our laser pulsewidth is on the order of 10^{-12} sec. Assuming a beam size of 20 microns, we estimate τ_f to range from .1 to 1000 picoseconds, depending on the ionization level. Assuming a beam radius of 20 micron and a kinetic energy of 1 eV, we can estimate the magnitude of the static electric field to be approximately 500 V/cm and the maximum is achieved after 25 picoseconds If a pondermotive potential is responsible for moving the electrons through the focal region, we expect it to take tens of nanoseconds to establish the DC field.

To measure this effect, we plan to do the following experiments. First, we will measure the SHG generated by a single beam propagating through the potassium vapor. If $\tau_f < \tau_l$, we should be able to clearly see an SHG output. We will then overlap a second beam with the first and vary the delay between the two to conduct a pump-probe experiment. The second beam will act to establish the DC-electric field that allows for the generation of SH-photons. If $\tau_f > \tau_l$, we can estimate the size of τ_f by measuring the delay time between the pump and probe that leads to maxmimum SHG output, thereby determining the time scale of the process.

References

[1]S. Dinev, A. G. d. Garcia, P. Meystre, R. Salomaa, H. Walther, in *Laser Spectroscopy* H. P. Weber, W. Luthy, Eds. (Berlin, Germany: Springer, 1983), pp. 183.

[2]S. G. Dinev, J. Phys. B: At. Mol. Opt. Phys. **21**, 1111 (1988).

[3]R. R. Freeman, J. E. Bjorkholm, R. Panock, W. E. Cooke, in *Laser Spectroscopy* A. R. W. McKellar, T. Oka, B. Stoicheff, Eds. (Berlin, Germany: Springer, 1981), pp. 453.

[4]K. Miyazaki, Phys. Rev. A **23**, 1350 (1981).

[5]K. Miyazaki, T. Sato, H. Kashiwagi, Phys. Rev. A **23**, 1358 (1981).

[6]K. Miyazaki, T. Sato, H. Kashiwagi, Phys. Rev. Lett. **43**, 1154 (1979).

[7]S. G. Dinev, Phys. Scrip. **T26**, 17 (1989).

[8]S. Dinev, J Phys B: At. Mol. Opt. Phys. **21**, 1681 (1988).

[9]M.-H. Lu, L.-H. Tsai, J. Phys. B: At. Mol. Opt. Phys. **23**, 921 (1990).

[10]M.-H. Lu, J.-H. Tsai, Chin. J. Phys. **27**, 14 (1989).

[11]J.-H. Tsai, M.-H. Lu, Appl. Phys. B **51**, 386 (1990).

[12]N. Bloembergen, J. Opt. Soc. Am. **70**, 1429 (1980).

[13]T. Mossberg, A. Flusberg, S. R. Hartmann, Opt. Commun. **25**, 121 (1978).

[14]J. Okada, Y. Fukuda, M. Matsuoka, J Phys Soc Jap **50**, 1301 (1981).

[15]D. S. Bethune, Phys Rev A **23**, 3139 (1981).

[16]A. Elçi, D. Depatie, Phys. Rev. Lett. **60**, 688 (1988).

[17]J.-Y. Zhang, H.-T. Zhou, P. Jin, in *Resonance Ionization Spectroscopy* T. B. Lucatorto, J. E. Parks, Eds. (Institute of Physics, Gaithersburg, Maryland, USA, 1988), pp. 29.

[18]S. Augst, D. D. Meyerhofer, C. I. Moore, J. Peatross, in *Fsec to Nsec High-intensity lasers and applications* (SPIE, 1990), pp. 152.

[19]M. S. Malcuit, R. W. Boyd, W. V. Davis, K. Rzazewski, Phys. Rev. A **41**, 3822 (1990).

[20]C. R. Vidal, J. Cooper, J. Appl. Phys. **40**, 3370 (1969).

Figure Captions

Figure 1: Schematic of experimental set-up

Figure 2: Energy level diagram of potassium

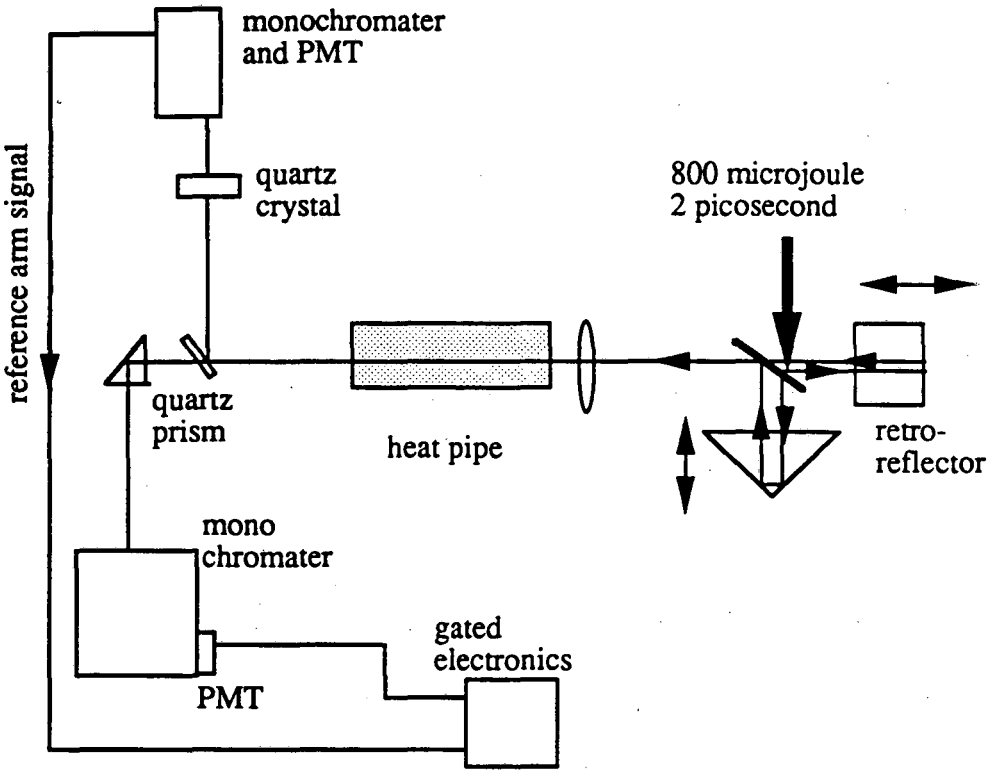
monochromater
and PMT
quartz
crystal
800 microjoule
2 picosecond
reference arm signal
quartz
prism
heat pipe
retro-
reflector
mono
chromater
gated
electronics
PMT

Figure 1

LAWRENCE BERKELEY LABORATORY
UNIVERSITY OF CALIFORNIA
INFORMATION RESOURCES DEPARTMENT
BERKELEY, CALIFORNIA 94720